# Nonlinear Estimator for a Class of Systems with Linear Dynamics and Noisy Quadratic Measurements

Mahmood Rezaee Qotb Abadi

A Thesis in

The Department

of

Electrical and Computer Engineering

Presented in Partial Fulfillment of the Requirements

For the Degree of Master of Applied Science (Electrical and Computer Engineering)

at Concordia University

Montréal, Québec, Canada

May 2024

Concordia University

School of Graduate Studies

This is to certify that the thesis

prepared by: Mahmood Rezaee Qotb Abadi

Entitled: Nonlinear Estimator for a Class of Systems with Linear Dynamics and Noisy Quadratic Measurements and submitted in partial fulfillment of the requirements for the degree of

**Master of Applied Science (Electrical and Computer Engineering)**

complies with the regulations of the University and meets the accepted standards with respect to originality and quality.

Signed by the final Examining Committee:

_____ Chair

Dr. Y. R. Shayan

_____ External Examiner

Dr. W. Lucia

_____ Examiner

Dr. R. Selmic

_____ Supervisor

Dr. L. Rodrigues

Approved by _____

Dr. Y. R. Shayan, Chair

Department of Electrical and Computer Engineering

_____ 2024 _____

Dr. M. Debbabi, Dean

Faculty of Engineering and Computer Science

# Abstract

Nonlinear Estimator For a Class of Systems with Linear Dynamics and Noisy Quadratic Measurements

Mahmood Rezaee Qotb Abadi

This thesis proposes a novel nonlinear estimator to estimate the state of a class of systems with linear dynamics and noisy quadratic measurements. It is shown that the error dynamics is described by a nonlinear Verhulst logistic equation. This observation unveils a link between population dynamics and state estimation for this class of systems. The stationary distribution of the estimation error converges to a zero-mean Gaussian with adjustable variance. This estimator is used to estimate the physical state variables in energy harvesters by using the measurement of electrical energy. Furthermore, the problem of estimating the position of a quadrotor in waypoint navigation using noisy range measurements can be formulated in a way in which it can be solved by the proposed estimator. This application emphasizes the practical use of the estimator, which guides the quadrotor through various pipeline configurations. The quadrotor's input is designed to maintain the piecewise affine trajectory within the thickness of the pipeline for the inspection task. The simulation results illustrate a stable estimation error that consistently converges to an area around zero with different initial conditions. In addition to evaluating the performance of the proposed estimator, a comparison is made with the Kalman filter for the augmented linearized system.

# Acknowledgements

First and foremost, I would like to express my deepest gratitude to my family. Their unconditional love and support despite the distance, have been my anchor through the most challenging times. Their belief in me has always kept my spirits and motivation high.

To my dearest Ming, my happiness, this endeavor would not have been possible without your unwavering support and motivation. In my darkest times, you were my only light. You consistently reminded me of the brighter side of life, for which I am eternally thankful.

To my best friend in the world, Ali, the saddest part of my studies was being physically apart from you, though our connection is unbreakable. Ali, your companionship, insightful discussions, and the joy you bring into my life are invaluable.

My appreciation extends to my colleagues Steven, Camilo, Soroush, Zachary, Lucas, Sonali, Giuseppe, and Karolina. Your work ethic, humor, and contagious enthusiasm not only elevated my own efforts but also created an environment that felt like family. Thank you for your support and fellowship. A special thanks to all my friends, whose constant encouragement fueled my perseverance.

I must express profound appreciation to Concordia's faculty and staff, with a special mention of my supervisor, Dr. Luis Rodrigues. His passion, guidance, and support have profoundly influenced my academic journey, constantly pushing me to strive for excellence. Without his dedication, this thesis would not have been possible.

Lastly, I want to thank myself for not giving up during the toughest times.

# Contents

# List of Figures

# List of Tables

# Chapter 1

# Introduction

## 1.1 Motivation

In control theory, robotics, signal processing, navigation, and other engineering fields, where it is important to precisely and reliably determine the system's current state, state estimation plays a crucial role. This knowledge is essential to design controllers to stabilize the system, improve performance, and promote better decision-making. Effective state estimation becomes significantly more challenging and important in systems perturbed by noise. Noise, an intrinsic feature of real-world systems, introduces uncertainty and can lead to erroneous decisions if not properly accounted for. Therefore, the development of robust state estimation methods capable of estimating the states while handling noise is of paramount importance.

State estimation involves the process of finding the internal state of a system by fusing a mathematical model with input and output data measurements. State estimation techniques are fundamental in various tasks related to analysis, monitoring, and energy management. An estimation approach might suggest installing sensors throughout the system, covering every conceivable aspect of the system. Nevertheless, in most practical applications, this approach is neither feasible nor pragmatic. This can result in high costs, difficulties in man-

agement, and potential changes to the original system design, among other concerns [1]. Consequently, state estimation methods can serve as a more practical and cost-effective alternative to the installation of sensors.

In this context, this thesis addresses the critical challenge of state estimation in systems with quadratic measurements perturbed by noise. We introduce a nonlinear estimator designed for these types of systems, offering a versatile and accurate solution for estimating system states even in the presence of considerable noise sources. To illustrate the practical significance of this novel estimator, we present two distinct yet interconnected applications.

In the field of electrical circuits, estimating the voltage of a capacitor using the measurement of the energy stored in the capacitor could be a theoretical subject of interest. Especially when the energy measurements are affected by noise. Noisy measurements of the energy stored in an inductor can also lead to inaccuracies in estimating the current through the inductor. In mechanics, the kinetic energy of a moving body is proportional to the square of its velocity. Therefore, it is possible to model the problem of estimating the body's velocity using measurements of the kinetic energy from noisy sensors. Similarly, in rotational mechanics, the kinetic energy of a rotating body is proportional to the square of its angular velocity. Furthermore, in mechanical systems involving a spring, the potential energy stored in the spring is proportional to the square of its displacement from equilibrium. If the measurements of the potential energy are perturbed by noise, the problem of estimating the displacement can be modeled as the same state estimation problem. The theoretical significance of these problems outweighs their practical application. This is primarily due to the fact that, in many cases, it is more straightforward to measure physical variables such as voltage, current, velocity, or displacement as opposed to measuring power or energy directly. The theoretical significance of estimating physical variables from energy measurements becomes manifestly practical in our first application, where we leverage measurements of electrical energy produced in an energy harvester to estimate crucial physical variables such as displacement or velocity. In energy harvesters, electrical energy or power is readily available

and often measured. Utilizing this existing measurement enables us to accurately estimate important physical variables without the need for extra equipment or measurements.

### 1.1.1 Energy Harvester

The widespread use of portable electronic devices such as mobile phones, global positioning systems (GPS), and wearable devices for health care, medical rehabilitation, and athletic training is becoming more prevalent in our daily lives. Consequently, the need for mobile power sources experiences a proportional rise. The energy requisites for these devices are predominantly satisfied through battery systems. Nevertheless, the requirement to periodically recharge these batteries (or ultimately replace them) poses a substantial constraint on the operational usage time (or longevity) of these portable electronic gadgets. This issue can be addressed by directly linking the applicable device to an electrical grid. Nonetheless, the availability of an electric grid is not universally attainable, particularly in developing nations or during traveling to remote locations. Therefore, this solution becomes infeasible [2].

Up until the present time, efforts directed towards the enhancement of power efficiency and the creation of batteries with improved power density have yielded an approximately two-fold augmentation in power density every decade. However, the operational usage time of any mobile system functioning without direct reliance on the electrical grid is constrained by the necessity of carrying and recharging the battery [3]. This limitation highlights the need for further research into portable electrical generation devices capable of augmenting both the capacity and the operational usage time of electrical power. A promising and environmentally friendly method to fulfill the aforementioned requirement is to harness the heat [4], vibration [5], movement, and strain energy [6] produced by the human body to generate electrical energy [2]. The foundation of this self-powered approach lies in the presence of abundant kinetic energy sources within the human body, particularly during limb movements such as joint rotations ([7], [8], and [9]). Transformation of kinetic energy into electrical energy can be achieved through piezoelectric, electromagnetic, and electrostatic mechanisms

([10], [11], and [12]). Some applications of energy harvesting are shown in Figure 1.1.

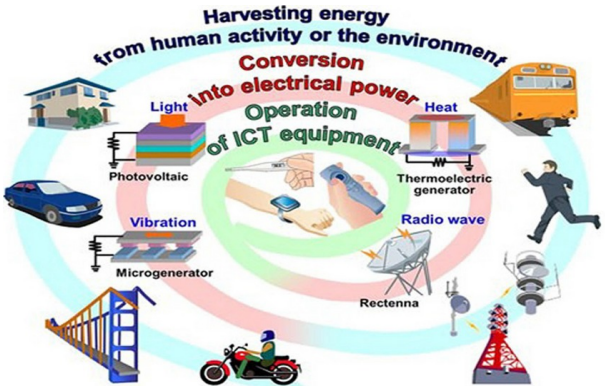


(a) Applications of energy harvesting and associative technologies [13]


(b) Self-powered sensing by rotational energy harvesting from different application [14]

(c) Strap-on kinetic energy harvester from walking [15]

(d) Bionic power knee energy harvester [16]

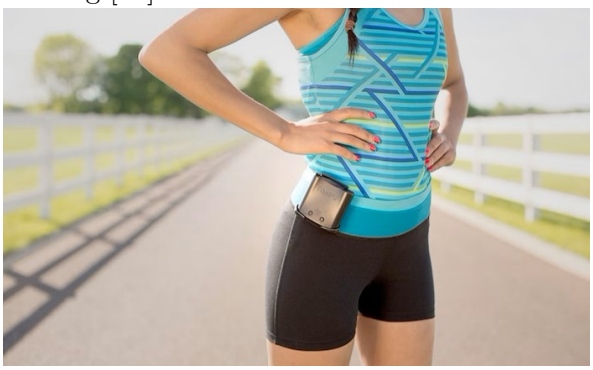

(e) A wearable battery motion energy harvester to power mobile devices [17]

(f) Human body movement energy harvester smartwatch [18]

Figure 1.1: Applications of energy harvesting

In the field of energy harvesting, we embark on a journey that combines theory and practice.

As mentioned earlier while it is important in theory to estimate variables, such as displace-

ment and velocity, from energy measurement, we often overlook their applications due to the ease of direct measurement. However, in our application, we connect this theoretical foundation with real-world usefulness. The electrical energy or power generated from the energy harvesting process is easily measurable. The electrical energy or power produced is approximately a factor of the mechanical energy due to energy loss. The kinetic energy is proportional to the square of velocity, and the potential energy stored in a spring is proportional to the squared of the displacement. Therefore, leveraging the measurement of electrical energy or power allows us to accurately estimate key physical variables, such as body movement velocity. This paves the way for an era of cost-effective state estimation within the field of energy harvesting.

### 1.1.2 Navigation with Range Measurement

An essential challenge in navigation is to determine the position of a moving vehicle based on a collection of range measurements between the vehicle and landmarks with known inertial coordinates, especially in the presence of measurement noise [19]. This issue can be further formulated as a state estimation task, utilizing the same framework of the quadratic measurement state estimation problem.

Navigation is a critical task that pertains to the process of accurately determining and monitoring the position, velocity, and orientation of an object or vehicle. It plays a vital role in a vast array of fields including transportation, exploration, military operations, and increasingly in personal mobility with applications to self-driving cars and unmanned aerial vehicles (UAVs). One of the major goals when designing autonomous vehicles and high-tech human-operated vehicles is the development of an efficient navigation system.

In recent years, UAVs have garnered a growing interest from both the research and industrial sectors. A wide array of applications are enabled by combining UAVs with the Internet of Things (IoT) ([20], [21]), such as environmental monitoring [22], the assessment of struc-

tural health [23], precise agricultural practices [24], search and rescue missions [25], to name a few. In the realm of autonomous UAV navigation, one of the common methodologies is Inertial Navigation Systems (INS) [26]. An INS estimates a UAV's current position and velocity by means of continuous integration (over time) of sensor data; Although the INS has widespread application, it suffers from the problem of cumulative error propagation. As time progresses, the magnitude of the estimation error tends to increase. Consequently, in practical scenarios, recourse is often made to the Global Positioning System (GPS) to periodically recalibrate the INS ([27], [28]). Inertial Navigation Systems (INS) and Global Positioning System (GPS)-related technologies have undergone an upsurge in interest and rapid development. Given these advancements, and particularly the growing popularity of GPS receivers, one may be led to believe that the navigation problem has practically been solved except for a steady search of more accurate, cost-efficient, and reduced-size solutions. Nevertheless, the navigation problem is still rather challenging in many real-world situations when GPS signals are not available. Typical GPS-denied environments in which GPS is unavailable, or not reliable, include

- **Indoor:** Within structures where the concrete walls block GPS signals, such as caves either on land or underwater.
- **Urban:** In cities, GPS signals are unreliable and sometimes obstructed by nearby structures or completely lost in tunnels.
- **Space:** Despite some experimental work on the use of GPS signals in space applications, GPS signals are often not accessible in space.
- **Underwater:** In lakes, rivers, or oceans.

Furthermore, GPS is vulnerable to both inadvertent and intentional interference, which can disrupt its functionality. A temporary loss of GPS signals is not uncommon, lasting from a few seconds to several minutes. In the case of UAVs that depend exclusively on GPS for

their navigation, such an occurrence can have disastrous consequences [29]. In these GPS-denied environments, different sensors must be used for navigation. The type of sensors used depends on the environment, the mission scenario, cost constraints, etc. A common choice is using Range-Only measurements which can be obtained from transponders, either acoustic or electromagnetic, depending on the environment. The range-only localization problem entails estimating the position of a vehicle with respect to a collection of places whose inertial positions are known using the ranges or squared ranges measurement. Range measurements can provide sufficient information to determine the position of the vehicle, and they eliminate the need for additional equipment or sources, which can save costs and increase the ease of implementation.

A quadrotor is a type of UAV that is lifted and propelled by four rotors. These rotors are arranged in a cross configuration, with two rotors spinning clockwise and two spinning counterclockwise. The quadrotor is able to perform a wide range of movements, including vertical take-off and landing, hovering, forward and backward flight, and lateral movement. These movements are achieved by adjusting the speed and thrust of each rotor. The ability of the quadrotor to perform these movements makes it useful in a variety of applications, such as aerial photography and surveillance, search and rescue, and delivery.

Waypoint navigation refers to the process of navigating a route or trajectory (mostly a straight line) between a series of predetermined points, often termed "waypoints". These waypoints are specific geographic locations, defined by coordinates in a reference system. The vehicle in waypoint navigation, follows this sequence of waypoints to move from an origin to a desired destination. This method of navigation is widely used in various applications (Figure 1.2).

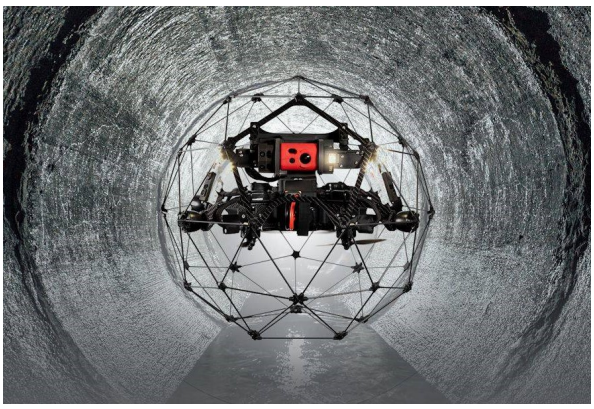

(a) Pipeline Inspection [30]

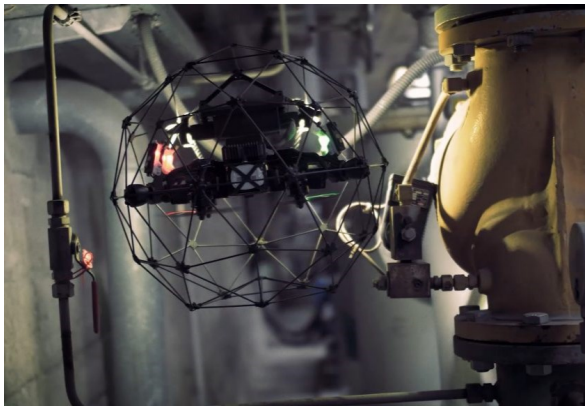

(b) Indoor Pipes and Valves Inspection [31]

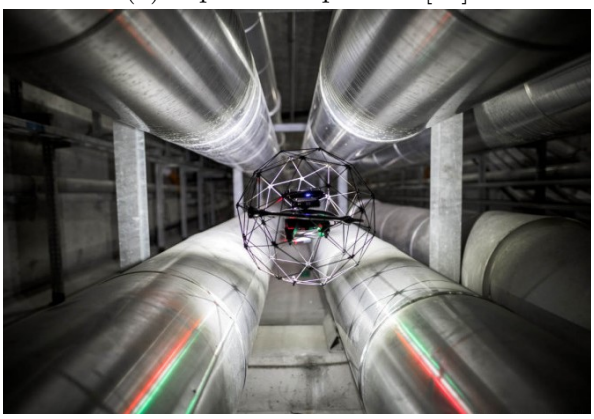

(c) Oil and Gas Pipe Inspection [32]

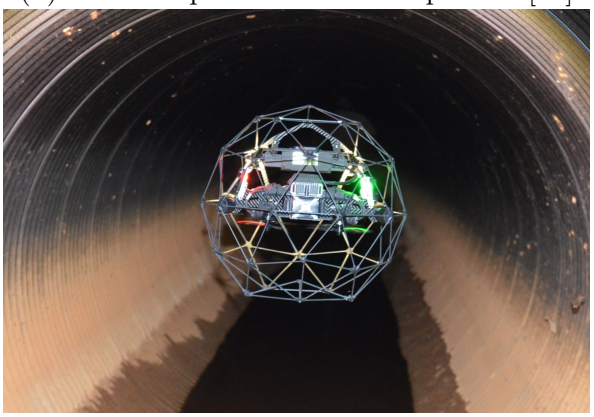

(d) Pipe Inspection [33]

(e) Train Railroad and Mining Inspection [34]

(f) Sewer Inspection [35]

Figure 1.2: Applications of UAV's waypoint-based navigation in GPS-denied environments

In this work, pipeline inspection is considered using a quadrotor as an inspector with a waypoint-based navigation system based on quadratic range measurements. Pipeline inspection is a critical process for ensuring the integrity and safety of pipelines. It is typically performed using specialized inspection tools (UAVs, UUVs, etc) that are designed to travel

through the pipeline and collect data on the potential leaks in the pipeline. The navigation system in these inspectors should be as accurate as possible so that the exact location of the leaks in the pipeline can be marked out even in GPS-denied environments. Potential scenarios are the inspection of underground pipelines that are installed along GPS-denied environments such as caves.

## 1.2 Literature Survey

State estimation is the process of determining the state of a system based on a set of measurements and a mathematical model of the system. Classical estimation algorithms include Kalman filtering [36] and particle filtering [37]. Sensor fusion techniques allow the system to integrate data from several sensors in a consistent and reliable manner, resulting in a more robust and accurate navigation system. These techniques can be applied in various forms, such as probabilistic data association [38], extended Kalman filtering [39], and unscented Kalman filtering [40]. By combining the strengths of multiple sensors and state estimation techniques, sensor fusion can provide a more accurate and reliable estimate of the system's state, even in challenging environments. This is especially important in autonomous systems, as they often rely on a variety of sensor types, such as cameras, Lidars, and GPS, to sense the environment and make decisions.

The problem of navigation and source localization using measurements from a set of sensors has been widely researched in recent years. The sensor solutions depend on the environment, the mission scenario, and cost constraints, to name a few. Common navigation solutions include Global Positioning System (GPS) [41], Long Baseline (LBL), Short Baseline (SBL), and Ultra Short Baseline (USBL) navigation [42]. In addition to these methods, a number of scholars have embraced a method referred to as SLAM, an acronym for Simultaneous Localization and Mapping, as a means of guiding vision-based navigation. Initially conceived

for robotic applications, SLAM's primary objective involves the estimation of a robot's own position (i.e., localization) and the positions of a set of landmarks (i.e., mapping) ([43], [44], and [45]). In most cases, this can be accomplished through an EKF that uses range measurements from the robot to the landmarks as observation data.

Paper [46] presents an indoor navigation approach for UAVs using low-cost range sensors. The authors address the challenges of mapping and self-localization in complex unknown indoor environments and propose a wall-following guidance algorithm for navigation. The authors in [47] address the problem of UAVs circumnavigating an unknown target in a GPS-denied environment by utilizing a method to estimate the target's position using range-only measurements obtained from the UAV's sensors. The method entails estimating the target's position based on the range data, using a Kalman filter. Reference in [48] proposes a technique for UAV navigation in indoor GPS-denied environments, using range measurements and odometry. The proposed algorithm extracts the range data and odometry from the terrestrial radio measurements between the UAV and a set of stationary reference points using inertial sensors, such as an accelerometer. Then a Kalman filter is used to fuse the range and odometry measurements and estimate the UAV's state. The article [49] developed an indoor localization method for unmanned aerial vehicles (UAVs) by integrating range distance measurements with data from an Inertial Measurement Unit (IMU), which includes acceleration and angular rate. This method utilizes an Unscented Kalman Filter (UKF) to enhance the fusion of these sensory inputs. Their research demonstrates improvements in the accuracy and reliability of UAV localization within indoor environments, highlighting the effectiveness of sensor data fusion. The research presented in [29] proposes an EKF to estimate the position of the maneuvering UAV that lost its GPS connection, by measuring the range to two individual UAVs at known locations. Article [50] provides a method that takes advantage of aided measurements from one or more cooperative UAVs flying under full GPS coverage to enhance the navigation performance of a UAV in GPS-challenging environments. A sensor fusion method based on an EKF is used that combines measurements

from onboard inertial sensors and magnetometers, available GPS pseudoranges, position information from cooperative UAVs, and line-of-sight estimated by vision-based tracking [50]. In paper [28], relative navigation is proposed using only inter-satellite range measurements. It also explores the observability of range-only relative navigation, possible trajectories that can produce the same time history of range measurements, and a method for computing these solutions.

From a control point of view, the article [51] has developed a range-based sliding mode control for the autonomous navigation of an aerial drone to approach and follow a herd of cattle. The algorithm does not depend on the accuracy of the range measurements, however, the rate of change of range measurements is used to fly the drone towards the herd. Article [52] designs a robust heading controller that employs a sliding mode controller for UAVs to effectively intercept both stationary and moving ground targets of interest. The proposed approach offers low computing costs and minimal sensor requirements, merely relying on range measurements. Article [53] introduces a trajectory generation and tracking method for drones in urban environments. This algorithm navigates the drone along a predefined path that passes through a given set of waypoints with linear segments between them. In addition to aiding UAV navigation, the utilization of range measurements holds significant prominence in the navigation of underwater vehicles. In reference [54], a synthetic long baseline navigation algorithm is proposed for underwater vehicles. The vehicle uses range measurements from a single transponder, and a discrete-time Kalman filter is designed for the linearized model of the system to obtain the required estimates. In [55], the authors address the problem of underwater navigation with unknown currents using range measurements to a single beacon, and an analysis of the observability of the nonlinear system is performed by linearizing it. A Luenberger estimator for the linearized system is introduced, but in practice, an extended Kalman filter (EKF) is implemented to estimate the state without any guarantees of global asymptotic stability. This problem has been further studied in [56] and [57] using the EKF to solve a navigation problem based on single beacon range

measurements. In [58], the authors propose an algorithm based on the square of the range measurements to a source while taking into account the inertial position of the agent. This method is able to provide the necessary self-awareness of the agent's motion to achieve Global Exponential Stability (GES) under a persistent excitation condition. The work of Batista, Silvestre, and Oliveira [59, 60, 61] on source localization and vehicle navigation based on single-range measurements uses state augmentation to derive a linear time-varying (LTV) model. The necessary and sufficient conditions for the observability of the nonlinear system are derived, and a Kalman filter is applied to the augmented linear time-varying system to estimate the system state with globally asymptotically stable error dynamics. Further research by the same authors, including acceleration readings, can be found in [62], where conditions were derived for globally asymptotically stable error dynamics. The article [61] addresses the problem of navigation and source localization using range measurements to a single source in the presence of unknown constant drifts. The system's observability is studied and a Kalman filter is proposed for the LTV system with guarantees of global exponential stability (GES) of the error dynamics. The estimator solutions proposed in [63] are inspired by the work of Batista et al. with some noticeable differences, particularly in terms of the augmented state definition and the formulation of persistent excitation (PE) conditions that ensure uniformly exponentially stable (not just convergent) over time. Article [64] uses an augmenting method proposed by Batista et al. [59, 60, 61] for state estimation in systems with linear dynamics and quadratic output. It also introduces persistent excitation conditions on the input and its derivatives to ensure uniform observability. In [65], the authors introduced a systematic method for systems with linear dynamics and quadratic outputs into a higher-dimensional LTV system by adding the minimum necessary auxiliary states. This approach simplifies the observer design process by linearizing the output relation, facilitating the use of a Kalman-type observer for global exponential state estimation.

Estimation methods for the class of linear systems with quadratic measurement in the existing literature frequently use the Kalman filter family. Especially navigation techniques

based on range measurements gravitate towards linearizing the estimation problem and use the Kalman filter. However, it is imperative to address these problems using a nonlinear estimation method. Some of the most important limitations of the methods in the literature are concerns about the convergence time and the accuracy of estimation. Consequently, there exists a pressing need for improvement in these critical aspects.

## 1.3 Contributions

This thesis addresses the state estimation problem in a class of systems with linear dynamics and quadratic measurements perturbed by noise. A novel nonlinear estimator is proposed to estimate the state in this class of nonlinear systems, without transforming the system into a linear system. The contributions of this work are:

1. In Chapter 3, The estimation error dynamics is found to be a non-autonomous Verhulst logistic equation that unveils the link between the estimation problem and the population dynamics. Moreover, the equation of time evolution of the probability density function of the estimation error is derived (the Fokker-Planck-Kolmogorov equation). Then, the stationary distribution of the error is proved to converge to a zero-mean Gaussian with adjustable variance under certain conditions. Furthermore, the performance of the proposed estimation method is illustrated through an example of velocity estimation from energy measurement in human body energy harvesters.

2. In Chapter 4, the nonlinear estimator proposed in Chapter 3 is extended for piecewise affine motions (each piece occurs on a given plane). The estimation error is proved to converge to zero in steady-state. Moreover, a navigation algorithm is proposed for a UAV pipeline inspector in a GPS-denied environment where the measurement is squared range.

## 1.4 Thesis Structure

This thesis will be subdivided into the following chapters. Chapter 2 provides an overview of the theoretical preliminaries required in this thesis. These preliminaries include concepts in linear algebra, probabilistic estimation, Brownian motion, stochastic differential equations, and Verhulst population dynamics. Chapter 3 then proposes a nonlinear method of state estimation with its application to energy harvesters to estimate physical states from noisy energy measurements. In Chapter 4, the same nonlinear estimator is extended to the piecewise affine trajectories. A case study of state estimation for navigation of a quadrotor pipeline inspector using a noisy range measurement is subsequently performed. Finally, Chapter 5 presents the conclusions and future considerations.

# Chapter 2

# Theoretical Preliminaries

## 2.1 Introduction

In this chapter, a review of the theoretical preliminaries of this thesis is performed. In Section 2.2, conventions and notations used in this thesis are introduced. Subsequently, in Section 2.3, a review of probability theory is carried out followed by a summary of the Brownian motion, stochastic differential equations, and the Fokker-Planck-Kolmogorov equation. A concise review of state estimation is presented in Section 2.4 including the observability of linear time-variant (LTV) and nonlinear systems and the Kalman filtering method for LTV systems. Finally, the Verhulst population dynamics is briefly explained in Section 2.5.

## 2.2 Conventions and Notations

### 2.2.1 Array and Matrix Conventions and Notations

In this thesis, a column array is denoted by a lowercase bold letter, and an $m \times n$ matrix which is a two-dimensional array of numbers is denoted by an uppercase letter, e.g.,

$$\mathbf{a} = \begin{bmatrix} a_1 \\ \vdots \\ a_n \end{bmatrix}, \qquad A = \begin{bmatrix} a_{11} & a_{12} & a_{13} & \dots & a_{1n} \\ a_{21} & a_{22} & a_{23} & \dots & a_{2n} \\ \vdots & \vdots & \vdots & \ddots & \vdots \\ a_{m1} & a_{m2} & a_{m3} & \dots & a_{mn} \end{bmatrix}. \tag{2.1}$$

The transpose of the matrix $A$ is designated as an $n \times m$ matrix $A^T$. The matrix $A^{-1}$ denotes the inverse of the matrix $A$, and for a square matrix $A$, it satisfies $AA^{-1} = A^{-1}A = I$, where $I$ is an identity matrix of the same dimensions as $A$.

Throughout this thesis, a vector is denoted by $\vec{v} = v\vec{e_v}$, where $v = \|\vec{v}\|$ is the magnitude of $v$ and $\|.\|$ denotes the 2-norm, and $\vec{e_v}$ is a unit vector that indicates the direction.

### 2.2.2 Change of Coordinates

Given that a vector may have different coordinates when observed from different reference frames, it becomes necessary to change these coordinates when transitioning between said frames. The notation used for the coordinates of the vector $\vec{v} \in \mathbb{R}^2$ with respect to the frame $I$, is ${}^I[\vec{v}]$ and can be written as the column array,

$${}^I[\vec{v}] = \begin{bmatrix} v_1 \\ v_2 \end{bmatrix}. \tag{2.2}$$

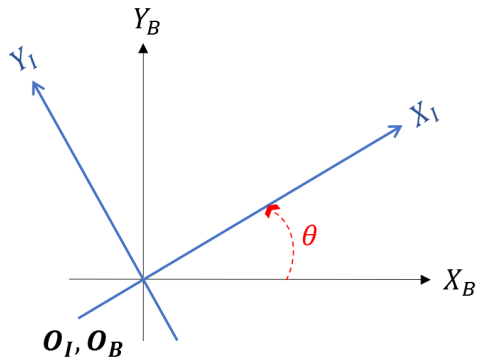


Figure 2.1: Change of coordinates

The rotation matrix $\mathcal{R}_B^I$ to change the coordinates of a vector from the frame $I$ to $B$ in 2-D is denoted by

$$\mathcal{R}_B^I = \begin{bmatrix} \cos(\theta) & -\sin(\theta) \\ \sin(\theta) & \cos(\theta) \end{bmatrix} \tag{2.3}$$

where $\theta$ is the clockwise angle between the $X_I$ and the $X_B$ axis (see Fig.2.1). One can then write

$${}^I[\vec{v}] = \mathcal{R}_B^I {}^B[\vec{v}] \tag{2.4}$$

## 2.3 Probability Theory

In the context of this thesis, probability theory plays a fundamental role in modeling and analyzing systems with noise. The **probability space** denoted by $(\Omega, \mathcal{F}, p)$ is the underlying concept in probability theory. The set $\Omega$ is the basic sample space in which its elements $\omega$ are samples or outcomes. Events are specific subsets of $\Omega$ or collections of outcomes. The probability of an event or a variable is denoted as $p(x)$. This function signifies the likelihood or chance associated with the occurrence of a specific event or the value of a random variable.

### 2.3.1 Random Variables and Stochastic Processes

In the study of probability theory, the concept of a random variable is crucial. Therefore, in this section, a review of random variables is presented. Despite its nomenclature, a random variable is neither intrinsically random nor a variable. It is in fact a deterministic function

that associates a real number with each possible outcome of a random experiment, hence providing a numerical representation of random outcomes.

**Definition 1.** *[66] A real finite-valued function $X(\cdot) : \Omega \to \mathbb{R}$ is called a* ***random variable*** *if, for every real number $x$, the inequality*

$$X(\omega) \leq x \tag{2.5}$$

*defines an $\omega$ set, whose probability is defined.*

Crucially, for this mapping to be valid in the probabilistic sense, it must be measurable according to the next definition.

**Definition 2.** *[67] Let $(\Omega, \mathcal{F}, p)$ be a probability space. A function $X : \Omega \to \mathbb{R}$ is called $\mathcal{F}$ measurable if for all open sets $U \in \mathbb{R}$, their pre-image under $X$ belongs to $\mathcal{F}$,*

$$X^{-1}(U) = \{w \in \Omega : X(w) \in U\} \in \mathcal{F} \tag{2.6}$$

A random variable $X$ is an $\mathcal{F}$-measurable function. In other words, it is a measurable function, denoted $X(\omega)$, which maps sets of events in $\mathcal{F}$ onto the real number line.

**Definition 3.** *[66] The distribution function of the random variable $x$ is defined for all real $x$ as follows:*

$$F_x := p(X(\omega) \leq x) \tag{2.7}$$

**Definition 4.** *[66] A random variable $x$ is continuous if there exists a Probability Density Function (PDF) $f_X(\cdot)$, such that*

$$F_X(x) = \int_{-\infty}^{x} f_X(s)ds, \quad -\infty < x < \infty \tag{2.8}$$

**Theorem 2.1.** *[66] A probability density function exists provided that the distribution function is absolutely continuous. This implies that the distribution function $F_X(\cdot)$, should be*

*differentiable almost everywhere, with the exception being only at a finite or countably infinite number of points. Therefore, it is evident from equation* (2.8) *that*

$$f_X(x) = \frac{d}{dx} F_X(x) \tag{2.9}$$

*at all $x$ where the derivative exists.*

In the realm of random experiments, it is common for researchers to be particularly interested in the expected value, or the mean, of a random variable. This concept is defined as follows.

**Definition 5.** *[67] Suppose $(\Omega, \mathcal{F}, p)$ is a probability space and $X$ is integrable (based on Lebesgue integral definition), i.e. $X \in L^1(\Omega, \mathcal{F}, p)$. The expected value (mean, average, first moment) of a continuous random variable taking values $x \in [x_{min}, x_{max}]$, is defined as*

$$\mathbb{E}[X] := \int_{x_{min}}^{x_{max}} x f_X(x) dx, \tag{2.10}$$

*where $f_X(x) \geq 0$ is the PDF and satisfies*

$$\int_{x_{min}}^{x_{max}} f_X(x) dx = 1. \tag{2.11}$$

The expected value for probability integrals with $F = [x_{min}, x_{max}]$ can also be rewritten as

$$\mathbb{E}[X] = \int_{x_{min}}^{x_{max}} x \frac{dp}{dx} dx = \int_F X dp \tag{2.12}$$

where $X$ is a function that maps random outcomes into real values $x$ and $\frac{dp}{dx} = f_X(x)$ is the PDF.

**Theorem 2.2.** *[67] The expected value holds the following properties:*

1. *(Linearity)* $\mathbb{E}[\alpha X + \beta Y] = \alpha \mathbb{E}[X] + \beta \mathbb{E}[Y]$, $\forall \alpha, \beta \in \mathbb{R}$,

2. *(Nested Expectation)* $\mathbb{E}[\mathbb{E}[X]] = \mathbb{E}[X]$,

3. *(Inner Product)* $\mathbb{E}[XY] = \langle X, Y \rangle$ *if* $\mathbb{E}[X^2] < \infty$, $\mathbb{E}[Y^2] < \infty$

**Definition 6.** *[66] The n-th moment of x about the mean (n-th central moment) is defined by*

$$\mathbb{E}\big[(x - \mathbb{E}(x))^n\big] := \int (x - \mathbb{E}(x))^n f_X(x) dx \tag{2.13}$$

In some cases, a thorough understanding of the statistical interdependence or correlation between two random variables is essential to fully grasp the dynamics of the underlying system or process. Correlation can be defined based on the notion of covariance.

**Definition 7.** *[67] The covariance between two random variables X and Y is defined as*

$$K_{XY} = \mathbb{E}[(X - \mathbb{E}[X])(Y - \mathbb{E}[Y])] = \mathbb{E}[XY] - \mathbb{E}[X]\mathbb{E}[Y]. \tag{2.14}$$

*The covariance between X and X is called the variance* $K_{XX} = \sigma_X^2$*, and two random variables* $X, Y$ *are uncorrelated if* $K_{XY} = 0$*.*

**Definition 8.** *[68] In probability theory, events are called independent if the occurrence of one event does not affect the probability of the occurrence of the others. Formally, a set of events* $A_1, A_2, ..., A_n \in \mathcal{F}$ *is mutually independent if the probability of the intersection of any subset of these events equals the product of their probabilities. i.e. for any subset* $A_{i1}, A_{i2}, ..., A_{ik}$*, this can be written as* $p(A_{i1} \cap A_{i2} \cap ... \cap A_{ik}) = p(A_{i1})p(A_{i2})...p(A_{ik})$*.*

**Theorem 2.3.** *[69] If random variables* $X_1, X_2, ..., X_k$ *are mutually independent, then*

$$\mathbb{E}\left[\prod_{i=1}^{k} X_i\right] = \prod_{i=1}^{k} \mathbb{E}[X_i] \tag{2.15}$$

**Theorem 2.4.** *[67] If two random variables X and Y are independent then they are uncorrelated.*

Notice that the reverse is not true in general, meaning two variables being uncorrelated does not imply that they are independent.

It is important to note that the definition of the expected value for random vectors is identical to that for random variables. This is because, by definition, vector summation and integration are executed coordinate-wise. However, random vectors are associated with a distinct construct known as a covariance matrix.

**Definition 9.** *[67] The covariance matrix of the random vector $X$ is defined as*

$$\mathcal{K}_x = \mathbb{E}[(X - \mathbb{E}[X])(X^T - \mathbb{E}[X^T])] = \mathbb{E}[XX^T] - \mathbb{E}[X]\mathbb{E}[X^T]. \tag{2.16}$$

The covariance matrix is always symmetric since the element $(i, j)$ of the covariance matrix is the covariance $K_{X_iX_j}$ between the random variables $X_i$ and $X_j$. Furthermore, each element $(i, i)$ in the main diagonal is the variance (second moment about the mean) $\sigma_i^2$ of the random variable $X_i$, i.e.

$$\sigma_i^2 = \mathbb{E}[X_i^2] - \mathbb{E}^2[X_i]. \tag{2.17}$$

Following the concept of individual random variables, one encounters stochastic processes, which extend the theory's application to variables changing over time or space. An intuitive definition of a stochastic process is a series of random variables that are indexed by either time or space.

**Definition 10.** *[67] A stochastic process is a parameterized family of random variables $\{X_t(\omega)\}_{t\in I}$ indexed by a set $I$.*

A stochastic process can thus be understood as a function with two parameters: the outcome of a random experiment, represented as $\omega$, and an index $t$, typically associated with the time evolution. Stochastic processes can be interpreted in one of two ways:

1. For fixed $\omega$, a stochastic process is a function of time, known as a sample path of the stochastic process.

2. For fixed $t$, a stochastic process is a function of $\omega$ and behaves like a random variable.

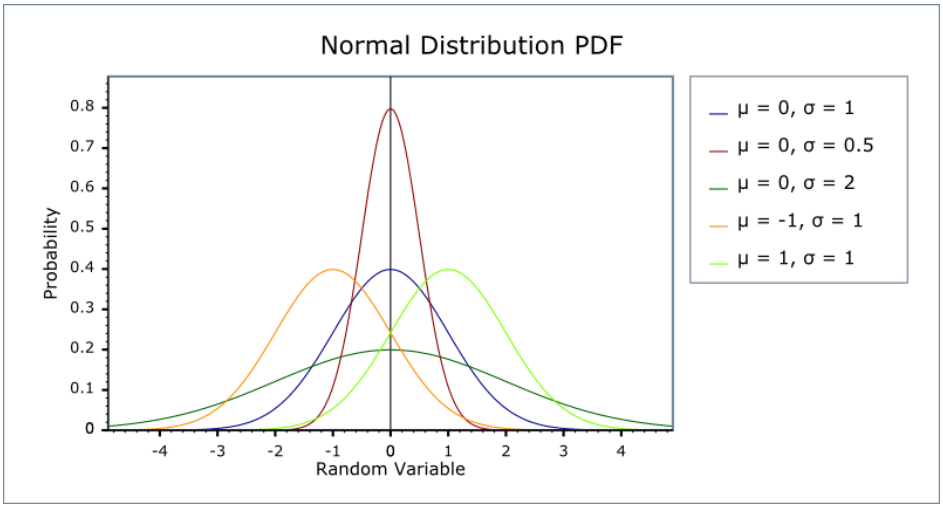


Figure 2.2: Gaussian probability density functions [70]

#### 2.3.1.1 Gausssain Random Variable and Gaussian Process

In the study of random variables, the Gaussian random variables, also known as the normal random variables, stand out as the most commonly employed and highly significant. This is due to their ability to accurately represent a wide range of natural events, physical phenomena, and random occurrences, including noise. Moreover, their widespread use is due in part to the central limit theorem, which states that the sum or average of a large number of independent and identically distributed random variables tends to follow a Gaussian distribution. These variables are characterized by a probability density function (PDF) that follows the well-known bell-shaped curve, often referred to as the Gaussian distribution.

**Definition 11.** *[71] A **Gaussian random variable** is one whose PDF can be written in the general form*

$$f_X(x) = \frac{1}{\sqrt{2\pi\sigma_x^2}} \exp\left( -\frac{(x-\mu_x)^2}{2\sigma_x^2} \right) \tag{2.18}$$

*This PDF of the Gaussian random variable has two parameters, the first moment $\mu_x$ and the second moment $\sigma_x$, which have the interpretation of the mean and standard deviation respectively. The parameter $\sigma_x^2$ is referred to as the variance. These parameters define where the distribution is centered and how it spreads out. Figure 2.2 illustrates some Gaussian distributions with different means and variances.*

A Gaussian random variable is commonly represented by a simplified notation, denoted as $X \sim \mathcal{N}(\mu_x, \sigma_x^2)$.

**Theorem 2.5.** *[72] The n-th central moment (about the mean) of a Gaussian random variable $X \sim \mathcal{N}(\mu_x, \sigma_x^2)$ is zero for odd moments, and for even moments is given by:*

$$\mathbb{E}[(X - \mu_x)^n] = (n-1)!! \cdot \sigma_x^n \tag{2.19}$$

According to this theorem the third central moment of $X \sim \mathcal{N}(\mu_x, \sigma_x^2)$ is zero, and the fourth central moment is $3\sigma_x^4$.

**Definition 12.** *[73] A stochastic process $\{\mathcal{Y}(t) : t \geq 0\}$ is called a **Gaussian process**, if for all $t_1 < t_2 < ... < t_n$ the vector $(\mathcal{Y}(t_1), ..., \mathcal{Y}(t_n))$ is a Gaussian random vector.*

### 2.3.2 Brownian Motion

**Definition 13.** *[74] Suppose $X_1, X_2, ...$ are independent and identically distributed random variables with equal probability having the value of $-1$ or $1$. then*

$$S_n = X_1 + X_2 + ... + X_n, \tag{2.20}$$

*is a simple **random walk** in $\mathbb{Z}$. Random walk represents a discrete-time process where at every individual time unit, there is an identical likelihood of either advancing to the right or regressing to the left on a line.*

The Central Limit theorem yields that as $n$ increases, $S_n$ converges to a normal distribution with zero-mean and variance $n$ (see [74] for the proof).

**Definition 14.** *[75] Discrete-time **Brownian motion** can be defined as the random variable*

$$w(t) = w(0) + \sum_{n=1}^{t} S_n. \tag{2.21}$$

*where* $w(0) \in \mathbb{R}$*, and the increments are* $\Delta w(t) = w(t) - w(t-1) = S_t$*, thus* $\mathbb{E}[\Delta w(t)] = 0$*.*

Continuous Brownian motion is essentially the continuous-time version of a random walk where one decreases both the time intervals and the magnitude of each step. Therefore, in the limit, the process evolves from discrete-time to continuous-time. Mathematically, let $\Delta t = k^{-1}$ for $k \neq 0$, and $\Delta w_k(n)$ for each increment $n \in \mathbb{N}$ be equal to either $\sqrt{\Delta t}$ or $-\sqrt{\Delta t}$ with equal probability.

$$w(t) = w(kt\Delta t) = w_k(t) = w(0) + \sum_{n=1}^{kt} \Delta w_k(n) \tag{2.22}$$

Continuous-time is thus divided into increments of $\Delta t$ units. If $w(0)$ is known with probability 1, one can write the following for the expected value and variance of $w_k(t)$:

$$\mathbb{E}[w_k(t)] = \mathbb{E}[w(0)] + \sum_{n=1}^{kt} \mathbb{E}[\Delta w_k(n)] = w(0) \tag{2.23}$$

$$\mathbb{E}\Big[\Big(w_k(t) - \mathbb{E}[w_k(t)]\Big)^2\Big] = \sum_{n=1}^{kt} \mathbb{E}\left[\big(\Delta w_k(n)\big)^2\right] = \sum_{n=1}^{kt} \left(\frac{1}{2}(\sqrt{\Delta t})^2 + \frac{1}{2}(-\sqrt{\Delta t})^2\right) = t \tag{2.24}$$

Continuous-time Brownian motion is $W(t) = \lim_{k\to\infty} w_k(t)$ which is a stochastic process, that is a collection of random variables indexed by time. A more rigorous definition of continuous-time Brownian motion is provided as follows.

**Definition 15.** *[73] If the following holds, a vector-valued stochastic process* $\{W(t) \in \mathbb{R}^n : t \geq 0\}$ *starting at* $W_0 \in \mathbb{R}^n$ *is referred to as n-dimensional Brownian motion (also called Wiener process):*

- $W(0) = W_0$*, and* $\mathbb{E}[W(t)] = W_0$*.*
- *The process has independent increments, i.e. for every choice of non-negative real* $0 \leq t_1 \leq t_2 \leq ... \leq t_m$*, the increments* $W(t_m) - W(t_m - 1)$*,* $W(t_m - 1) - W(t_m - 2)$*, ...,* $W(t_2) - W(t_1)$ *are independent random vectors.*

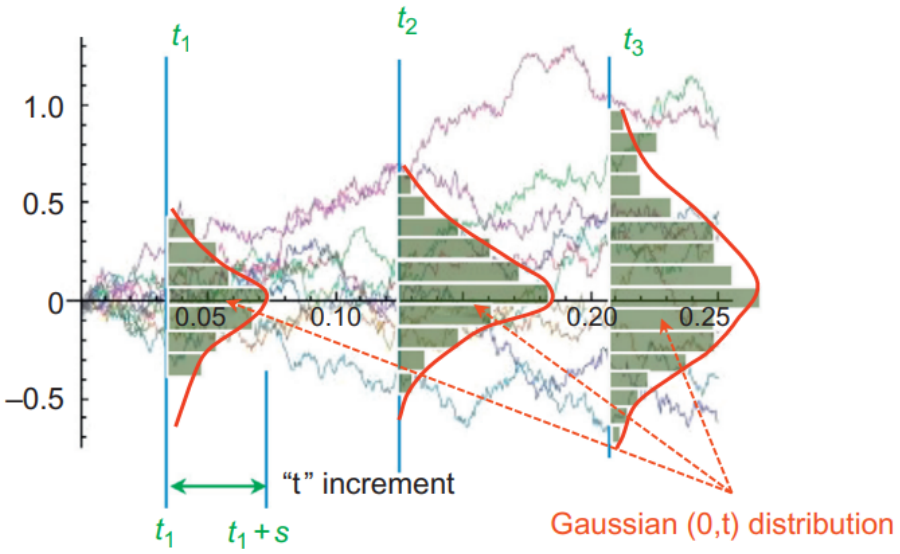


Figure 2.3: Gaussian distributions of Brownian motion [76].

- *The increments* $W(t+h) - W(t)$ *are normally distributed with expectation zero (zero-mean Gaussian) and variance* $nh > 0$ *for all* $t \geq 0$ *(Please see Figure 2.3).*
- *The function* $t \to W(t)$ *is continuous almost surely (with probability one).*

*If* $n = 1$*, then the Brownian motion is called one-dimensional Brownian motion, and if* $W_0 = 0$*, then the Brownian motion is called a standard Brownian motion (denoted by* $\bar{W}$*).*

*Remark. [75]* For each $0 < t_1 < t_2$,

$$\mathbb{E}\left[\left(\left(W(t_2) - W(t_1)\right)^T \left(W(t_2) - W(t_1)\right)\right)^2\right] = n(n+2)(t_2 - t_1)^2. \tag{2.25}$$

The graphical representation of different Brownian motions is shown in Figure 2.4. The top panel depicts the standard Brownian motion, characterized by its zero mean and its variance expanding over time, with the sample paths contained within the quantiles $1, 5, 10, 90$, and 95%. The PDF on the right illustrates the normal distribution of the endpoints of the paths centered at the initial value $X_0$ of 0. The middle panel shows Brownian motion with a constant drift where the mean path is linear. The PDF here reflects the normal distribution of the paths' endpoints, skewed by the drift. The bottom panel shows a Brownian motion with

a linear drift, resulting in geometric Brownian motion, marked by an exponential increase in the average path. This results in a log-normal distribution of the final values, indicating the non-negative nature of the process.

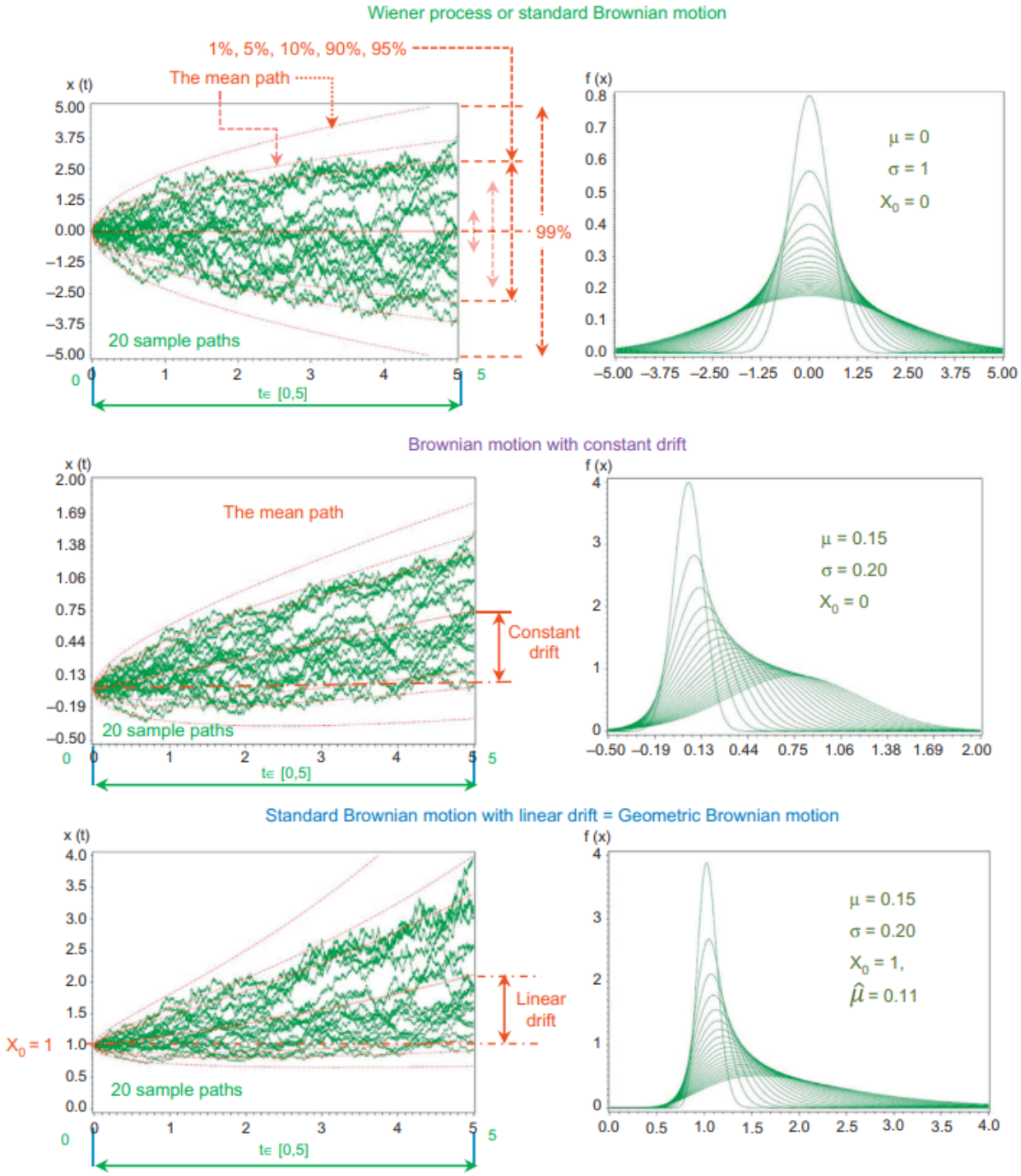


Figure 2.4: Graphical representations of different Brownian motions [76].

**Theorem 2.6.** *Even though Brownian motion $t \to W(t)$ is everywhere continuous, it is nowhere differentiable almost surely. (See [77] for proof.)*

**Lemma 2.1.** *[77] (Scaling Invariance). Suppose $\{\bar{W}(t) : t > 0\}$ is a standard Brownian motion and let $\alpha > 0$. Then the process $\{X(t) : t > 0\}$ defined by $X(t) = \frac{1}{\alpha}\bar{W}(\alpha^2 t)$ is also a standard Brownian motion.*

**Theorem 2.7.** *[73] Brownian motion with start in $W_0 \in \mathbb{R}$ is a Gaussian process.*

**Definition 16.** *[78] Consider the following Gaussian process for every $n \in \mathbb{N}$*

$$\xi_t^{(n)} := n\Big(W(t) - W(t - 1/n)\Big); \quad 0 \leq t < \infty \tag{2.26}$$

*with $\mathbb{E}\Big[\xi_t^{(n)}\Big] = 0$ and covariance $\mathbb{E}\Big[\xi_t^{(n)}\xi_\tau^{(n)}\Big] = Q_n(t-\tau)$, where*

$$Q_n(s) = \begin{cases} n^2(\frac{1}{n} - s); & |s| \leq 1/n \\ 0; & |s| \geq 1/n \end{cases} \tag{2.27}$$

*as $n \to \infty$, the sequence of functions $\{Q_n\}_{n=1}^{\infty}$ approaches the Dirac delta. In a generalized, distributional sense,*

$$\xi_t = \lim_{n\to\infty} \xi_t^{(n)} \tag{2.28}$$

*is a zero-mean Gaussian process with covariance $\mathbb{E}\big[\xi_t\xi_\tau\big] = \delta(t-\tau)$ and it is called **White Noise**.*

It has been shown in [66, 79, 80], that if $\bar{\xi}(t)$ is a standard white Gaussian noise, it is the formal derivative of the Brownian motion. Thus, we have:

$$d\bar{W}(t) = \bar{\xi}(t)dt \tag{2.29}$$

where $d\bar{W}(t)$ represents infinitesimal displacements of standard Brownian motion with $\mathbb{E}[d\bar{W}(t)] =$

0, $\mathbb{E}[d\bar{W}(t)^2] = dt$. For the white noise $\xi$ with the variance $\sigma^2$, we have:

$$dW(t) = \xi(t)dt = \sigma\bar{\xi}(t)dt \tag{2.30}$$

where $dW(t)$ represents infinitesimal displacements of Brownian motion with $\mathbb{E}[dW(t)] = 0$, $\mathbb{E}[dW(t)^2] = \sigma^2 dt$.

### 2.3.3 Stochastic differential equations

In standard calculus, a differential equation representing a continuous dynamical system with a finite-dimensional state is of the form

$$\frac{df(t)}{dt} = G(t, f(t)), \quad t \geq t_0 \tag{2.31}$$

where $G(t, f(t))$ is the rate of the change with respect to $t$ of the function $f(t)$, which can depend on both $t$, and the value of $f$ at time $t$. Given an initial condition, the value of $f(t)$ can be described as

$$f(t) = f(t_0) + \int_{t_0}^{t} G(\tau, f(\tau))d\tau, \tag{2.32}$$

which can be calculated either directly by analytically solving the integral or the main differential equation if possible, or by using numerical methods.

In stochastic calculus, the dynamical system in equation (2.31) subject to random disturbances can be described by a stochastic differential equation (SDE) of the form

$$\frac{dX_t}{dt} = G\big(t, \xi(t), X_t\big), \quad t \geq t_0 \tag{2.33}$$

where $X_t$ is a stochastic process and $\xi(t)$ is the white Gaussian noise. An important special case of equation (2.33) is the following SDE with additive noise.

$$\frac{dX_t}{dt} = F(t, X_t) + \sigma(t, X_t)\xi(t), \quad t \geq t_0 \tag{2.34}$$

where the term $F(t, X_t)$ is called the *drift*, and $\sigma(t, X_t)$ is the *diffusion* term. The white Gaussian process $\xi(t)$ is not mean square Riemann integrable and equation (2.34) lacks any mathematical meaning [66]. Consequently, using equation (2.30), one can rewrite equation (2.34) and consider the formally equivalent SDE of the form

$$dX_t = F(t, X_t)dt + \sigma(t, X_t)dW(t), \quad t \geq t_0, \tag{2.35}$$

where $W(t)$ is a Brownian motion. It can be inferred from this SDE that the process $X_t$ evolves at time $t$ similar to a Brownian motion with drift $F(t, X_t)$, and variance $\sigma(t, X_t)^2$. Given an initial condition, the process $X_t$ can be described as

$$X_t = X_{t_0} + \int_{t_0}^{t} F(\tau, X_\tau)d\tau + \int_{t_0}^{t} \sigma(\tau, X_\tau)dW(\tau), \tag{2.36}$$

where the first integral is a standard calculus integral (Riemann integral) and the second integral defined in a mean square sense is the stochastic ($Itô$) integral [81]. One of the $Itô$ stochastic integration results is

$$\begin{aligned} \int_a^b df(t, W(t)) &= \sum_{t_i} f(t_{i+1}, W(t_{i+1})) - f(t_i, W(t_i)) \\ &= f(b, W(b)) - f(a, W(a)) \end{aligned} \tag{2.37}$$

(Proof: [82])

### 2.3.4 Fokker-Planck-Kolmogorov Equation

The Fokker-Planck equation describes the time evolution of the probability density function (PDF). The solution of the SDE (2.35), is a stochastic process, and the probability density of an $Itô$ process $X_t$ can be found by deriving the Fokker-Planck-Kolmogorov equation.

**Theorem 2.8.** *[83] (Fokker-Planck-Kolmogorov equation). The probability density* $p(t, X_t)$

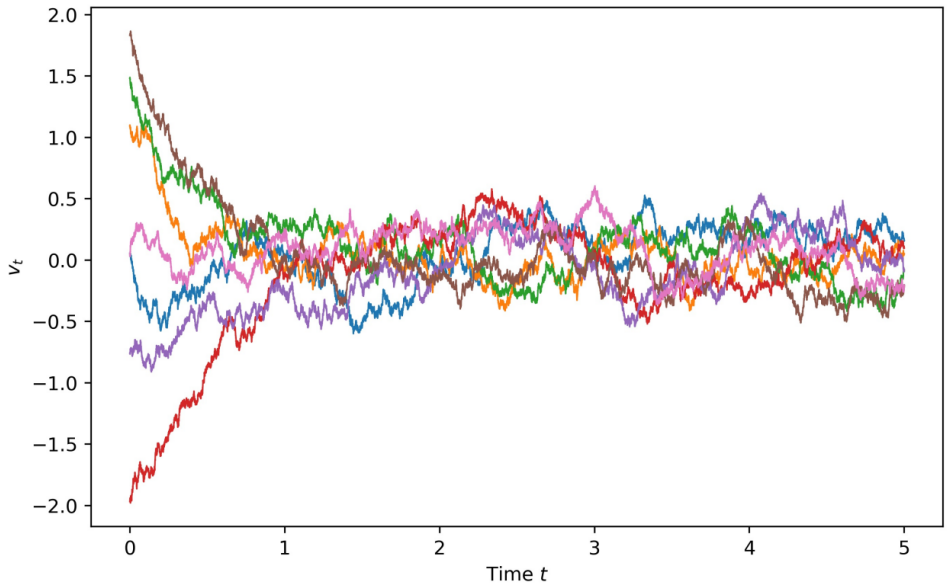


Figure 2.5: Simulation of the Ornstein-Uhlenbeck process [84]

*of the solution of the SDE in equation* (2.35) *solves the partial differential equation (PDE):*

$$\frac{\partial p(t, X_t)}{\partial t} = -\frac{\partial}{\partial X_t}\Big(F(t, X_t)p(t, X_t)\Big) + \frac{1}{2}\frac{\partial^2}{\partial X_t^2}\Big(D(t, X_t)p(t, X_t)\Big), \tag{2.38}$$

*where* $F(t, X_t)$ *is the drift coefficient,* $D(t, X_t) = \sigma_W^2\sigma^2(t, X_t)$ *is the diffusion coefficient with* $\sigma_W^2$ *being the variance or intensity of the Brownian motion. This PDE is called the Fokker–Planck–Kolmogorov (FPK) equation and is an initial value problem with the given initial condition* $p(t_0, X_{t_0})$ *at time* $t = t_0$*. (For proof see [83].)*

**Definition 17.** *[83] The stationary distribution of the solution of the FPK equation* (2.38) *when it exists is the probability density function* $p_s(X_t)$ *that does not change with time. Thus, the time derivative of the PDF is zero, i.e.,*

$$\frac{\partial p_s(X_t)}{\partial t} = 0.$$

**Example 2.1.** [84] The Ornstein-Uhlenbeck process is a stochastic differential equation used to model the velocity of a particle under the influence of friction and random forces,

whose mean value reverts over time. The Fokker-Planck-Kolmogrov equation for this process describes the time evolution of the probability density function $p(t, V_t)$ for the velocity $V_t$ at time $t$.

Given a stochastic differential equation (SDE) for the Ornstein-Uhlenbeck process in the form [84]:

$$dV_t = \left(-\frac{\xi}{m}V_t\right)dt + \frac{\sqrt{2\sigma^2}}{m}d\bar{W}_t, \tag{2.39}$$

where $V_t$ is the velocity, $\xi$ is the friction coefficient, $m$ is the mass, $\sigma^2$ is the variance of the process, and $d\bar{W}_t$ represents the increment of a Wiener process (standard Brownian motion). Substituting $F(t, V_t) = -\frac{\xi}{m}V_t$, and the term $D(t, V_t) = \frac{2\sigma^2}{m^2}$ into equation (2.38), we have:

$$\begin{aligned}\frac{\partial p(t, V_t)}{\partial t} &= -\frac{\partial}{\partial V_t}\left(-\frac{\xi}{m}V_t.p(t, V_t)\right) + \frac{1}{2}\frac{\partial^2}{\partial V_t^2}\left(\frac{2\sigma^2}{m^2}.p(t, V_t)\right), \\ &= -\frac{\xi}{m}\frac{\partial}{\partial V_t}\Big(V_t.p(t, V_t)\Big) + \frac{\sigma^2}{m^2}\frac{\partial^2 p(t, V_t)}{\partial V_t^2}\end{aligned} \tag{2.40}$$

The stationary distribution $p_s(V_t)$ satisfies the condition $\frac{\partial p_s(V_t)}{\partial t} = 0$, indicating that $p_s(V_t)$ does not change with time. For the stationary case, the Fokker-Planck equation simplifies to the following ordinary differential equation (ODE):

$$0 = -\frac{\xi}{m}\frac{\partial}{\partial V_t}\Big(V_t.p(t, V_t)\Big) + \frac{\sigma^2}{m^2}\frac{\partial^2 p(t, V_t)}{\partial V_t^2}. \tag{2.41}$$

We can conclude that a process is stationary if this equation has a unique solution.

By integrating this equation we have,

$$\frac{\sigma^2}{m\xi}\frac{\partial p(V_t)}{\partial V_t} + V_t.p(V_t) = C, \tag{2.42}$$

where $C$ is an integration constant. The solution of this first order ODE for $p_s(V_t)$ is then given by

$$p(V_t) = e^{-\frac{m\xi V_t^2}{2\sigma^2}}\left(\frac{m\xi C}{\sigma^2}\int e^{\frac{m\xi V_t^2}{2\sigma^2}}dV_t + K\right). \tag{2.43}$$

where $K$ is a constant. The normalization condition $\int_{-\infty}^{\infty} p_s(V_t)dV_t = 1$, and the non-negativity condition $p_s(V_t) \geq 0$ for all $V_t$ imply that $C$ must be 0 and $K = \frac{1}{\sqrt{2\pi\frac{\sigma^2}{m\xi}}}$. This conclusion arises because any non-zero value of $C$ would affect the asymptotic behavior of $p_s(V_t)$ by making it unbounded, causing the violation of these constraints. Consequently, the stationary distribution of the Ornstein-Uhlenbeck process is Gaussian:

$$p_s(V_t) = \frac{1}{\sqrt{2\pi\frac{\sigma^2}{m\xi}}} \exp\left(-\frac{V_t^2}{2\frac{\sigma^2}{m\xi}}\right), \tag{2.44}$$

with mean 0 and variance $\frac{\sigma^2}{m\xi}$. The stationarity can be seen in Figure 2.5 where this process is simulated with various initial conditions.

## 2.4 State Estimation

In many practical scenarios, the accurate estimation of the current state of a dynamical system is of paramount importance. This necessity arises either for the design of a controller or for the real-time acquisition of system information, serving as a basis for decision-making or surveillance. A prevalent approach to address this problem involves using sensors on or within the physical system. The ultimate aim is to construct a reliable estimation of the entire system state based on this sensor data. Notably, the feasibility of implementing such an algorithm depends on the premise that the measurements from the sensors possess sufficient information to uniquely determine the system's state, namely observability.

The process of designing an observer is guaranteed through the observability property. This property essentially enables the determination of the initial state vector of the system by having access to information about the system's input and the resulting output over an interval of time. While the observability of linear systems is independent of the input, this is typically not the case for nonlinear systems, and one must take into account inputs that distinguish the states, specifically, inputs that produce distinct outputs. In other words,

these inputs must be properly selected in a way that they generate distinct outputs under different system states. This distinction is necessary to establish observability in nonlinear systems; please see [85].

### 2.4.1 Linear Time-Varying System

Consider a linear time-variant (LTV) system with the state space model

$$\begin{aligned} \dot{\boldsymbol{x}}(t) &= A(t)\boldsymbol{x}(t) + B(t)\boldsymbol{u}(t) \\ \boldsymbol{y}(t) &= C(t)\boldsymbol{x}(t) + D(t)\boldsymbol{u}(t) \end{aligned} \tag{2.45}$$

where $\boldsymbol{x}(t) \in \mathbb{R}^n$ is the state, $\boldsymbol{u}(t) \in \mathbb{R}^m$ represents the input, $\boldsymbol{y}(t) \in \mathbb{R}^p$ is the output, and the matrices $A(t), B(t), C(t)$, and $D(t)$ are the time varying state space matrices.

#### 2.4.1.1 Observability

The assessment of observability for time-varying systems is closely tied to finite time intervals. Various observability concepts and definitions have been developed in this regard, and the reader can refer to [86], [87], [88], and [89] for different perspectives and approaches to characterizing observability in time-varying systems.

**Definition 18.** *[64] An LTV system is called observable on $[t_0, T]$ if any initial state $\boldsymbol{x}(t_0)$ is uniquely determined by the input $\boldsymbol{u}(t)$ and the output $\boldsymbol{y}(t)$ for $t \in [t_0, T]$.*

The concept of uniform observability is of significant importance, as it guarantees the well-conditioning and solvability of the state estimation process via the design of exponentially stable observers.

**Assumption 2.1.** *The matrix-valued functions $A(t), B(t), C(t)$, and $D(t)$ of the LTV system (2.45) are continuous and bounded on $[0, +\infty)$,*

**Definition 19.** *[90] The LTV system (2.45) (the pair $A(\cdot), C(\cdot)$) under Assumption 2.1 is*

*uniformly completely observable if there exist* $\tau, \delta > 0$ *such that*

$$\forall t \geq 0, \qquad 0 < \delta I \leq W(t, t+\tau) := \int_t^{t+\tau} \Psi(s,t)^T C^T(s) C(s) \Psi(s,t)\, ds \tag{2.46}$$

*with* $\Psi(s,t)$ *as the state transition matrix of* $\dot{\boldsymbol{x}} = A(t)\boldsymbol{x}$ *and* $I$ *as the identity matrix. The matrix* $W$ *is referred to as the observability Grammian of the system.*

Evaluating the uniform observability of a time-varying linear system (LTV) can be complex, as calculating the Gramian necessitates the integration of solutions of $\dot{\boldsymbol{x}} = A(t)\boldsymbol{x}$. Therefore, it is well-established to use the observability properties of LTV systems which are related to the attributes of the observability matrix $\mathcal{O}(t)$ defined in Theorem 2.9.

**Theorem 2.9.** *The system* (2.45) *is observable for a specific time* $\bar{t} \in (t_0, T]$ *if* $Rank\Big(\mathcal{O}(\bar{t})\Big) = n$*, where* $n$ *is the order of the system, and* $\mathcal{O}(t) := \begin{bmatrix} \mathcal{O}_0(t) \\ \mathcal{O}_1(t) \\ \vdots \\ \mathcal{O}_{n-1}(t) \end{bmatrix}$ *with* $\mathcal{O}_0(t) = C(t)$, $\mathcal{O}_i(t) = \mathcal{O}_{i-1}(t)A(t) + \dot{\mathcal{O}}_{i-1}(t)$, $i = 1, ..., n-1$. *(Proof: [64])*

The instantaneous observability at $t$ is guaranteed using Theorem 2.9. However, uniform observability cannot be characterized only in terms of rank conditions, unless one can prove $Rank\Big(\mathcal{O}(t)\Big) = n$ for all $t$. For general LTV systems, a sufficient condition for uniform observability is stated in Theorem 2.10 and Proposition 2.1.

**Proposition 2.1.** *[91] Consider an LTV system* (2.45) *satisfying Assumption 2.1. Suppose there exists a positive integer* $K$ *such that*

1. *The* $k$*-th order derivative of* $A$ *(resp.* $C$*) is well-defined and bounded on* $[0, +\infty)$ *up to* $k = K$ *(resp. up to* $k = K+1$*).*

2. *There exists an* $n \times n$ *matrix* $\mathcal{O}(t)$ *defined in Theorem 2.9 and two scalars* $\bar{\delta}, \bar{\tau} > 0$

*such that*

$$\forall t \geq 0, \qquad 0 < \bar{\delta} \leq \int_t^{t+\bar{\tau}} \left| det(\mathcal{O}(s)) \right| ds. \tag{2.47}$$

*Then, this system is uniformly observable.*

**Theorem 2.10.** *[86] The bounded LTV system* (2.45) *(under Assumption 2.1) is uniformly completely observable if there exists a positive scalar* $\bar{\delta} > 0$ *such that*

$$\forall t \geq 0, \qquad 0 < \bar{\delta}\mathbf{I} \leq \mathcal{O}^T(t)\mathcal{O}(t) \tag{2.48}$$

*where* $\mathcal{O}(t)$ *is defined in Theorem 2.9 and* $\mathbf{I}$ *is the identity matrix.*

**Theorem 2.11.** *[91] For a time-varying linear system* (2.45) *that satisfies Assumption 2.1, the following properties hold:*

1. *The pair* $\Big(A(\cdot), C(\cdot)\Big)$ *is uniformly observable if and only if the pair* $\Big(A(\cdot) - LC(\cdot), C(\cdot)\Big)$ *is uniformly observable, where* $L(\cdot)$ *is any bounded matrix-valued time-function.*

2. *If the pair* $\Big(A(\cdot), C(\cdot)\Big)$ *is uniformly observable, then for any* $a > 0$*, there exists a bounded matrix* $L_a(t)$ *such that the linear observer*

$$\dot{\hat{\boldsymbol{x}}} = A(t)\hat{\boldsymbol{x}} + L_a(t)(\boldsymbol{y} - C(t)\hat{\boldsymbol{x}})$$

*is uniformly exponentially stable with a convergence rate determined by "*$a$*", i.e. there exists* $c_a > 0$ *such that*

$$\|\hat{\boldsymbol{x}}(t) - \boldsymbol{x}(t)\| \leq c_a e^{-a(t-t_0)} \|\hat{\boldsymbol{x}}(t_0) - \boldsymbol{x}(t_0)\|,$$

*for any* $t \geq t_0$ *and any initial conditions* $\boldsymbol{x}(0)$ *and* $\hat{\boldsymbol{x}}(0)$*.*

**Example 2.2.** Consider the following LTV state-space model:

$$\begin{aligned}
\begin{bmatrix} \dot{x}(t) \\ \dot{y}(t) \end{bmatrix} &= \begin{bmatrix} 0 & 0 \\ u(t) & 0 \end{bmatrix} \begin{bmatrix} x(t) \\ y(t) \end{bmatrix} + \begin{bmatrix} 1 \\ 0 \end{bmatrix} u(t) \\
y(t) &= \begin{bmatrix} 0 & 1 \end{bmatrix} \begin{bmatrix} x(t) \\ y(t) \end{bmatrix},
\end{aligned} \tag{2.49}$$

where $x(t)$ and $y(t)$ are the states, and $u(t)$ and $z(t)$ represent the input and output of the system respectively. For the instantaneous observability of this system we have

$$\begin{aligned}
&\mathcal{O}_0(t) = C(t) = \begin{bmatrix} 0 & 1 \end{bmatrix}, \\
&\mathcal{O}_1(t) = \mathcal{O}_0(t)A(t) + \dot{\mathcal{O}}_0(t) = \begin{bmatrix} 0 & 1 \end{bmatrix} \begin{bmatrix} 0 & 0 \\ u(t) & 0 \end{bmatrix} = \begin{bmatrix} u(t) & 0 \end{bmatrix}, \\
&\mathcal{O}(t) = \begin{bmatrix} 0 & 1 \\ u(t) & 0 \end{bmatrix}.
\end{aligned} \tag{2.50}$$

When $u(t) \neq 0$ for $t \in [t_1, t_2]$ with $t_1 \geq 0,\ t_2 > t_1$, rank of $\mathcal{O}(t)$ is equal to 2. Therefore, the system has instantaneous observability (Theorem 2.9). For uniform observability, if we design the input to be $u(t) = u_0 t^\alpha$ with $u_0 > 0$ and integer $\alpha \geq 0$, we have

$$\int_0^T \left|\det(\mathcal{O}(t))\right| dt = \int_0^T u_0 t^\alpha ds = \frac{u_0 T^{\alpha+1}}{\alpha+1} \geq \bar{\delta} > 0. \tag{2.51}$$

Since there exists a $T > 0$ and $\bar{\delta} = \frac{u_0 T^{\alpha+1}}{\alpha+1}$ satisfying the inequality (2.51), the LTV system in (2.49) is uniformly observable with the designed input (Proposition 2.1).

The instantaneous observability rank condition is necessary and sufficient for the observability of Linear Time-Invariant (LTI) systems. In Example 2.2, considering the constant input $u(t) = u_0 > 0$, the system (3.4) becomes an LTI system and the rank condition for $\mathcal{O}(t)$ is sufficient and necessary. However, Example 2.3 shows an LTV system that exhibits

instantaneous observability at most time instances but fails to achieve uniform observability.

**Example 2.3.** Consider a linear time-varying (LTV) system described by the following state-space representation:

$$\begin{bmatrix} \dot{x}(t) \\ \dot{y}(t) \end{bmatrix} = \begin{bmatrix} 0 & \sin(t) \\ 0 & 0 \end{bmatrix} \begin{bmatrix} x(t) \\ y(t) \end{bmatrix} + \begin{bmatrix} 0 \\ 1 \end{bmatrix} u(t), \tag{2.52}$$
$$z(t) = \begin{bmatrix} 1 & 0 \end{bmatrix} \begin{bmatrix} x(t) \\ y(t) \end{bmatrix}.$$

The observability matrix $\mathcal{O}(t)$ for this system is:

$$\mathcal{O}(t) = \begin{bmatrix} 1 & 0 \\ 0 & \sin(t) \end{bmatrix}. \tag{2.53}$$

The rank of $\mathcal{O}(t)$ is 2 (full rank) for $t \neq n\pi, n \in \mathbb{Z}$, ensuring instantaneous observability at these points. However, at $t = n\pi$, the rank of $\mathcal{O}(t)$ reduces to 1 due to the zero value of $\sin(t)$. For uniform observability, the system's observability matrix must maintain full rank across the entire time domain. In this example, the existence of points ($t = n\pi$) where the observability matrix's rank is less than the system's order 2 implies the system does not satisfy the condition for uniform observability. The system's state cannot be fully determined from the output $z(t)$ at these points.

#### 2.4.1.2 Kalman-Bucy Filter

In this section, the continuous-time Kalman-Bucy filter and its usual assumptions are recalled. The Kalman filter in continuous-time is designed for LTV systems modeled by

$$\begin{aligned} \dot{\boldsymbol{x}}(t) &= A(t)\boldsymbol{x}(t) + B(t)\boldsymbol{u}(t) + Q^{\frac{1}{2}}\boldsymbol{\omega}(t) \\ \boldsymbol{y}(t) &= C(t)\boldsymbol{x}(t) + D(t)\boldsymbol{u}(t) + R^{\frac{1}{2}}\boldsymbol{v}(t) \end{aligned} \tag{2.54}$$

where $t \in \mathbb{R}$ represents time, $\boldsymbol{x}(t) \in \mathbb{R}^n$ is the state vector, $\boldsymbol{u}(t) \in \mathbb{R}^l$ is the bounded input, $\boldsymbol{y}(t) \in \mathbb{R}^m$ is the output, and $\boldsymbol{\omega}(t) \in \mathbb{R}^n$ and $\boldsymbol{v}(t) \in \mathbb{R}^m$ are two independent white noise processes with identity covariance matrices. The matrices $A(t), B(t), C(t), Q(t)$,and $R(t)$ are bounded real matrices of appropriate sizes. Moreover, $Q(t)$ and $R(t)$ are symmetric positive semi-definite matrices. The initial condition $\boldsymbol{x}(t_0) \in \mathbb{R}^n$ is an initial state vector following the Gaussian distribution $\boldsymbol{x}(t_0) \sim \mathcal{N}(\boldsymbol{x_0}, P_0)$ with $\boldsymbol{x_0} \in \mathbb{R}^n$ and $P_0 \in \mathbb{R}^{n\times n}$.
The Kalman-Bucy filter [92] for this LTV system is as follows

$$\dot{\hat{\boldsymbol{x}}}(t) = A(t)\hat{\boldsymbol{x}}\,dt + B(t)\boldsymbol{u}(t)\,dt + K(t)\big(\boldsymbol{y}(t) - C(t)\boldsymbol{x}(t)\big) \tag{2.55}$$

$$K(t) = P(t)C^T(t)R^{-1}(t) \tag{2.56}$$

$$\frac{d}{dt}P(t) = A(t)P(t) + P(t)A^T(t) - P(t)C^T(t)R^{-1}(t)C(t)P(t) + Q(t) \tag{2.57}$$

$$\hat{\boldsymbol{x}}(t_0) = \hat{\boldsymbol{x}}_0, \quad P(t_0) = P_0, \tag{2.58}$$

where the solution of the Riccati Equation (2.57) is represented as a matrix function, denoted as $P(t) \in \mathbb{R}^{n\times n}$, while $K(t) \in \mathbb{R}^{n\times m}$ is the Kalman gain. The Kalman filter is well-recognized for its optimal properties with respect to estimating the state of a linear dynamic system in the presence of Gaussian noise. Furthermore, it is established that $P(t)$ remains bounded. The dynamics of the Kalman filter are stable under the conditions that the matrix pair $(A(t), Q(t)^{1/2})$ is uniformly completely controllable (see [93] for definition), and the matrix pair $(A(t), C(t))$ is uniformly completely observable (equivalent to uniformly observable under Assumption 2.1) [10,2]. Stability in this context firstly means the error covariance matrix converges to a steady-state value or remains bounded over time. Secondly, the estimation error does not grow unbounded over time (either remains bounded or converges to zero).

**Example 2.4.** This example outlines the design of the Kalman-Bucy filter for the system (2.49) with constant input $u(t) = u_0$. Assuming the process and measurement noise are

white noise processes with covariance matrices given by:

$$Q(t) = 0.01 \cdot \mathbf{I}_2, \quad R(t) = 0.01, \tag{2.59}$$

where $\mathbf{I}_2$ is the $2 \times 2$ identity matrix. Assume the initial conditions $\hat{x}(0) = [0, 0]^T$ and $P(0) = \mathbf{I}_2$. Initially, at $t_0 = 0$ we have:

$$K(0) = P(0)C^T R^{-1} = \begin{bmatrix} 1 & 0 \\ 0 & 1 \end{bmatrix} \begin{bmatrix} 0 \\ 1 \end{bmatrix} \cdot 100 = \begin{bmatrix} 0 \\ 100 \end{bmatrix}. \tag{2.60}$$

The steady-state Kalman gain $K_{ss}$ can be calculated by solving the following Algebraic Ricatti Equation (ARE)

$$0 = AP_{ss} + P_{ss}A^T - P_{ss}C^T R^{-1} C P_{ss} + Q, \tag{2.61}$$

This equation does not involve derivatives of $P$ with respect to time. Using numerical methods, we obtain the steady-state error covariance matrix $P_{ss}$ and the steady-state Kalman gain $K_{ss}$ as follows:

$$P_{ss} = \begin{bmatrix} 6.21 \times 10^{14} & 1.01 \times 10^{-3} \\ 1.01 \times 10^{-3} & 1 \times 10^{-2} \end{bmatrix}, \quad K_{ss} = \begin{bmatrix} 0.101 \\ 1 \end{bmatrix} \tag{2.62}$$

Here, we used Python programming language, specifically the "*scipy*" library [94], which provides numerical methods for solving Riccati equations. The function "*solve_continuous_are*" from "*scipy.linalg*" is used to find the solution of equation (2.61). This function internally uses an advanced method based on the Schur decomposition (detailed in [95]), which involves decomposing the matrix into a form that simplifies the Riccati equation. (Please refer to [96] for more information about this library and its functions.)

### 2.4.2 Observability of Nonlinear Systems

Typically, the observability of a nonlinear system is a local problem and can be characterized by the conventional observability rank condition as outlined in [85]. However, this condition is insufficient for the design of an observer since it tightly depends on the input used in the system. In such cases, the design of an observer is limited to specific classes of inputs that are deemed suitable. These inputs are typically referred to as "regular" or "persistently exciting" inputs, see [97], [98], [99], and [100].

## 2.5 Population Dynamics

A population is a collection of members of the same species that reside in a certain area. The logistic equation models bacterial, plant, animal, and human population expansion, bound by the maximum population size (carrying capacity). The autonomous Verhulst logistic equation has the form [101]

$$\dot{N}(t) = N(t)\big(a - bN(t)\big), \;\; t \geq 0, N(0) = N_0 > 0, \tag{2.63}$$

The non-autonomous Verhulst logistic equation is usually denoted by [101]

$$\dot{N}(t) = N(t)\big(a(t) - b(t)N(t)\big), \;\; t \geq 0, N(0) = N_0 > 0, \tag{2.64}$$

where $N(t)$ is the population, $N_0 > 0$ is the initial condition, $a$ is the nonzero rate of growth and $\frac{a}{b} = K$ is the carrying capacity where $b \neq 0$. In the case of $N_0 < K$, both $a(t)$ and $b(t)$ are positive continuous functions. The population with a positive growth rate grows and converges to the carrying capacity (blue line in Figure 2.6). When $N_0 > K$, the growth rate $a(t)$, and $b(t)$ are negative. In this case, the population decreases and converges to the carrying capacity (orange line in Figure 2.6).

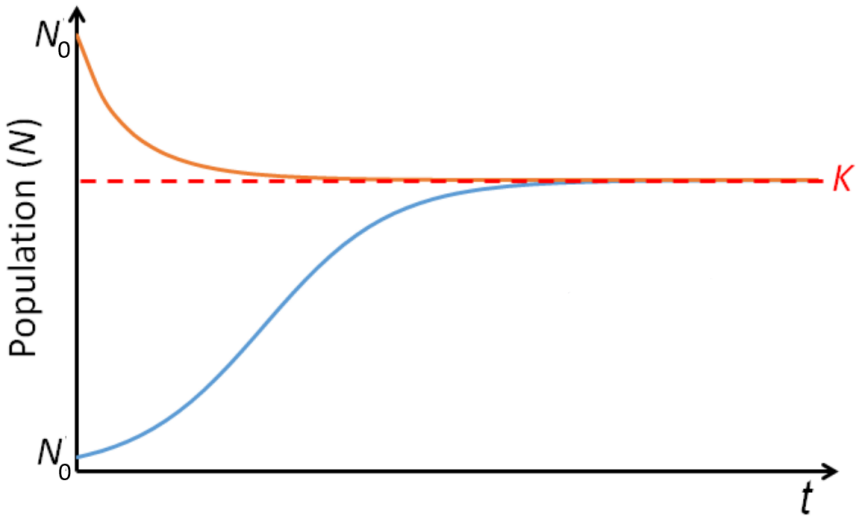


Figure 2.6: Typical logistic curves for positive and negative growth [103]

The solution of the ODE (2.64) is given by [102]:

$$N(t) = \frac{N_0 \exp\left(\int_0^t a(s)\,ds\right)}{1 + N_0 \int_0^t \exp\left(\int_0^s a(\nu)\,d\nu\right) b(s)\,ds}, \tag{2.65}$$

Typically, This model is stochastically perturbed in two ways. The first one is additive noise and the model can be described as follows

$$dN(t) = N(t)\Big[\big(a(t) - b(t)N(t)\big)dt\Big] + \sigma(t)dW(t), \;\; t \geq 0, \tag{2.66}$$

where $W(t)$ is $1-$dimensional standard Brownian motion with $W(0) = 0$, $N(0) = N_0$ and $N$ is a positive random variable. Here $a(t)$, $b(t)$, and $\sigma(t)$ are bounded continuous functions defined on $t \in [0, \infty)$. It is reasonable to assume that $N_0$ is independent of $W(t)$.

The second model is perturbed by multiplicative noise. Suppose that parameter a(t) is stochastically perturbed as

$$a(t) + \xi(t) \tag{2.67}$$

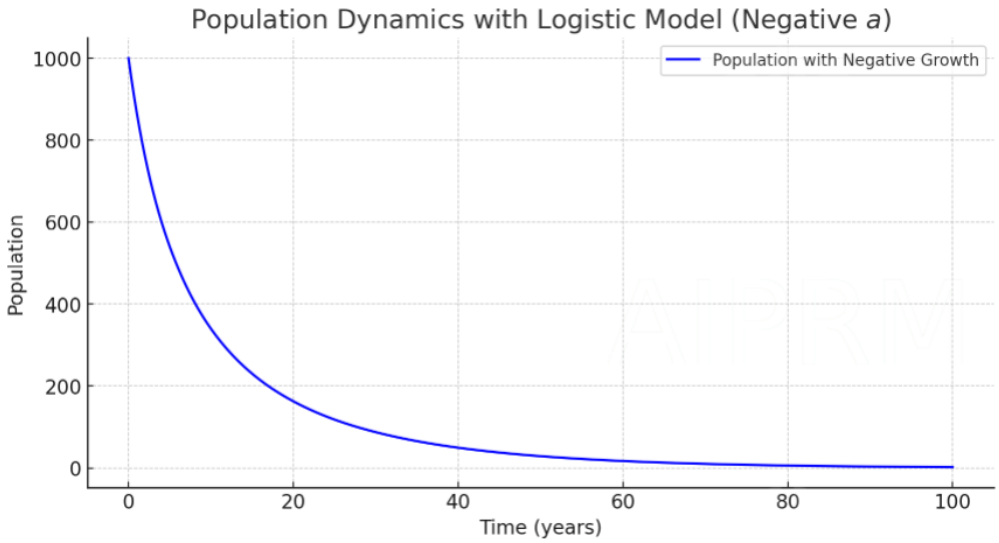


Figure 2.7: Population dynamics over 100 years with a negative growth rate using the Verhulst logistic model.

where $\xi(t)$ is zero-mean white noise with the variance or intensity of $\sigma^2(t)$. Then using equation (2.30), this perturbed system may be described as follows [104]

$$dN(t) = N(t)\Big[\big(a(t) - b(t)N(t)\big)dt + \sigma(t)dW(t)\Big], \ t \geq 0. \tag{2.68}$$

In population dynamics, negative population growth will occur if a greater percentage of the population dies than can be replaced (population decline phase) [105]. This decline is influenced by the negative growth rate $a < 0$, which is further moderated by the logistic term $b$, showing how the population stabilizes at a lower density as time progresses.

Figure 2.7 presents a graphical representation of population dynamics under a negative growth rate scenario. The initial population $N_0$ is set to 1000 individuals, the growth rate is $a = -0.05$ per year, and $b = 0.0001$ per individual per year. The model is analyzed over a period of 100 years to clearly observe the population's approach towards zero.

# Chapter 3

# Nonlinear State Estimation and its Application in Energy Harvesters

## 3.1 Introduction

State estimation involves mathematical methods used to reconstruct the states of a system using measurements. The key challenge in state estimation is to offer robust real-time estimates despite measurement noise. Throughout this chapter, we will dive into the mathematical formulations and principles of the state estimation problem for a class of systems with linear dynamics and noisy quadratic measurements. Subsequently, we propose our innovative solution to this problem, the nonlinear estimator, and present the observability conditions and the rigorous proof of the stability of the estimation error. The proposed nonlinear estimator is then applied to the kinetic energy harvesting estimation problem.

## 3.2 Problem Statement

A particular class of systems with linear dynamics and quadratic measurements perturbed by noise is considered in this thesis. By focusing on this class, the goal is to derive observability conditions and design a nonlinear estimator to estimate the state.

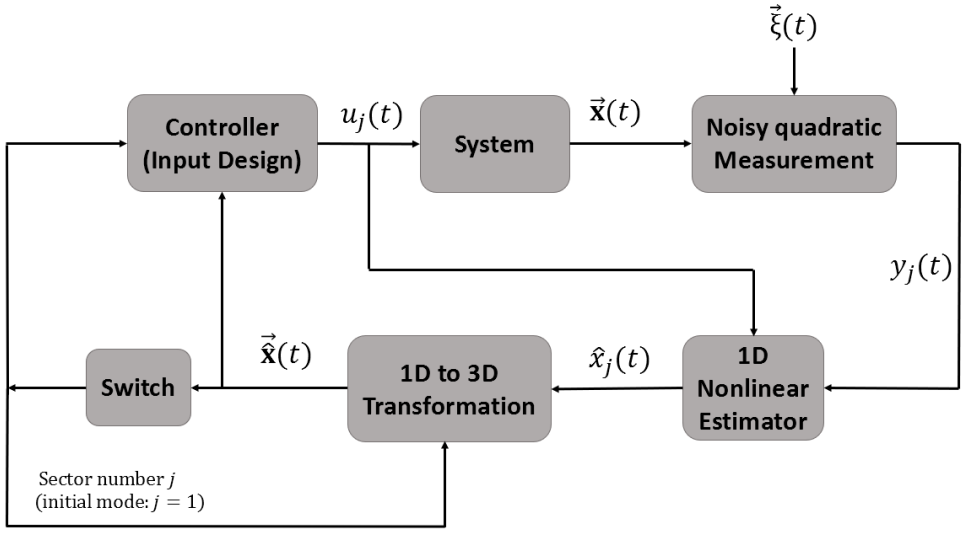


Figure 3.1: Block diagram of the nonlinear estimation and control framework

It is assumed that the state of the system has a piecewise affine trajectory in 3D. Our proposed method uses a 1D nonlinear estimator in each sector of the trajectory and a switching algorithm to switch between sectors. This system can be viewed as a hybrid system, since it exhibits continuous dynamics and discrete event switching. The block diagram in Figure 3.1 demonstrates our proposed method's estimation and control framework. The model of the system in each sector can be described as

$$\begin{aligned} \dot{x}(t) &= \alpha u(t) \\ y(t) &= \beta \frac{x^2(t)}{2} + \xi(t), \end{aligned} \tag{3.1}$$

where $x(t)$ is the state, $u(t)$ is the input of the system, the output $y(t)$ is the quadratic measurement, and $\xi(t)$ is zero-mean white noise with variance $\sigma^2$.

**Problem formulation:** Given the model (3.1), design a trajectory for $u(t)$ that makes the state $x(t)$ observable and propose an estimator for $\hat{x}(t)$ that guarantees that $\mathbb{E}[\delta x(t)] \to 0$ as $t \to \infty$, where $\delta x(t) = x(t) - \hat{x}(t)$.

## 3.3 Noiseless Problem

### 3.3.1 Observability

For nonlinear systems, local observability is often evaluated using a test that linearizes the system. However, a significant complexity with such systems is that their observability can vary based on the input. Therefore, aiming at global observability we must consider inputs that distinguish the states.

We consider first the case where there is no noise,

$$\begin{aligned} \dot{x}(t) &= u(t) \\ y(t) &= \frac{x^2(t)}{2}. \end{aligned} \tag{3.2}$$

The problem is to estimate the state $x(t)$ from the measurement $y(t)$. It is clear that this problem does not have a unique solution if the input of the system is equal to zero, because of the fact that both $x(t)$ and $-x(t)$ would lead to the same value of $y(t)$. We therefore, assume that the input $u(t)$ is determined by the designer and that there exist $t_1,\ t_2$, such that $u(t) \neq 0$ for $t \in [t_1, t_2]$ with $t_1 \geq 0,\ t_2 > t_1$. Under this assumption, one can write an augmented linear model ([59], [64]) of model (3.2) as

$$\begin{aligned} \begin{bmatrix} \dot{x}(t) \\ \dot{y}(t) \end{bmatrix} &= \begin{bmatrix} 0 & 0 \\ u(t) & 0 \end{bmatrix} \begin{bmatrix} x(t) \\ y(t) \end{bmatrix} + \begin{bmatrix} 1 \\ 0 \end{bmatrix} u(t) \\ y(t) &= \begin{bmatrix} 0 & 1 \end{bmatrix} \begin{bmatrix} x(t) \\ y(t) \end{bmatrix} \end{aligned} \tag{3.3}$$

**Theorem 3.1.** *The linear time-varying system in* (3.3) *is uniformly observable assuming the input* $u(t) = u_0 t^\alpha$ *with* $u_0 > 0$ *and integer* $\alpha \geq 0$ *where* $u(t) \neq 0$ *for* $t \in [t_1, t_2]$ *with* $t_1 \geq 0,\ t_2 > t_1$.

*Proof.* According to Theorem 2.9 provided in Chapter 2, for the instantaneous observability

of the LTV system (3.3) we have

$$\begin{aligned}
&\mathcal{O}_0(t) = C(t) = \begin{bmatrix} 0 & 1 \end{bmatrix}, \\
&\mathcal{O}_1(t) = \mathcal{O}_0(t)A(t) + \dot{\mathcal{O}}_0(t) = \begin{bmatrix} 0 & 1 \end{bmatrix} \begin{bmatrix} 0 & 0 \\ u(t) & 0 \end{bmatrix} = \begin{bmatrix} u(t) & 0 \end{bmatrix}, \\
&\mathcal{O}(t) = \begin{bmatrix} 0 & 1 \\ u(t) & 0 \end{bmatrix}.
\end{aligned} \tag{3.4}$$

When $u(t) \neq 0$ for $t \in [t_1, t_2]$ with $t_1 \geq 0,\ t_2 > t_1$, rank of $\mathcal{O}(t)$ is equal to 2. Therefore, the system has instantaneous observability. For uniform observability using the assumption $u(t) = u_0 t^\alpha$ with $u_0 > 0$ and integer $\alpha \geq 0$, one can write

$$\int_0^T \big|\det(\mathcal{O}(t))\big| dt = \int_0^T u_0 t^\alpha ds = \frac{u_0 T^{\alpha+1}}{\alpha+1} \geq \bar{\delta} > 0. \tag{3.5}$$

Since there exists a $\bar{\delta} = \frac{u_0 T^{\alpha+1}}{\alpha+1}$ and $T > 0$ satisfying the inequality (3.5) and based on Theorem 2.9 and Proposition 2.1 (Chapter 2), the system (3.3) is uniformly observable given the assumed input. □

Theorem 3.1 implies that if the designer picks such input the problem of estimating $x(t)$ from knowledge of $y(t)$ is guaranteed to have a solution. In the case of the constant input $u(t) = u$, the system becomes an LTI system with the following constant observability matrix

$$\mathcal{O} = \begin{bmatrix} C \\ CA \end{bmatrix} = \begin{bmatrix} 0 & 1 \\ u & 0 \end{bmatrix}, \quad |\mathcal{O}| = -u. \tag{3.6}$$

Since the determinant is not zero when the system's input $u$ is not zero, then the state $x(t)$ can be estimated from the measurement of $y(t)$. The literature has focused on the solution of this estimation problem using the transformation to the linear model (3.3), and then designing a Luenberger linear observer or a Kalman filter for time-varying linear systems.

### 3.3.2 Nonlinear Observer

This thesis will depart from previous approaches by proposing a nonlinear estimator for noisy measurements. The second author of [106] solved the noiseless problem as follows.
Consider an observer proposed in [107] to find an estimate $\hat{x}(t)$ of the state with dynamics

$$\dot{\hat{x}}(t) = u(t) + L\left(\frac{x^2(t)}{2} - \frac{\hat{x}^2(t)}{2}\right) = u(t) + \frac{L}{2}(x(t) + \hat{x}(t))(x(t) - \hat{x}(t)), \tag{3.7}$$

where $L$ is a gain to be determined by the designer. Writing the dynamics of the estimation error $\delta x(t) = x(t) - \hat{x}(t)$ yields

$$\delta\dot{x}(t) = \dot{x}(t) - \dot{\hat{x}}(t) = -\frac{L}{2}(x(t) + \hat{x}(t))(x(t) - \hat{x}(t)) = -\frac{L}{2}(2x(t) - \delta x(t))\delta x(t), \tag{3.8}$$

which is a Verhulst equation with a growth rate proportional to $-L$. To solve this Verhulst equation, article [106] follows the standard procedure and performs the change of variables

$$\delta x(t) = \frac{\dot{f}(t)}{1 - \frac{L}{2}f(t)}, \tag{3.9}$$

which is well defined for all values of $f(t)$ that are different from $2/L$. This condition will be later guaranteed when stating the main result in the theorem. Under the change of coordinates (3.9) equation (3.8) is transformed to

$$\ddot{f}(t) + Lx(t)\dot{f}(t) = 0, \tag{3.10}$$

which is linear and has the solution

$$f(t) = f(0)e^{-\int_0^t Lx(\tau)d\tau}. \tag{3.11}$$

Replacing (3.11) into the change of coordinates (3.9) then yields the error solution

$$\delta x(t) = \frac{\delta x_0 e^{-\int_0^t Lx(\tau)d\tau}}{1 - \frac{L}{2}\delta x_0 \int_0^t e^{-\int_0^s Lx(\tau)d\tau} ds}, \tag{3.12}$$

where, for a constant $u$ the integral in the denominator is

$$\int_0^t e^{-L\left(x_0 s + 0.5us^2\right)} ds = \sqrt{\frac{\pi}{2Lu}} e^{\frac{Lx_0^2}{2u}} \left[ er\left(\sqrt{\frac{L}{2u}} x_0 + \sqrt{\frac{Lu}{2}} t\right) - er\left(\sqrt{\frac{L}{2u}} x_0\right)\right],$$

and the $er$ function is defined as usual by

$$er(z) = \frac{2}{\sqrt{\pi}} \int_0^z e^{-\tau^2} d\tau. \tag{3.13}$$

The equilibrium points of equation (3.8) are obtained from the condition $\delta\dot{x}(t) = 0$, leading to the solution

$$\delta x(t) = 0, \ \forall t \geq 0, \tag{3.14}$$

and the (potential) solution

$$\delta x(t) = 2x(t), \ \forall t \geq 0. \tag{3.15}$$

Note, however, that (3.15) only represents an equilibrium point if $x(t)$ is constant, because otherwise equation (3.15) would lead to $\delta\dot{x}(t) = 2\dot{x}(t) \neq 0$. Given the assumption that $u \neq 0$ for $t \in [t_1, t_2]$ with $t_1 \geq 0, \ t_2 > t_1$, it is not possible that $x(t)$ will be constant for all time ($\dot{x} = u$) and therefore the equation (3.15) does not represent any equilibrium point. This leaves $\delta x(t) = 0, \ \forall t \geq 0$, as the only equilibrium point.

**Theorem 3.2.** *[107, 106] Let $|x_0| \leq \bar{x}_0$. If $L > 0, \hat{x}_0 \geq \bar{x}_0, u(t) = u_0 t^\alpha$ with $u_0 > 0$ and integer $\alpha \geq 0$, then $\delta x(t) \to 0$ as $t \to \infty$.*

*Proof.* [107, 106] The solution (3.12) converges to zero if $L > 0, \delta x_0 \leq 0$ and if $\int_0^t x(\tau)d\tau$ converges to infinity, which is the case when $u(t) = u_0 t^\alpha$ with $u_0 > 0$ and integer $\alpha \geq 0$. □

## 3.4 Noise-Corrupted Model: Nonlinear Estimator

The system model (3.1), (using equation (2.30) explained in Chapter 2), can be written as follows

$$\begin{aligned} dx(t) &= u(t)dt \\ z(t) &= y(t)dt = \frac{x^2(t)}{2}dt + dW(t). \end{aligned} \tag{3.16}$$

where $dW(t) = \xi(t)dt$ represents infinitesimal displacements of Brownian motion (or Wiener process) with $\mathbb{E}[dW(t)] = 0, \mathbb{E}[dW(t)^2] = \sigma^2 dt$, and $\sigma$ is the standard deviation of the noise. The following nonlinear estimator is proposed to estimate the state using noisy measurements.

$$\begin{aligned} d\hat{x}(t) =& u(t)dt + L\left(z(t) - \hat{z}(t)\right)dt \\ &= u(t)dt + L\left(\frac{x^2(t)}{2}dt + dW(t) - \frac{\hat{x}^2(t)}{2}dt\right) \\ &= u(t)dt + \frac{L}{2}(x(t) + \hat{x}(t))(x(t) - \hat{x}(t))dt + LdW(t). \end{aligned} \tag{3.17}$$

One can obtain the estimation error dynamics for the system with additive noise (3.16) as

$$\begin{aligned} d\delta x(t) &= dx(t) - d\hat{x}(t) \\ &= u(t)dt - u(t)dt - LdW(t) \\ &- \frac{L}{2}\delta x(t)\big(2x(t) - \delta x(t)\big)dt \\ &= -\frac{L}{2}\delta x(t)\big(2x(t) - \delta x(t)\big)dt - LdW(t) \end{aligned} \tag{3.18}$$

where, as before, $\hat{x}(t)$ is the estimated state, $\delta x(t) = x(t) - \hat{x}(t)$ is the estimation error, and $L$ is the estimator gain. Thus, the error $\delta x(t)$ is a stochastic process, and the error dynamics is modeled by the SDE (3.18).

**Theorem 3.3.** *If the trajectory $x(t)$ is such that*

$$|\lim_{t\to\infty} x(t)| = |x_\infty| \gg \frac{|\delta x_\infty|}{3}, \tag{3.19}$$

*where $\delta x_\infty$ is the stationary value of the estimation error $\delta x(t)$, then there is a stationary probability density $p(\delta x_{j_\infty})$ with a local maximum for $\delta x_{j_\infty} = 0$. This distribution can be approximated by the Gaussian probability density*

$$p(\delta x_{j_\infty}) = \frac{1}{\sqrt{2\pi\sigma_\infty^2}} e^{-\frac{\delta x_{j_\infty}^2}{2\sigma_\infty^2}}, \tag{3.20}$$

*where*

$$\sigma_\infty^2 = \frac{L\sigma^2}{2x_\infty}. \tag{3.21}$$

*Moreover, if $L$ is chosen such that*

$$L \ll \frac{2x_\infty}{\sigma^2} \tag{3.22}$$

*then $\sigma_\infty \ll 1$, and the stationary probability density is concentrated close to its mean.*

*Proof.* The Fokker-Planck equation is

$$\begin{aligned}\frac{\partial p(t,\delta x(t))}{\partial t} =& -\frac{\partial}{\partial \delta x(t)}\Big[F\big(t,\delta x(t)\big)p\big(t,\delta x(t)\big)\Big] \\ &+ \frac{1}{2}\frac{\partial^2}{\partial \delta x^2(t)}\Big[D\big(t,\delta x(t)\big)p\big(t,\delta x(t)\big)\Big]\end{aligned} \tag{3.23}$$

where $p(t,\delta x(t))$ is the probability density function of the error, $F(t,\delta x(t))$ is the drift coefficient, and $D(t,\delta x(t))$ is the diffusion coefficient. From equation (3.18) we have

$$F\big(t,\delta x(t)\big) = -\frac{L}{2}\delta x(t)\big(2x(t) - \delta x(t)\big) \tag{3.24}$$

and

$$D\big(t,\delta x(t)\big) = L^2\sigma^2. \tag{3.25}$$

Replacing $F$ and $D$ in (3.23) and setting $\frac{\partial P(t,\delta x(t))}{\partial t} = 0$ to find a stationary distribution yields

$$p''(\delta x_\infty) + a(\delta x_\infty)p'(\delta x_\infty) + a'(\delta x_\infty)p(\delta x_\infty) = 0, \tag{3.26}$$

where

$$a(\delta x_\infty) = \left(\frac{2x_\infty \delta x_\infty}{L\sigma^2} - \frac{\delta x_\infty^2}{L\sigma^2}\right), \tag{3.27}$$

and the prime symbol denotes the total derivative with respect to $\delta x$. Note that the last two terms of equation (3.26) form the expression for the derivative of a product. Therefore, equation (3.26) can be integrated to yield

$$p'(\delta x_\infty) + a(\delta x_\infty)p(\delta x_\infty) = c, \tag{3.28}$$

where $c$ is a constant of integration. The constant $c$ must be zero for a local maximum at $\delta x_\infty = 0$, and the solution of (3.28) is then

$$p(\delta x_\infty) = p_0 e^{-\frac{\delta x_\infty^2}{2\sigma_\infty^2}\left(1-\frac{\delta x_\infty}{3x_\infty}\right)}, \tag{3.29}$$

where $\sigma_\infty^2$ is given by expression (3.21). The result then follows from assumption (3.19). □

## 3.5 State Estimation using Energy Measurement with Application in Energy Harvesters

In pursuit of advancing technology and addressing the growing demand for mobile power sources, scientists and engineers have been exploring innovative solutions to extend the operational lifespan of portable electronic devices. This quest has led to a remarkable breakthrough in the form of harvesting energy from the human body itself.

In energy harvesters, apart from harnessing the kinetic energy stored within our bodies, we can utilize the generated electrical energy measurements to gain insights into the system's

mechanics and physical state. Solving this state estimation problem leads to obtaining the real-time system's state which can be used in system diagnosis, boosting performance, and optimizing the decision-making.

The kinetic energy of a moving body is proportional to the square of its velocity. This is mathematically denoted by $K_E = \frac{1}{2}mv_b^2$, where $m$ is the body's mass and $v_b$ is its velocity. The generated electrical energy on the other hand can be measured using voltage measurements [108] or methods such as Monjolo (a power-proportional, energy-harvesting approach to energy-metering with the energy-harvesting power supply as the sensor [109]). The electrical power or energy $E_e$ in the output is proportional by the efficiency coefficient $\eta_{COH}$ to the kinetic energy $K_E$ in the input. The harvester's efficiency commonly quantified as Cost of Harvesting (COH) [110], can be used to obtain the kinetic energy ($K_E \approx \frac{1}{\eta_{COH}}E_e$). Consequently, it is possible to model the problem of estimating the moving body's velocity using noisy energy measurements. Given the force $F(t) = m\dot{v}_b(t)$ as the input, the following models this system as

$$\begin{aligned} \dot{v}_b(t) &= \frac{F(t)}{m} = \alpha u(t) \\ y(t) &= E_e + \xi(t) = \frac{1}{2}\eta_{COH} m v_b^2(t) + \xi(t), \end{aligned} \tag{3.30}$$

where considering the body velocity to be the state $x(t) = v_b(t)$, this system is the same as the main nonlinear system (3.1), and one can use the nonlinear estimator to estimate the body velocity using the electrical energy measurement.

## 3.6 Simulation Results

In this section, simulation results will illustrate the effectiveness of the proposed nonlinear estimator for the kinetic energy harvester using the noisy energy measurement. The system in equation (3.30) is simulated with different inputs such as

- constant input

$$\dot{x}(t) = u(t) = u_0 \neq 0 \tag{3.31}$$

- ramp input

$$\begin{aligned} &\dot{x}(t) = u(t) = u_0 t \\ &u_0 \neq 0 \end{aligned} \tag{3.32}$$

- feedback input

$$\begin{aligned} &\dot{x}(t) = u(t) = -\alpha\hat{x}(t) + \beta \\ &\hat{x}(0) \neq \frac{\beta}{\alpha},\ \alpha \neq 0 \end{aligned} \tag{3.33}$$

The measurement of the energy in this system is perturbed by Gaussian white noise with zero-mean and variance equal to $0.1 Joules$. A nonlinear estimator (3.17) is designed for the system (3.30). Moreover, a Kalman filter (3.34) is also designed for the augmented system (3.3) to compare our proposed method to the established methods in the literature.
Since the system (3.30) is observable, and based on Theorem 2.11, one can design a Kalman-Bucy filter (or even a Luenberger observer) for this system as follows

$$\begin{bmatrix} \dot{\hat{x}}(t) \\ \dot{\hat{y}}(t) \end{bmatrix} = \begin{bmatrix} 0 & 0 \\ u(t) & 0 \end{bmatrix} \begin{bmatrix} \hat{x}(t) \\ \hat{y}(t) \end{bmatrix} + \begin{bmatrix} 1 \\ 0 \end{bmatrix} u(t) + \begin{bmatrix} K_1 \\ K_2 \end{bmatrix} (y(t) - \hat{y}(t)). \tag{3.34}$$

where $K_1$ and $K_2$ are the estimator gains.

One can write the error dynamics of this estimator as follows

$$\begin{aligned}\dot{e}_L &= \begin{bmatrix}\dot{x}(t)\\ \dot{y}(t)\end{bmatrix} - \begin{bmatrix}\dot{\hat{x}}(t)\\ \dot{\hat{y}}(t)\end{bmatrix} \\ &= \begin{bmatrix}0 & -K_1\\ u(t) & -K_2\end{bmatrix} e_L.\end{aligned} \tag{3.35}$$

The closed-loop eigenvalues of the error dynamics can be found by solving the following quadratic equation

$$\lambda^2 + K_2\lambda + K_1 u(t) = 0 \tag{3.36}$$

It is straightforward to show that assuming $u(t) > 0$, the eigenvalues are in the left-half plane and the error is asymptotically stable when $K_1 > 0$ and $K_2 > 0$. Moreover, the Kalman gains $K_1$ and $K_2$ can be found by solving the Ricatti equation (2.57) (please refer to Example 2.4).

### 3.6.1 Constant Input

#### 3.6.1.1 Nonlinear Estimator, Constant Input

Figure 3.2 shows the estimation error for a constant input ($u(t) = 1$). In this figure, 10 error trajectories or sample paths with different noise seeds are shown, all with the initial condition $x(0) = 0$ and initial estimation $\hat{x}(0) = 10\, m/s$.

Figure 3.3 illustrates the average of the estimation error's different sample paths with different estimator gains to see the effect of increasing $L$. Increasing $L$ decreases the convergence time; however, the steady-state variance of the estimation error $\sigma_\infty^2$ increases proportionally to $L$ which follows equation (3.21) in Theorem 3.3. Therefore, there is a trade-off between faster convergence and precision of the steady-state estimation.

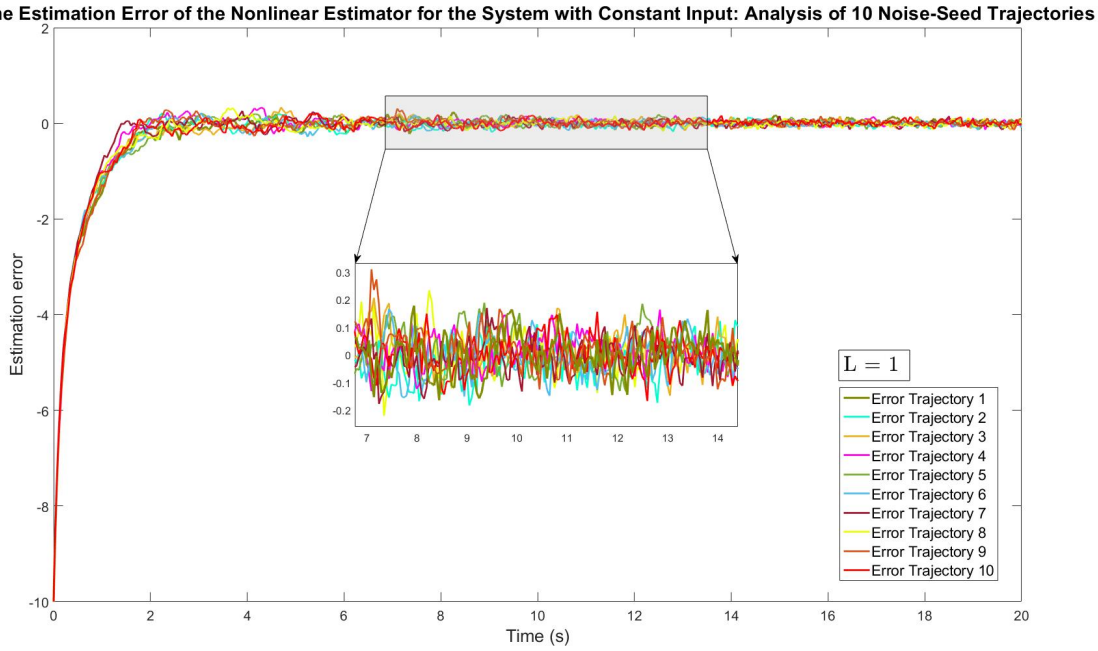


Figure 3.2: The estimation error's sample paths in the nonlinear estimator. (constant input)

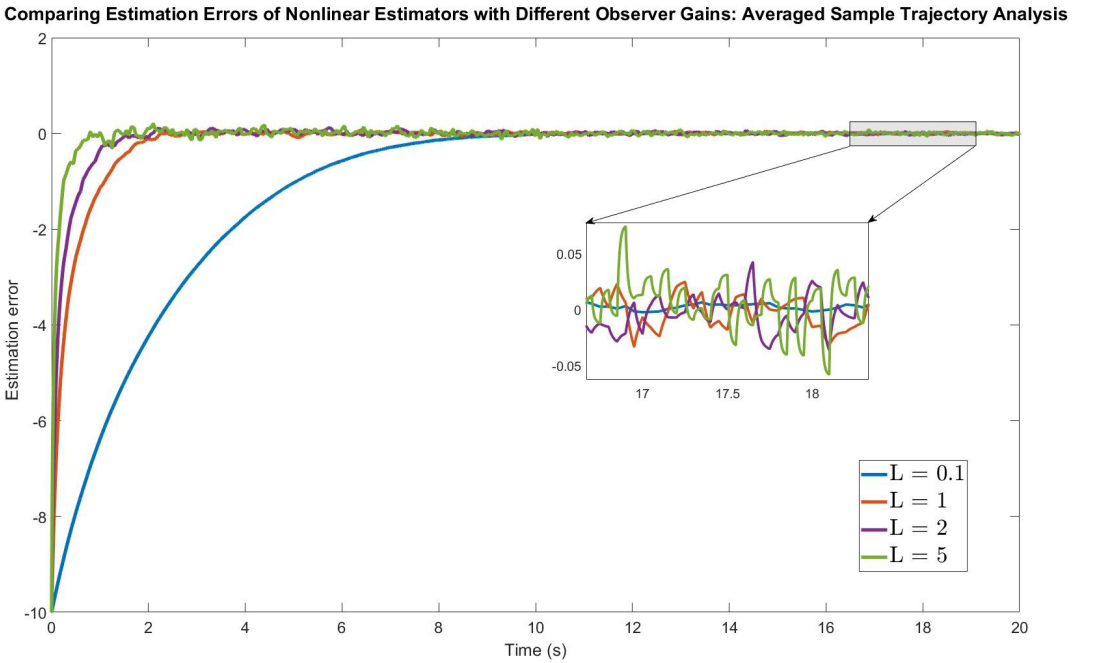


Figure 3.3: Averages of the estimation error's sample paths in the nonlinear estimator with different estimator gain $L$. (constant input)

### 3.6.1.2 Augmented State Method with Kalman Filter, Constant Input

Figure 3.4 depicts 10 estimation error trajectories (different noise seeds) of the Kalman filter for the augmented system with constant input ($u(t) = 1$), with the initial condition $x(0) = 0$ and initial estimation $\hat{x}(0) = 10\, m/s$, and the weighting matrices $Q = 0.1 \times \mathbf{I}_2, R = 0.1$.

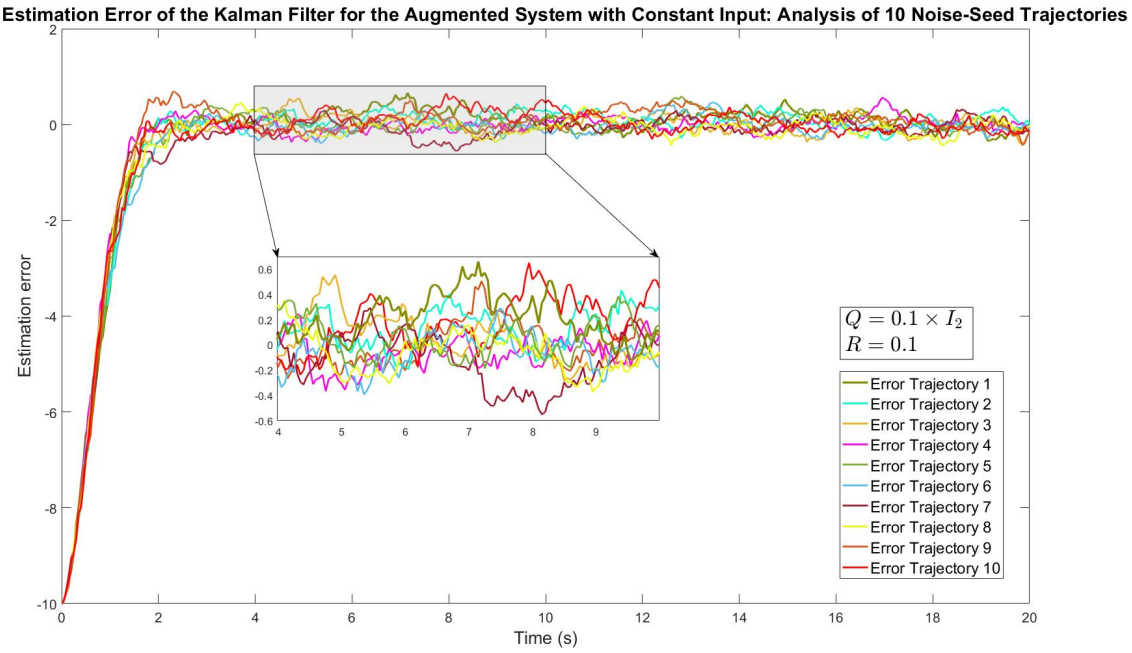


Figure 3.4: The estimation error's sample paths with the Kalman filter. (constant input)

Figure 3.5 shows the averages of estimation error's sample paths with different Kalman filter weighting matrices ($Q$ and $R$). In the case with noise covariances $Q = 0.1 \times \mathbf{I}_2, R = 0.1$, the mean error converges to zero, and its steady-state variance is lower compared to others.

### 3.6.1.3 Comparison, Constant Input

To compare the nonlinear estimator with the augmented state method with the Kalman filter, figure 3.6 illustrates the averaged trajectories of the estimation error for both methods with the best parameters I could find. The estimation error's mean is closer to zero (more accurate), and the variance in steady-state is smaller too (more precise) for the proposed nonlinear estimator.

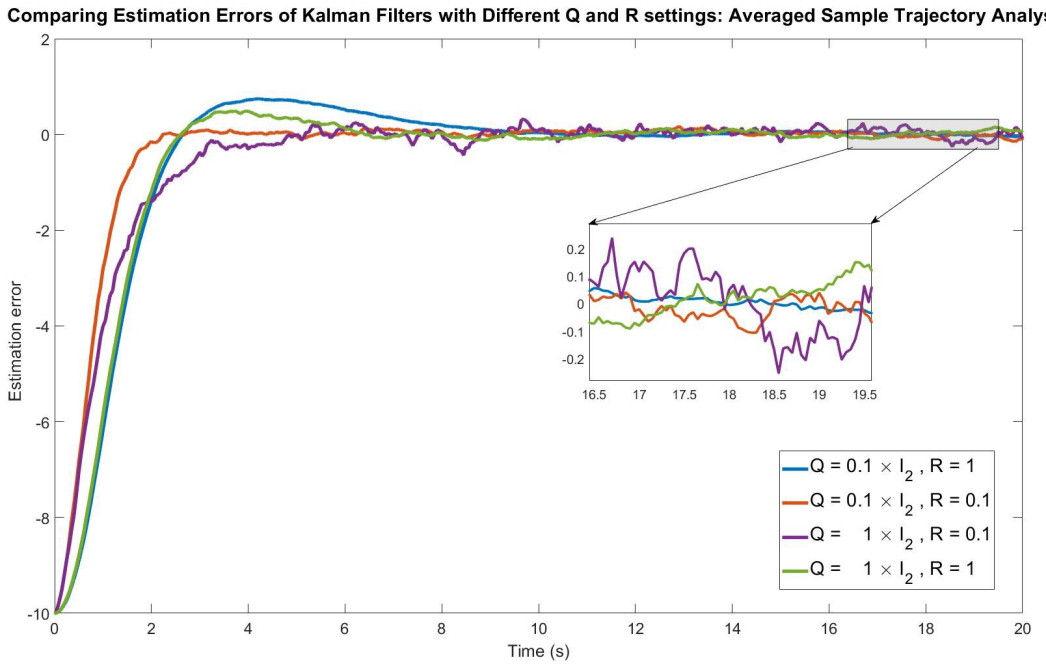


Figure 3.5: Averages of the estimation error (Kalman filter, ramp input)

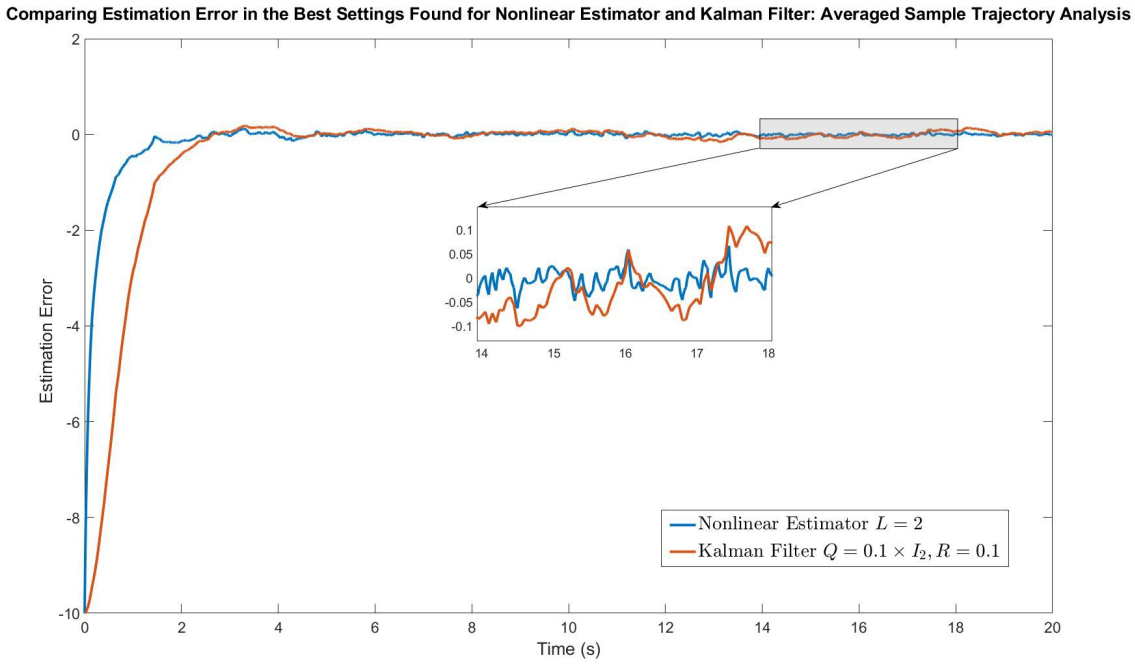


Figure 3.6: The estimation error of the nonlinear estimator and Kalman filter.

### 3.6.2 Ramp Input

#### 3.6.2.1 Nonlinear Estimator, Ramp Input

Figure 3.7 illustrates the estimation error sample paths of the nonlinear estimator with a bounded ramp input ($u(t) = t$ bounded between 0 to 10 seconds). The initial condition of the system is $x(0) = 0$ and initial estimation is $\hat{x}(0) = 10\, m/s$.

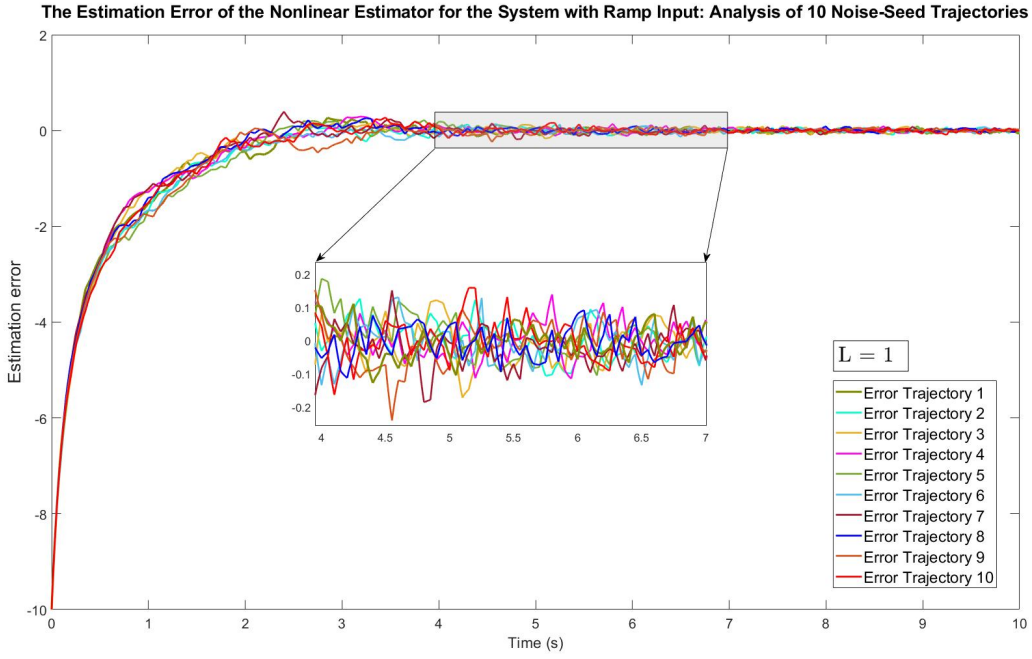


Figure 3.7: Estimation error sample paths (ramp input, $L = 1$).

#### 3.6.2.2 Augmented State Method with Kalman Filter, Ramp Input

Figure 3.8 shows the estimation error of the Kalman filter in the augmented system with bounded ramp input.

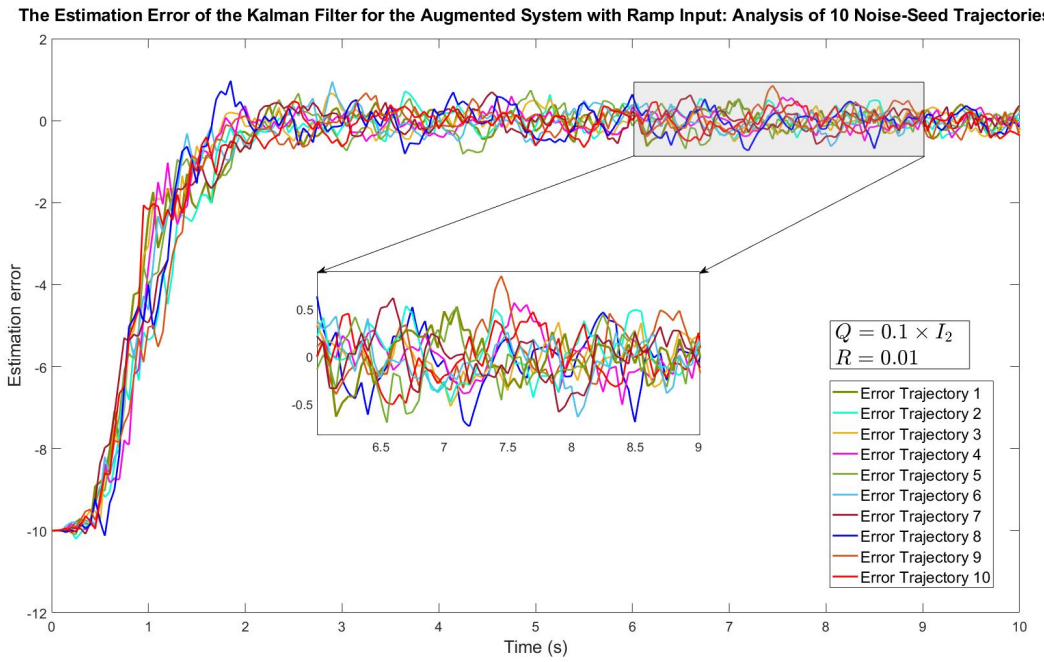


Figure 3.8: Error sample paths (Kalman filter, ramp, $Q = 0.1 \times \mathbf{I}_2, R = 0.01$).

#### 3.6.2.3 Comparison

Figures 3.9 and 3.10 show the averages of the estimation error's different sample paths with different observer gains ($L$) and Kalman filter noise covariances $Q$ and $R$. Figure 3.9 illustrates that increasing $L$ decreases the convergence time. However, following equation (3.21) in Theorem 3.3, the steady-state variance of the estimation error $\sigma_\infty^2$ increases proportionally to $L$.

Figure 3.11, illustrates the averaged trajectories of the estimation error for both methods with the best parameters the author could find.

Similar to the constant input case, the convergence time of the estimation error towards a region proximal to zero is less using the nonlinear estimator relative to the Kalman filter. Furthermore, the mean value of the estimation error is closer to zero, and the steady-state variance is notably reduced using the nonlinear estimator compared to the Kalman filter.

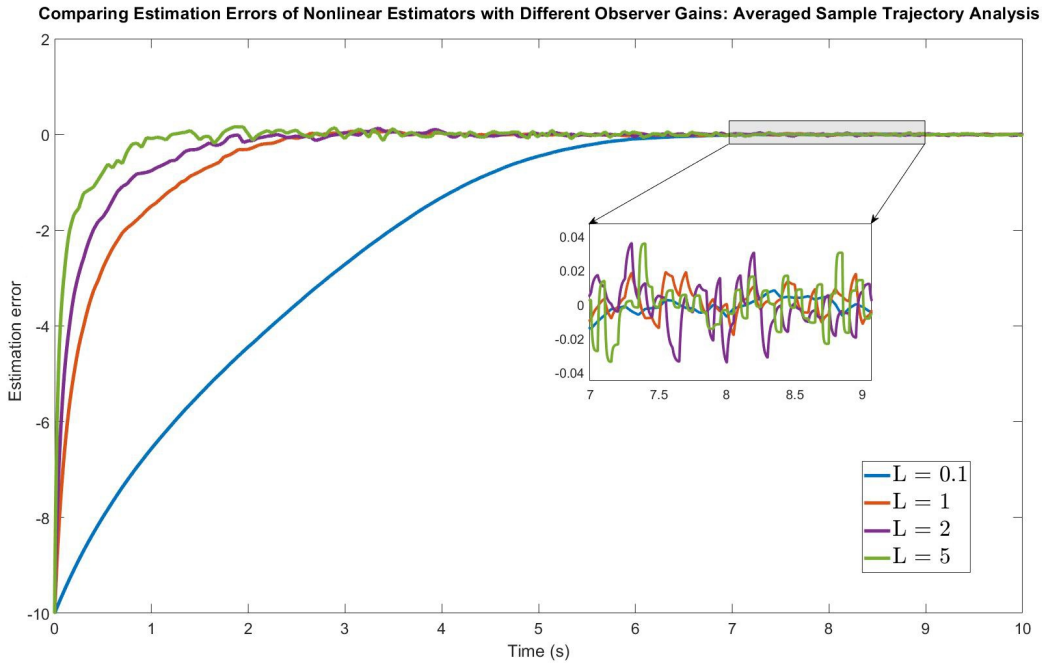


Figure 3.9: Averages of sample paths (ramp input).

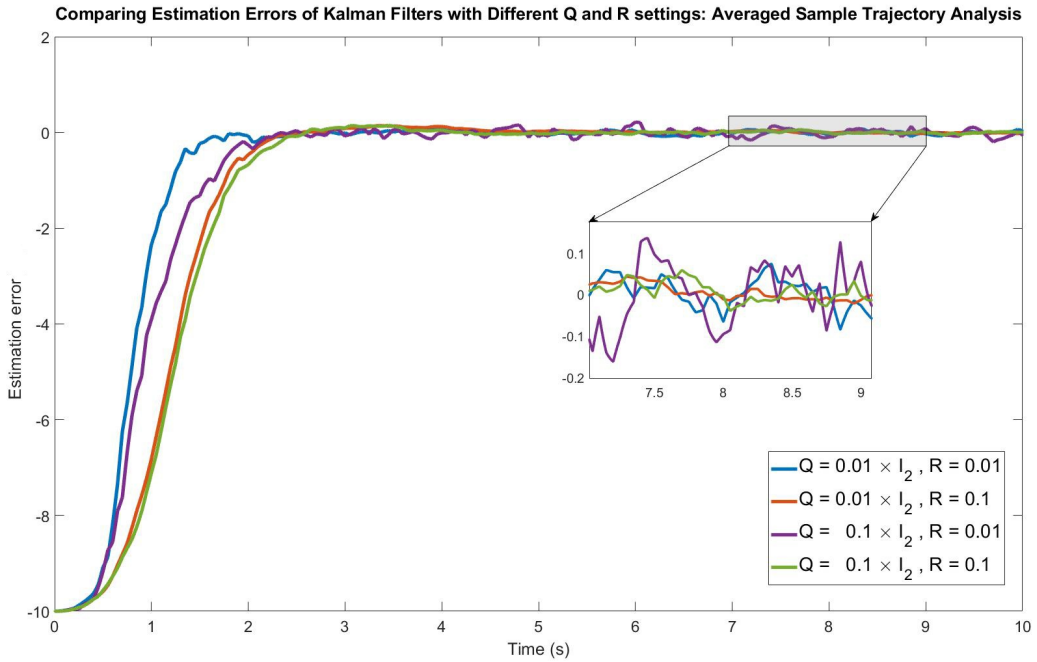


Figure 3.10: Averages of the estimation error (Kalman filter, ramp input).

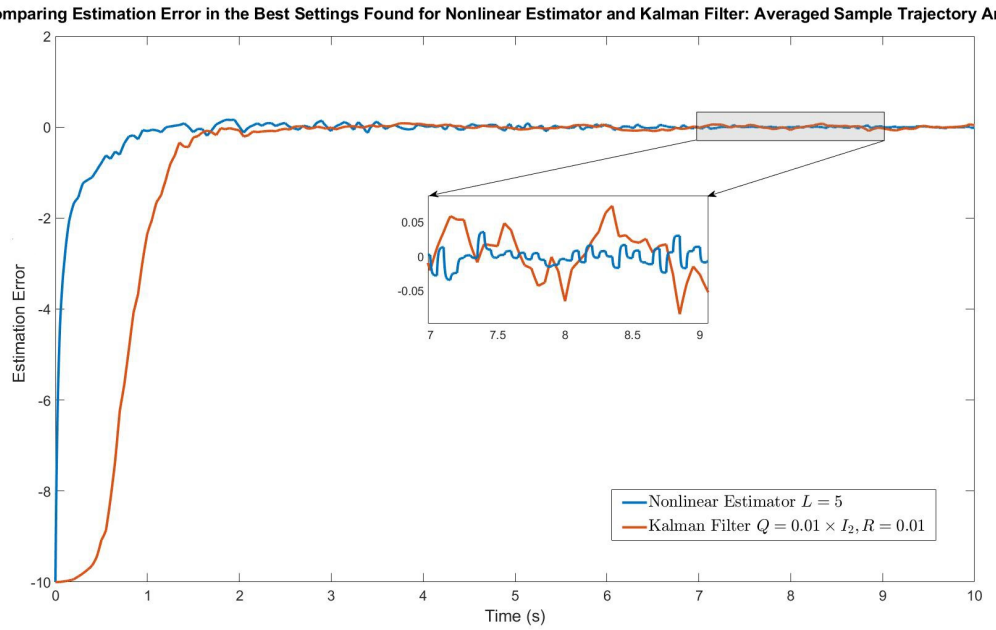


Figure 3.11: Estimation error of the nonlinear estimator and Kalman filter.

### 3.6.3 Feedback Input

In this section, the input of the system is designed as follows

$$\begin{aligned} u(t) &= -\alpha\hat{x}(t) + \beta \\ \hat{x}(0) &\neq \frac{\beta}{\alpha},\ \alpha \neq 0 \end{aligned} \tag{3.37}$$

where $u(t)$ is the input of the system, consisting of two constants $\alpha$ and $\beta$, and $\hat{x}(t)$ is the estimated state. The quadratic measurement of the system is perturbed by Gaussian white noise with zero-mean and variance equal to $0.1 Joules$, and the initial state is $x(0) = 0\, m/s$. A nonlinear estimator for this system and a Kalman filter for the augmented system is designed to estimate the state from the noisy measurement.

#### 3.6.3.1 Nonlinear Estimator, Feedback Input

Figure 3.12 shows the estimation error of the nonlinear estimator with $\alpha = 1$ and $\beta = 10$. In this figure, 10 error sample paths with different noise seeds have been shown, all with initial

estimations $\hat{x}(0) = 20\, m/s$ which satisfies the condition $\hat{x}(0) \neq \frac{\beta}{\alpha}$.

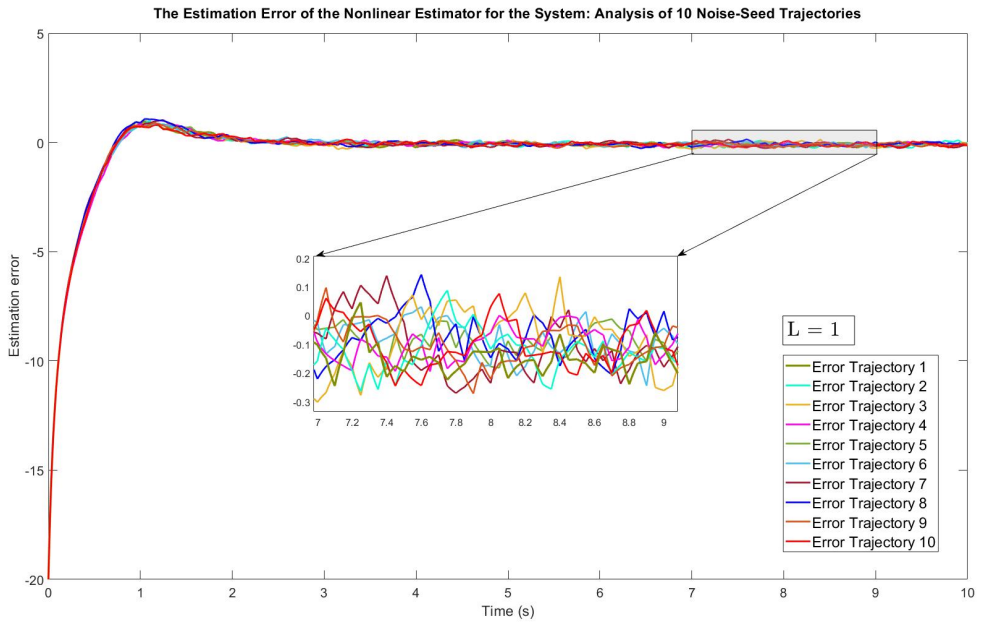


Figure 3.12: The estimation error's sample trajectories in the nonlinear estimator. ($\alpha = 1$, $\beta = 10$, $\hat{x}(0) = 20$)

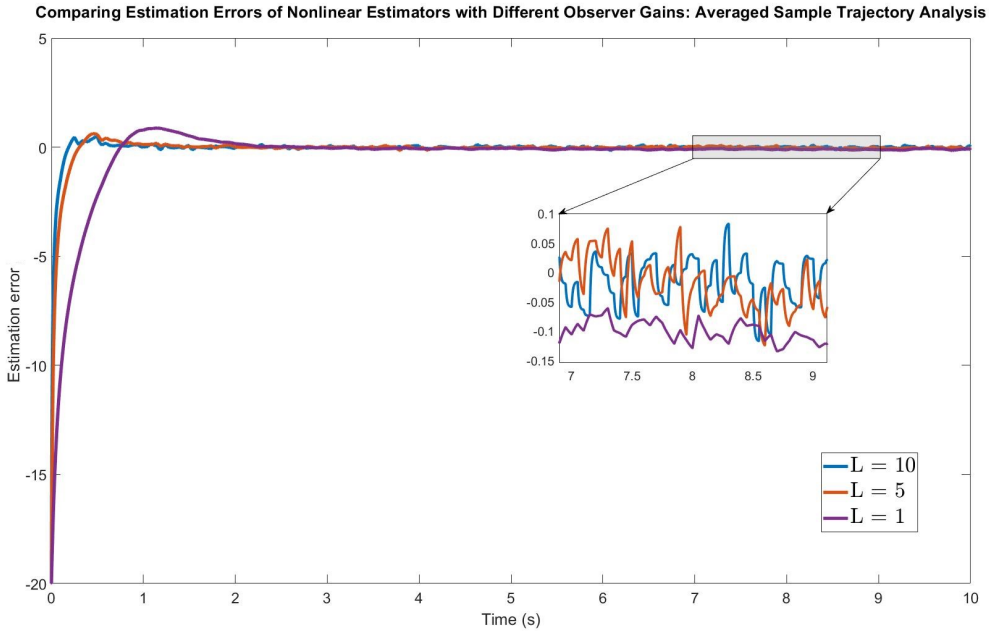


Figure 3.13: The averaged estimation error's sample paths in the nonlinear estimator with different $L$. ($\alpha = 1$, $\beta = 10$, $\hat{x}(0) = 20$)

Figure 3.13 represents a comparison between the averaged estimation errors with different estimator gains for $\alpha = 1$ and $\beta = 10$. Increasing $L$ leads to a faster convergence and estimation error's mean closer to zero, but higher error's variance in the steady-state as before.

#### 3.6.3.2 Augmented State Method with Kalman Filter, Feedback Input

Figure 3.14 shows the estimation error sample paths of the Kalman filter in the augmented system with $\alpha = 1$, $\beta = 10$, noise covariances $Q = 0.01 \times \mathbf{I}_2$, $R = 0.01$, and $\hat{x}(0) = 20$.

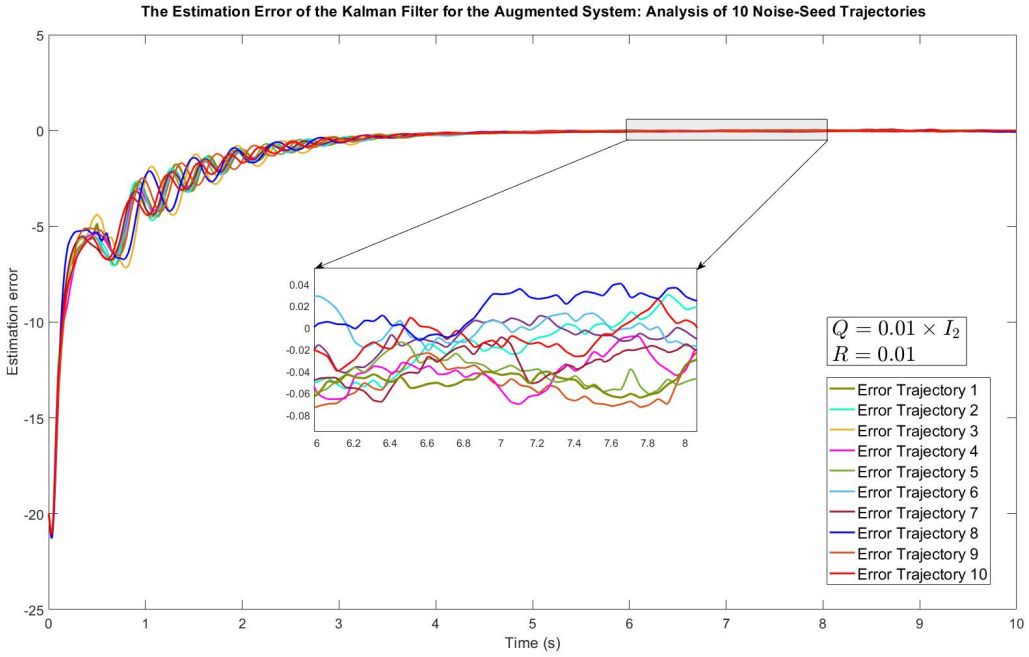


Figure 3.14: The estimation error's sample paths in the Kalman filter. ($\alpha = 1$, $\beta = 10$, $\hat{x}(0) = 20$)

Figure 3.15 shows the averaged estimation errors of the Kalman filter with different $Q$ and $R$ in the augmented system with $\alpha = 1$, $\beta = 10$ and $\hat{x}(0) = 20$.

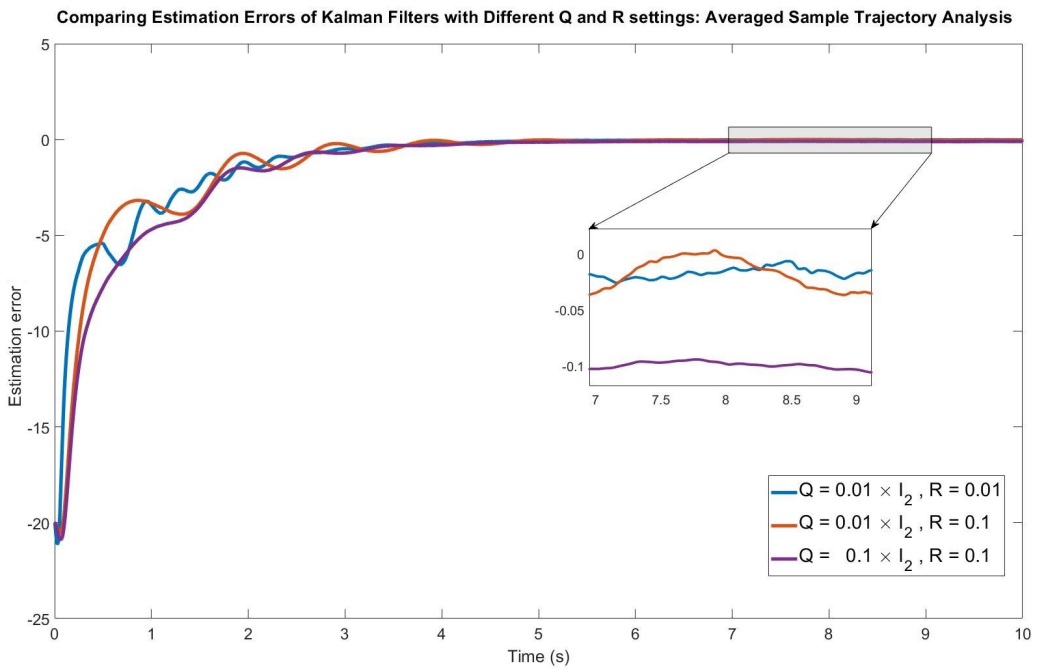


Figure 3.15: Averages of the estimation error (Kalman filter, feedback input).

#### 3.6.3.3 Comparison, Feedback Input

To compare the methods, Figures 3.16 and 3.17 illustrate the averaged trajectories of the estimation error for both methods with the best parameters found by the author. The initial estimated state is $\hat{x}(0) = 20$, $\alpha = 1$ and $\beta = 10$ for the simulation in Figure 3.16, and $\hat{x}(0) = 10$, $\alpha = 1$ and $\beta = 30$ respectively for the simulation in Figure 3.17.

The results indicate a faster convergence of the mean of the estimation error to zero in the case of the nonlinear estimator when compared to the Kalman filter. Furthermore, the estimation error using the nonlinear filter consistently maintains a state of equilibrium at zero after convergence. This denotes a stable accuracy in estimation following the initial convergence phase. However, despite the aforementioned advantages of the nonlinear estimator, the Kalman filter exhibits a lower estimation error variance in the steady-state in this case.

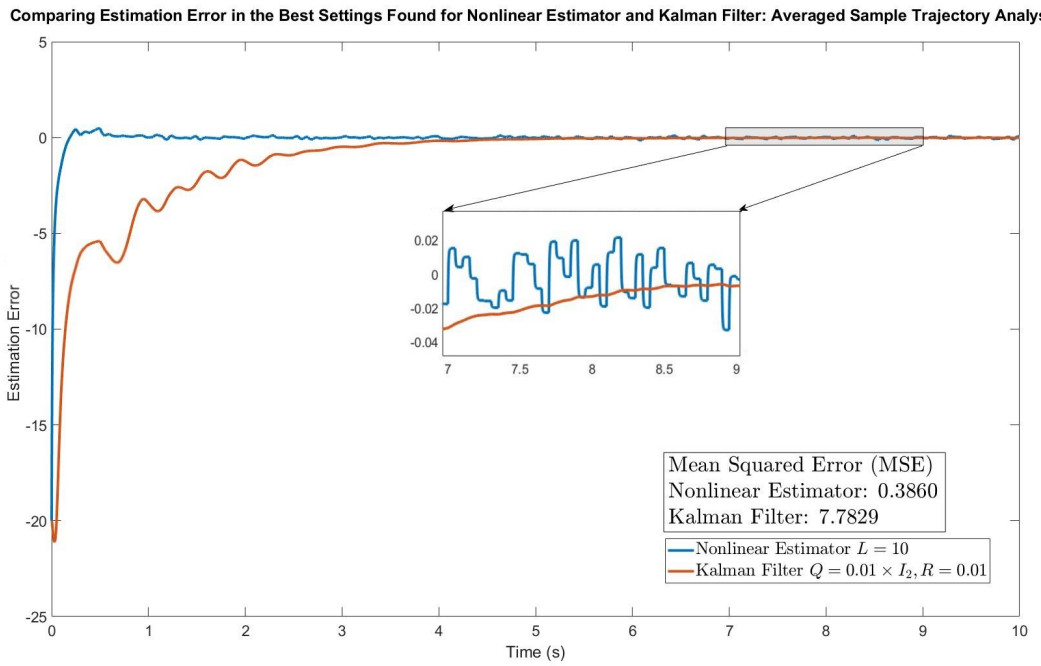


Figure 3.16: The estimation error of the nonlinear estimator and Kalman filter. ($\alpha = 1$, $\beta = 10$, $\hat{x}(0) = 20$)

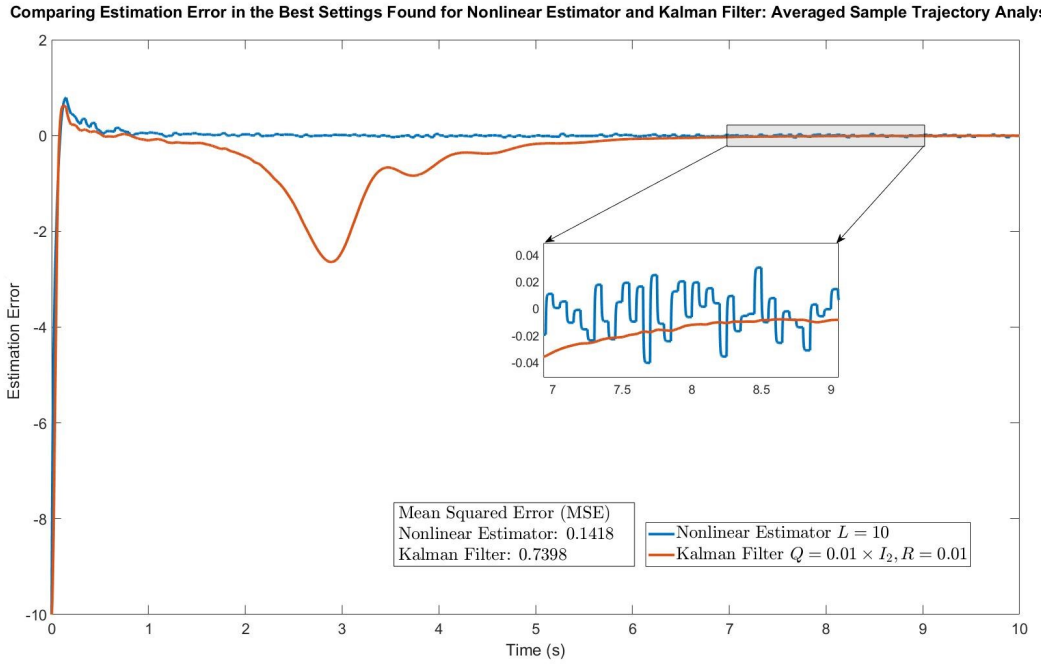


Figure 3.17: The estimation error of the nonlinear estimator and Kalman filter. ($\alpha = 1$, $\beta = 30$, $\hat{x}(0) = 10$)

### 3.6.3.4 State Variable, Feedback Input

Figures 3.18 and 3.19 illustrate the trajectories of the state (body velocity) with the input in (3.37) alongside the averaged trajectories of the estimated state using both methods. In these simulations $\alpha = 1$, $\beta = 30$, and the initial estimations are selected as $\hat{x}(0) = 10\, m/s$ and $\hat{x}(0) = 50\, m/s$ respectively.

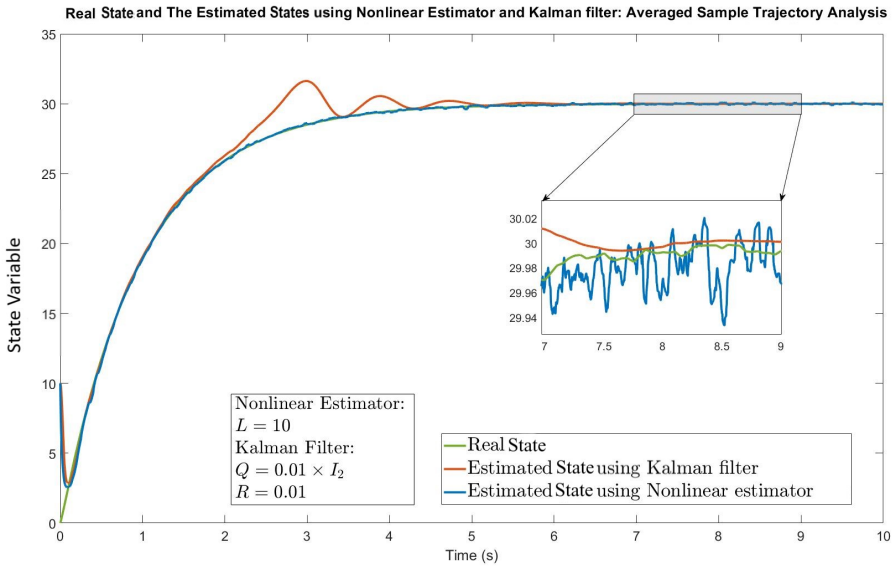


Figure 3.18: Averaged trajectories of the state and the estimated states. $(\hat{x}(0) = 10\, m/s)$

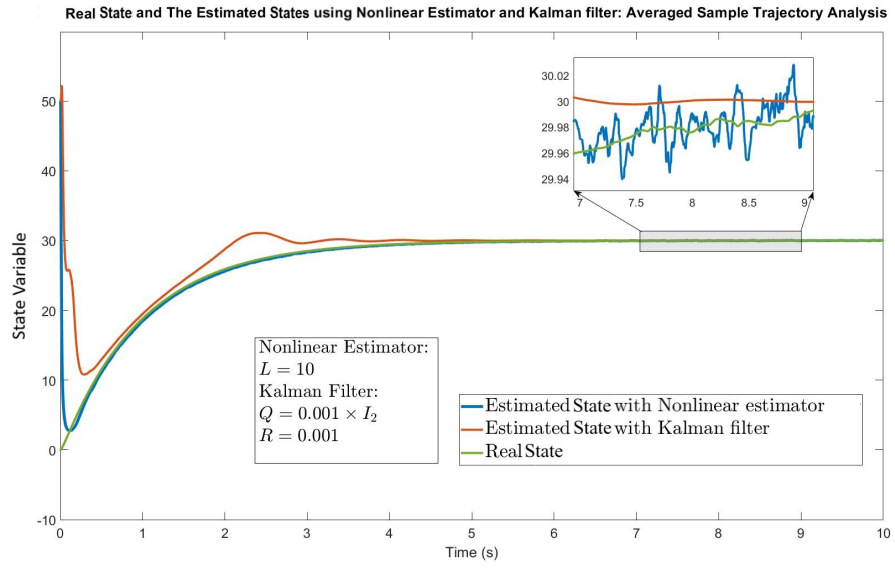


Figure 3.19: Averaged trajectories of the state and the estimated states. $(\hat{x}(0) = 50\, m/s)$

It can be inferred from Figures 3.18 and 3.19 that the state converges to the steady-state value $\beta/\alpha$. Moreover, the estimated state trajectory using the Kalman filter depends on the initial estimate. In the case of $|\hat{x}(0)| > |\beta|$, the estimation using the Kalman filter is worse than $|\hat{x}(0)| < |\beta|$.

### 3.6.4 Discussion of Simulation Results

From the simulations presented above, one can draw the following conclusions:

- The nonlinear estimation gain $L$ is proportional to the steady-state variance of the estimation error $\sigma_\infty^2$ and inversely proportional to the convergence time.
- The convergence time of the estimation error to zero is smaller using the nonlinear estimator relative to the Kalman filter. Furthermore, the estimation error's mean is closer to zero, and the steady-state variance is lower in the nonlinear estimator compared to the Kalman filter with the weighting matrices tested in this thesis.
- In the case of the feedback input and $|\beta| > |x(0)|$, the estimation error of the nonlinear estimator converges to a neighborhood of zero. However, it may deviate from zero for the Kalman filter at some times. (Figures 3.16, 3.17)
- The Mean Squared Error (MSE) of the nonlinear estimator is less than the Kalman filter using the parameters tested in this thesis for both methods.
- The nonlinear estimator is simpler to tune than the Kalman filter.

## 3.7 Conclusion

In this chapter, a method of state estimation is proposed for a class of systems with linear dynamics and squared measurements perturbed by zero-mean Gaussian noise. This proposed nonlinear estimator is used to estimate the body velocity in a kinetic energy harvester using the measurements of the generated electrical energy.

The error dynamics of the nonlinear estimator were described by a nonlinear Verhulst logistic equation. This observation unveiled a link between the state estimation using noisy squared measurements and population dynamics. The equation of time evolution of the estimation error PDF is derived. Then it has been proved that the stationary distribution of the estimation error will converge to a zero-mean Gaussian with adjustable variance under a certain assumption on the steady-state value of velocity (3.19).

The simulation results demonstrate the performance of the proposed nonlinear estimator in terms of convergence speed and steady-state error estimation mean (accuracy) and variance (precision), compared to the Kalman filter. The nonlinear estimator not only achieved faster convergence for all inputs but also maintained convergence, unlike the Kalman filter. Its mean squared error (MSE) was lower. Additionally, the nonlinear estimator proved to be simpler to tune, representing a significant practical advantage.

# Chapter 4

# Waypoint Navigation Based on Range Measurement with Application to Pipeline Inspection

## 4.1 Introduction

Regular inspections of pipelines are necessary to evaluate their condition, as they frequently exhibit problems such as corrosion or external damage. In particular, in the oil and gas sector, the damaged pipes might have serious consequences, such as explosions or environmental risks. Preventing financial losses and environmental contamination and maintaining safe working conditions all depend on the early diagnosis of these problems. Traditionally, pipeline inspection was a labor-intensive and potentially dangerous task. Furthermore, although manual pipeline inspection can be performed regularly, it is time consuming and unsafe in hazardous places [111]. To address these issues, employing UAVs with vision sensors offers a promising, cost-efficient, and reliable alternative for performing similar inspection tasks [112], [113]. These autonomous quadrotors reduce human interaction and, therefore, significantly decrease the possibility of human error and enhance the reliability of inspection

by providing high-quality and consistent data in dangerous and repetitive operations [114]. Nowadays, the majority of UAVs are capable of autonomous navigation using the Global Positioning System (GPS) and inertial sensors. Despite the high level of automation achieved, these GPS-based UAV navigation methods are highly dependent on GPS signals. Their reliance on GPS presents a challenge for GPS-denied environments where there is poor satellite coverage, multipath propagation, and deliberate jamming [115], [116]. One of the alternatives commonly used for UAV navigation in GPS-denied environments is range measurement sensors due to their lightweight, cost-effective, and low power consumption. Range typically derives from analyzing the time of flight of specific signal transmissions, which can be either acoustic or electromagnetic in nature. In pipeline inspection, UAVs are frequently employed to navigate extensive pipeline systems typically situated in GPS-denied environments, such as underground or within tunnels. Employing range measurement for UAV navigation in these scenarios not only addresses the challenge of GPS unavailability but also contributes to reduced power consumption. The reason is that range sensors use less power compared to other sensors for GPS-denied navigation [117]. This reduction in power usage enables UAVs to complete vast pipeline mapping tasks without the need for frequent recharging.

The application of pipeline monitoring necessitates that the unmanned aerial vehicle (UAV) navigates to predetermined specific geographic markers, or "waypoints," with efficiency and reliability. To achieve this goal with autonomous reliability, the deployment of a navigation system is crucial so that the UAV persistently maintains its spatial and temporal positioning within the environment [118]. These waypoints are at the turning points of the pipeline where range measurement emitters (sources) are installed. Within this context, the quadrotor depends on an accurate estimation based on range measurements to an emitter to maintain an accurate course, ensuring that it remains within safe proximity to the pipeline while covering the entirety of the structure.

The range measurements provide critical data that help the quadrotor navigate through waypoints, even in challenging or GPS-denied environments, effectively compensating for

any potential loss or interference of signals. Nevertheless, it is important to consider that range data alone does not provide directional information; hence, solely relying on range measurements does not specify the exact location of the quadrotor. Instead of a unique and specific point, a range sensor provides a wide spectrum of possible positions [119].

In addition, range measurements are subject to inaccuracies caused by environmental noise or malfunctioning equipment [120]. Noise in distance measurements increases the effects of incomplete data and adds to uncertainty [121]. Therefore, it is essential to implement an estimation algorithm that accurately determines the exact position of the quadrotor.

This chapter aims to present the estimation and control problem of a navigation system. The theoretical framework of the nonlinear estimator is elaborated upon and extended to piecewise affine motions. This expansion is illustrated in a practical case study focusing on the application of a nonlinear estimator. This case study is centered on position estimation within the navigation system of a quadrotor, specifically designed for pipeline inspection tasks in a waypoint scenario using noisy range measurements. Simulation results demonstrate the effectiveness and robustness of this approach in real-world scenarios.

## 4.2 Problem Formulation

### 4.2.1 Motion in 3D

Let $\vec{r}(t) \in \mathbb{R}^3$ be the position of a vehicle and let a range measurement emitter (source) be located at the position $\vec{s}$. Additionally, let

$$d(t) = \left\| \vec{r}(t) + \vec{\xi}(t) - \vec{s} \right\|$$

denote the measured range between the vehicle and the source, where $\|.\|$ denotes the 2-norm, $\|\vec{r}(t) - \vec{s}\|$ is the actual range, and $\vec{\xi}(t)$ is a zero-mean Gaussian measurement noise vector.

Without loss of generality, assuming the source is at the origin, the navigation model of the vehicle moving in 3D can be written as

$$\dot{\vec{r}}(t) = \vec{v}(t) \tag{4.1}$$
$$y(t) = \frac{\left\| \vec{r}(t) + \vec{\xi}(t) \right\|^2}{2}$$

where $\vec{v}(t) \in \mathbb{R}^3$ is the velocity vector (input), and $y(t)$ is the measurement. The problem is then to estimate the position from the measurement $y(t)$.

In the pipeline inspection application, assuming a flat piecewise affine pipeline geometry and a constant altitude for the UAV flying above it, this model can be transformed into a simpler model.

Please note that the observability and state estimation of this nonlinear model depend on the input. Therefore, estimation methods are studied for different inputs and vehicle motions. In [122], the estimation problem under the helical and affine motions in 3D is addressed using the nonlinear estimator. Here, the nonlinear estimator-based navigation algorithm is demonstrated for vehicles with piecewise affine motion.

### 4.2.2 Picewise Affine Motion in 2D

Inspired by the pipeline inspection scenario, the navigation geometry (top view) of a flat pipeline is shown in Figure. 4.1. There are several fixed sources installed at different waypoints. The route between every two consecutive waypoints $O_j$ and $O_{j+1}$ is a straight line on the East-North (EN) plane with a known bearing angle $\theta_j$ from North. Let $I_0$ denote an inertial reference frame consisting of the East-North (EN) plane in the East-North-Up (ENU) coordinate system. Furthermore, let the symbol $I_j,\ j = 1, 2, \ldots, N$ denote an inertial local reference frame aligned with $I_0$, with its origin located at the position of the $j$-th waypoint. Let $B_j$ represent a local reference frame, wherein the $X_j$ axis is oriented along the straight line between the $j$-th waypoint and the $(j+1)$-th waypoint (see Figure. 4.1).

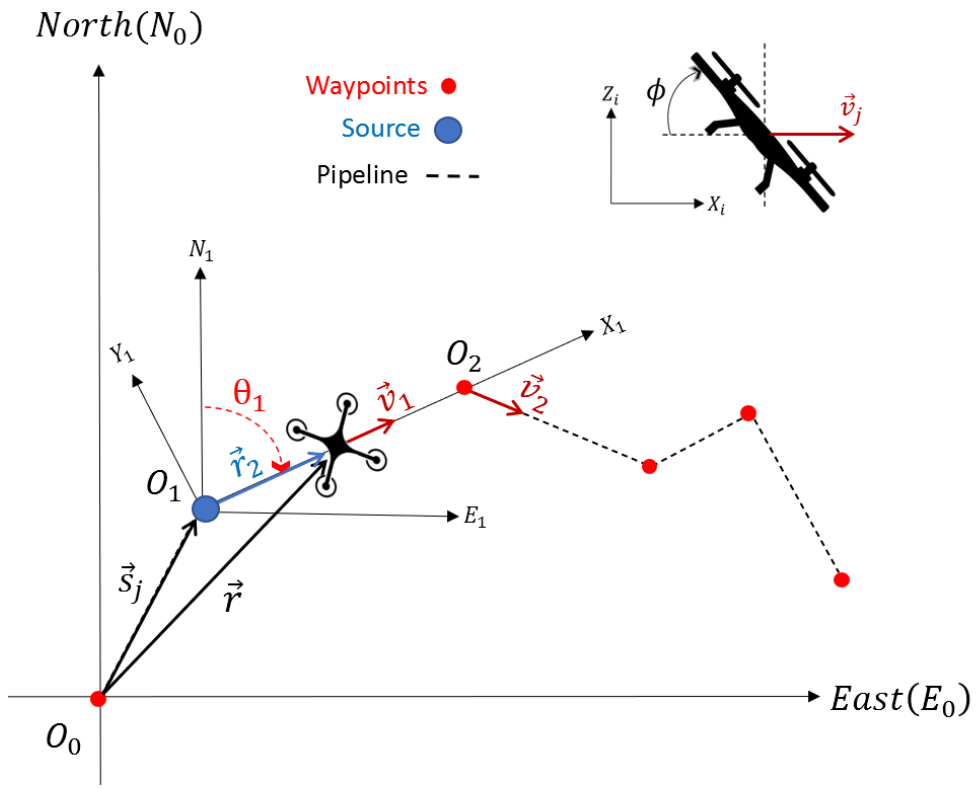


Figure 4.1: Navigation geometry with several waypoints.

Operating as an aerial inspector, the quadrotor maintains a constant altitude from the pipeline while flying above it. The quadrotor utilizes the squared range measurements to navigate, exclusively sourced from the waypoint from which it is progressively distancing itself. The position of the quadrotor and the source located at the $j$-th waypoint expressed in $I_0$ are denoted by $\vec{r}(t)$ and $\vec{s}_j$ respectively. The coordinates of the quadrotor's relative position vector $\vec{r}_j(t) = \vec{r}(t) - \vec{s}_j$ are expressed in $I_j$. The coordinates of any vector $\vec{r}$ in a frame $I_j$ are denoted by ${}^{I_j}[\vec{r}]$. From section 2.2.2, the rotation matrix $\mathcal{R}_{B_j}^{I_j}$ is

$$\begin{bmatrix} \sin(\theta_j) & -\cos(\theta_j) \\ \cos(\theta_j) & \sin(\theta_j) \end{bmatrix} \tag{4.2}$$

where $\theta_j$ is the clockwise bearing angle between the North axis of $I_j$ and the $X_j$ axis of frame $B_j$. The coordinates of the quadrotor's relative position vector expressed in $I_j$ are given by

$$\begin{aligned} {}^{I_j}[\vec{r}_{PO_j}(t)] &= \mathcal{R}_{B_j}^{I_j\ B_j}[\vec{r}_{PO_j}(t)] \\ &= \begin{bmatrix} \sin(\theta_j) & -\cos(\theta_j) \\ \cos(\theta_j) & \sin(\theta_j) \end{bmatrix} \begin{bmatrix} x_j(t) \\ 0 \end{bmatrix} \\ &= \begin{bmatrix} \sin(\theta_j) \\ \cos(\theta_j) \end{bmatrix} x_j(t) \end{aligned} \tag{4.3}$$

where $x_j(t)$ is the displacement of the quadrotor relative to the source at $O_j$ along $X_j$. Ignoring the drag, the quadrotor's model in each segment while flying at a constant altitude along $X_j$ is

$$\begin{bmatrix} \dot{x}_j(t) \\ \dot{v}_j(t) \end{bmatrix} = \begin{bmatrix} 0 & 1 \\ 0 & 0 \end{bmatrix} \begin{bmatrix} x_j(t) \\ v_j(t) \end{bmatrix} + \begin{bmatrix} 0 \\ g \end{bmatrix} tan(\phi) \tag{4.4}$$

where $v_j(t)$ is the velocity of the quadrotor along $X_j$, $\phi$ is the pitch angle shown in Fig. 4.1, and $g$ is the gravitational acceleration. Note that by properly choosing the angle $\phi(t)$, one can determine the time evolution of the velocity $v_j(t)$. Therefore, we will consider the input signal of the system to be the velocity $v_j(t)$.

Considering motion in each segment $j$ in the local coordinate frame $B_j$, one can write the quadrotor dynamics with squared range measurements perturbed by zero-mean Gaussian noise $\xi(t)$ with variance $\sigma_W^2$ as

$$\begin{aligned} \dot{x}_j(t) &= v_j(t) \\ y_j(t) = \frac{(x_j(t)+\xi(t))^2}{2} &= \frac{1}{2}x_j^2(t) + \frac{1}{2}\xi^2(t) + x_j(t)\xi(t), \end{aligned} \tag{4.5}$$

**Problem formulation:** Given

- the positions of the waypoints $O_j, j = 1, \ldots, N$ and the straight paths connecting them (i.e., $\theta_j, j = 1, \ldots, n$),
- a constant altitude $h_0$ from the flat pipeline for the autonomous vehicle,
- range measurements of the squared distance to the source emitter located at the departure waypoint which are perturbed by Gaussian white noise,

and assuming that

1. the initial position is above the pipeline,
2. a controller to maintain a constant altitude and to hover to change direction is available,
3. wind and drag are neglectable,

and given the navigation model in (4.1), design $\vec{v}(t)$ that makes the position $\vec{r}(t)$ observable at each pipeline segment and keeps the quadrotor flying on top of the pipeline geometry at all times. Additionally, propose an estimator for $\hat{x}_j(t)$ that guarantees that $\mathbb{E}[\delta x_j(t)] \to 0$ as $t \to \infty$, where $\mathbb{E}[.]$ is the mathematical expectation operator, and $\delta x_j(t) = x_j - \hat{x}_j(t)$. Moreover, design and simulate a waypoint navigation algorithm using the proposed estimator for a quadrotor in a pipeline inspection task. The quadrotor must remain within safe proximity to the pipeline while covering the entirety of the structure.

## 4.3 Methodology

### 4.3.1 Noise Approximation

The first step in solving the estimation problem is to simplify the noise. To do so, a new variable can be defined for the noise term as

$$\eta(t) = \frac{1}{2}\xi^2(t) + x_j(t)\xi(t). \tag{4.6}$$

The thesis [19] proves that $\eta(t)$ is neither zero-mean nor a Gaussian random variable.

**Theorem 4.1.** *The mean (expected value) and the variance of $\eta(t)$ are given by*

$$\begin{aligned} \mu_\eta &:= \mathbb{E}[\eta(t)] = \frac{1}{2}\sigma_W^2 \\ \sigma_\eta^2 &:= \mathbb{E}[(\eta(t) - \mu_\eta)^2] = \frac{1}{2}\sigma_W^4 + x_j^2(t)\sigma_W^2. \end{aligned} \tag{4.7}$$

*Proof.* Following the proof in [19], since $x_j(t)$ and $\xi(t)$ are mutually independent random variables and given $\mathbb{E}[\xi(t)] = 0$, and $\mathbb{E}[\xi^2(t)] = \sigma_W^2$, then the mean of $\eta(t)$ can be found as

$$\begin{aligned} \mu_\eta := \mathbb{E}[\eta(t)] &= \mathbb{E}\Big[\frac{1}{2}\xi^2(t)\Big] + \mathbb{E}[x_j(t)\xi(t)] = \mathbb{E}\Big[\frac{1}{2}\xi^2(t)\Big] + \mathbb{E}[x_j(t)]\mathbb{E}[\xi(t)] \\ &= \frac{1}{2}\sigma_W^2 + 0 = \frac{1}{2}\sigma_W^2. \end{aligned} \tag{4.8}$$

To find the variance of $\eta(t)$, we first compute $\mathbb{E}[\eta^2(t)]$ as follows using the fact that $\mathbb{E}[\xi^3(t)] = 0$, and $\mathbb{E}[\xi^4(t)] = 3\sigma_W^4$.

$$\begin{aligned} \mathbb{E}[\eta^2(t)] &= \mathbb{E}\left[\left(\frac{1}{2}\xi^2(t) + x_j(t)\xi(t)\right)^2\right] \\ &= \mathbb{E}[\frac{1}{4}\xi^4(t)] + \mathbb{E}[x_j(t)\xi^3(t)] + \mathbb{E}[x_j^2(t)\xi^2(t)] \\ &= \frac{3}{4}\sigma_W^4 + 0 + \mathbb{E}[x_j^2(t)]\mathbb{E}[\xi^2(t)] \\ &= \frac{3}{4}\sigma_W^4 + x_j^2(t)\sigma_W^2 \end{aligned} \tag{4.9}$$

Then the variance of $\eta(t)$ is calculated as

$$\begin{aligned} \sigma_\eta^2 &:= \mathbb{E}[(\eta(t) - \mu_\eta)^2] = \mathbb{E}[\eta^2(t) - 2\eta(t)\mu_\eta + \mu_\eta^2] \\ &= \mathbb{E}[\eta^2(t)] - 2\mu_\eta\mathbb{E}[\eta(t)] + \mu_\eta^2 \\ &= \frac{3}{4}\sigma_W^4 + x_j^2(t)\sigma_W^2 - 2\mu_\eta^2 + \mu_\eta^2 \\ &= \frac{1}{2}\sigma_W^4 + x_j^2(t)\sigma_W^2. \end{aligned} \tag{4.10}$$

□

The inherent complexity of ranging errors due to signal noise presents substantial challenges in their accurate modeling. Presuming these noises to be zero-mean Gaussian is an over-simplification that requires careful consideration. However, in practice, this assumption is necessary to formulate the problem and make it treatable [19]. Practical scenarios often demonstrate that $\eta(t)$ is quite close to a zero-mean Gaussian variable, particularly when the magnitudes of the range significantly exceed the standard deviation of the measurement noise [19]. In the case of $x_j(t) \gg \sigma_W^2$, one can make the approximation $\eta(t) \approx x_j(t)\xi(t)$ which is a zero-mean Gaussian random variable. The assumption $x_j(t) \gg \sigma_W^2$ is really a rather mild assumption, as the measurements would not be usable if the measurement noise was in the same order of magnitude as the true value. However, this assumption fails when the vehicle is quite close to the source. Please refer to [123], [124], and [125] for some remarks about this matter.

### 4.3.2 Nonlinear Estimator

Assume that $dW(t) = \xi(t)dt$ represents infinitesimal displacements of Brownian motion (or Wiener process) with $\mathbb{E}[dW(t)] = 0$, and variance $\mathbb{E}[dW(t)^2] = \sigma_W^2 dt$. Using the noise approximation ($\eta(t) \approx x_j(t)\xi(t)$), one can rewrite equation (4.5) for segment $j$ as

$$\begin{aligned} dx_j(t) &= v_j(t)dt \\ z_j(t) = y_j(t)dt &= \frac{1}{2}x_j^2(t)dt + x_j(t)dW(t) \end{aligned} \tag{4.11}$$

Using the nonlinear estimator with the gain $L$ (proposed in the previous chapter) to find an estimate $\hat{x}_j(t)$ of the position

$$\begin{aligned} d\hat{x}_j(t) &= v_j(t)dt + L\left(y_j(t) - \frac{1}{2}\hat{x}_j^2(t)\right)dt \\ &= v_j(t)dt + L\left(\frac{1}{2}x_j^2(t)dt + x_j(t)dW(t) - \frac{1}{2}\hat{x}_j^2(t)dt\right). \end{aligned} \tag{4.12}$$

The estimation error SDE can then be written as

$$\begin{aligned} d\delta x_j(t) &= dx_j(t) - d\hat{x}_j(t) \\ &= v_j(t)dt - v_j(t)dt - L\left(\frac{1}{2}x_j^2(t)dt - \frac{1}{2}\hat{x}_j^2(t)dt\right) - Lx_j(t)dW(t) \\ &= -\frac{L}{2}\delta x_j(t)\big(2x_j(t) - \delta x_j(t)\big)dt - Lx_j(t)dW(t). \end{aligned} \tag{4.13}$$

The convergence theorem for the error (4.13) is now stated. The diffusion term of the error SDE (3.18) (Chapter 3) is independent of the state while it is proportional to the state in SDE (4.13).

**Theorem 4.2.** *If the trajectory $x_j(t)$ is such that*

$$|\lim_{t\to\infty} x_j(t)| = |x_{j_\infty}| \gg \frac{|\delta x_{j_\infty}|}{3}, \tag{4.14}$$

*where $\delta x_{j_\infty}$ is the stationary value of the estimation error $\delta x_j(t)$, then there is a stationary probability density $p(\delta x_{j_\infty})$ with a local maximum for $\delta x_{j_\infty} = 0$. This distribution can be approximated by the Gaussian*

$$p(\delta x_{j_\infty}) = \frac{1}{\sqrt{2\pi\sigma_\infty^2}} e^{-\frac{\delta x_{j_\infty}^2}{2\sigma_\infty^2}}, \tag{4.15}$$

*where*

$$\sigma_\infty^2 = \frac{Lx_{j_\infty}\sigma_W^2}{2}. \tag{4.16}$$

*Moreover, if $L$ is chosen such that*

$$L \ll \frac{2}{x_{j_\infty}\sigma_W^2} \tag{4.17}$$

*then $\sigma_\infty \ll 1$, and the stationary probability density is concentrated close to its mean.*

*Proof.* The proof follows the one in the previous chapter by deriving the Fokker-Planck-

Kolmogorov (FPK) equation for the given stochastic differential equation (SDE) (4.13) as

$$\frac{\partial p(t,\delta x_j)}{\partial t} = -\frac{\partial}{\partial \delta x_j}\left[F(t,\delta x_j)p(t,\delta x_j)\right] + \frac{1}{2}\frac{\partial^2}{\partial \delta x_j^2}\left[D(t,\delta x_j)p(t,\delta x_j)\right], \tag{4.18}$$

where $p(t,\delta x_j)$ is the PDF of error $\delta x_j(t)$, $F(t,\delta x_j)$ is the the drift coefficient and $D(t,\delta x_j)$ is the diffusion coefficient given by

$$\begin{aligned} F(t,\delta x_j) &= -\frac{L}{2}\left(2x_j(t)\delta x_j - \delta x_j^2\right) \\ D(t,\delta x_j) &= L^2\sigma_W^2 x_j^2(t). \end{aligned} \tag{4.19}$$

Substitute the expressions for $F(t,\delta x_j)$ and $D(t,\delta x_j)$:

$$\frac{\partial p(t,\delta x_j)}{\partial t} = \frac{\partial}{\partial \delta x_j}\left[\frac{L}{2}\left(2x_j(t)\delta x_j - \delta x_j^2\right)p(t,\delta x_j)\right] + \frac{1}{2}\frac{\partial^2}{\partial \delta x_j^2}\left[L^2 x_j^2(t)\sigma_W^2 p(t,\delta x_j)\right] \tag{4.20}$$

The stationary distribution is the PDF $p_s(\delta x_{j_\infty})$ that does not change with time. Thus, the time derivative of the PDF is zero, i.e.,

$$\frac{\partial p_s(\delta x_{j_\infty})}{\partial t} = 0$$

Substitute this into the FPK equation and given $x_j(t) = x_{j_\infty}$ in the stationary state,

$$\begin{aligned} 0 &= \frac{\partial}{\partial \delta x_{j_\infty}}\left[\frac{L}{2}\left(2x_{j_\infty}\delta x_{j_\infty} - \delta x_{j_\infty}^2\right)p_s(\delta x_{j_\infty})\right] + \frac{1}{2}\frac{\partial^2}{\partial \delta x_{j_\infty}^2}\left[L^2 x_{j_\infty}^2\sigma_W^2\ p_s(\delta x_{j_\infty})\right] \\ &= Lx_{j_\infty}\left(p_s(\delta x_{j_\infty}) + \delta x_{j_\infty}\frac{\partial p_s(\delta x_{j_\infty})}{\partial \delta x_{j_\infty}}\right) - \frac{L}{2}\left(2\delta x_{j_\infty}p_s(\delta x_{j_\infty}) + \delta x_{j_\infty}^2\frac{\partial p_s(\delta x_{j_\infty})}{\partial \delta x_{j_\infty}}\right) + \frac{L^2 x_{j_\infty}^2\sigma_W^2}{2}\frac{\partial^2 p_s(\delta x_{j_\infty})}{\partial \delta x_{j_\infty}^2} \\ &= L\left(x_{j_\infty} - \delta x_{j_\infty}\right)p_s(\delta x_{j_\infty}) + L\left(x_{j_\infty}\delta x_{j_\infty} - \frac{1}{2}\delta x_{j_\infty}^2\right)\frac{\partial p_s(\delta x_{j_\infty})}{\partial \delta x_{j_\infty}} + \frac{L^2 x_{j_\infty}^2\sigma_W^2}{2}\frac{\partial^2 p_s(\delta x_{j_\infty})}{\partial \delta x_{j_\infty}^2} \\ &= \frac{\partial^2 p_s(\delta x_{j_\infty})}{\partial \delta x_{j_\infty}^2} + \frac{1}{Lx_{j_\infty}^2\sigma_W^2}\left(2x_{j_\infty}\delta x_{j_\infty} - \delta x_{j_\infty}^2\right)\frac{\partial p_s(\delta x_{j_\infty})}{\partial \delta x_{j_\infty}} + \frac{1}{Lx_{j_\infty}^2\sigma_W^2}\left(2x_{j_\infty} - 2\delta x_{j_\infty}\right)p_s(\delta x_{j_\infty}) \end{aligned} \tag{4.21}$$

Moreover, since $p_s(\delta x_{j_\infty})$ is just a function of $\delta x_{j_\infty}$, one can write the following second-order

ordinary differential equation (ODE)

$$\frac{d^2 p_s(\delta x_{j_\infty})}{d\delta x_{j_\infty}^2}+\frac{1}{L x_{j_\infty}^2 \sigma_W^2}\left(2x_{j_\infty}\delta x_{j_\infty}-\delta x_{j_\infty}^2\right)\frac{dp_s(\delta x_{j_\infty})}{d\delta x_{j_\infty}}+\frac{1}{L x_{j_\infty}^2 \sigma_W^2}\left(2x_{j_\infty}-2\delta x_{j_\infty}\right)p_s(\delta x_{j_\infty})=0. \tag{4.22}$$

The solution of this linear second-order ODE with polynomial coefficients can be solved by integration leading to the following first-order linear equation [126].

$$\frac{dp_s(\delta x_{j_\infty})}{\delta x_{j_\infty}}+\left(\frac{-1}{L x_{j_\infty}^2 \sigma_W^2}\delta x_{j_\infty}^2+\frac{2}{L\sigma_W^2 x_{j_\infty}}\delta x_{j_\infty}\right)=c \tag{4.23}$$

The constant $c$ must be zero for a local maximum at $\delta x_{j_\infty}=0$. Then the solution of this ODE is

$$p(\delta x_{j_\infty})=p_0 e^{-\frac{\delta x_{j_\infty}^2}{2\sigma_\infty^2}\left(1-\frac{\delta x_{j_\infty}}{3x_{j_\infty}}\right)}, \tag{4.24}$$

where $\sigma_\infty^2$ is given by expression (4.16). The result then follows from assumption (4.14). □

A navigation algorithm design is still required to ensure that the quadrotor maintains its piecewise affine trajectory above the pipeline geometry. This includes designing a velocity for each segment that makes the quadrotor fly on a straight line aligned with the pipeline. Moreover, the quadrotor needs a switching algorithm at each turning point (waypoint) to change direction and sync with the new range source located at the departure waypoint.

### 4.3.3 Piecewise Affine Trajectory

In this section, the conditions under which the nonlinear estimator (4.12) is applicable to the quadrotor navigation system with piecewise affine motion are investigated. Consider the noiseless navigation model in the pipeline segment $j$:

$$\begin{aligned}\dot{\vec{r}}_j(t)&=\vec{v}_j(t)\\ y(t)&=\frac{\|\vec{r}_j(t)\|^2}{2}.\end{aligned} \tag{4.25}$$

One can use a nonlinear observer of the following form to estimate the position,

$$\dot{\hat{\vec{r}}}_j(t) = \vec{v}_j(t) + \vec{L}\big(y(t) - \hat{y}(t)\big) \tag{4.26}$$

where $\hat{\vec{r}}_j$ is the estimated position vector and $\vec{L}$ is the observer gain vector. The error dynamics is given by

$$\begin{aligned} \dot{\delta\vec{r}}(t) &= \dot{\vec{r}}_j(t) - \dot{\hat{\vec{r}}}_j(t) \\ &= -\vec{L}\left(\frac{(r_j)^T r_j - (\hat{r}_j)^T \hat{r}_j}{2}\right) \\ &= -\frac{\vec{L}}{2}\big(2r_j(t) - \delta r(t)\big)^T \delta r(t) \end{aligned} \tag{4.27}$$

where $\delta\vec{r}(t)$ is the error vector and the notation $(r_j)^T$ is used for transpose of the column array with the coordinates of vector $\vec{r}_j$. Let the coordinates of any vector expressed in the local frame $B_j$ be shown in bold letters $\big($such as ${}^{B_j}[\vec{r}_j(t)] = \mathbf{r}(t)$ and ${}^{B_j}[\vec{v}_j(t)] = \mathbf{v}(t)\big)$ for simplicity of notation. Then the complete dynamic model equations are

$$\dot{\mathbf{r}}(t) = \mathbf{v}(t)$$

$$y(t) = \frac{\|\mathbf{r}(t)\|^2}{2} = \frac{1}{2}\mathbf{r}^T(t)\mathbf{r}(t) \tag{4.28}$$

$$\dot{\hat{\mathbf{r}}}(t) = \mathbf{v}(t) + \mathbf{L}\delta y(t) = \mathbf{v}(t) + \frac{\mathbf{L}}{2}\big(\,\|\mathbf{r(t)}\|^2 - \|\hat{\mathbf{r}}(t)\|^2\,\big) \tag{4.29}$$

$$\delta\dot{\mathbf{r}}(t) = -\mathbf{L}\delta y(t) = -\frac{\mathbf{L}}{2}\big(2\mathbf{r}(t) - \delta\mathbf{r}(t)\big)^T \delta\mathbf{r}(t) \tag{4.30}$$

$$\delta\dot{y}(t) = \delta\mathbf{r}(t)^T\mathbf{v}(t) - \hat{\mathbf{r}}(t)^T\mathbf{L}\delta y(t) \tag{4.31}$$

**Theorem 4.3.** *[122] If* $\mathbf{L} \neq 0$*, any equilibrium point of the error dynamics* (4.30) *satisfies*

$$\|\mathbf{r}_\infty\| = \|\hat{\mathbf{r}}_\infty\|\,. \tag{4.32}$$

*Proof.* Since $\mathbf{L} \neq 0$, the equation $\delta\dot{\mathbf{r}}(t) = 0$ yields,

$$\begin{aligned} &\left(\mathbf{r}_\infty^T - \hat{\mathbf{r}}_\infty^T\right)\left(\mathbf{r}_\infty + \hat{\mathbf{r}}_\infty\right) = 0 \\ \iff\ &\mathbf{r}_\infty^T\mathbf{r}_\infty = \hat{\mathbf{r}}_\infty^T\hat{\mathbf{r}}_\infty \end{aligned} \tag{4.33}$$

Therefore, this happens iff $\|\mathbf{r}_\infty\| = \|\hat{\mathbf{r}}_\infty\|$. □

Equation (4.32) positions $\mathbf{r}_\infty$ and $\hat{\mathbf{r}}_\infty$ on a circle with the same radius.

**Theorem 4.4.** *Assume $\vec{r}_j(0) = r_0\vec{e_j}$ (assumption 1), and let $\vec{\hat{r}}_j(0) = \hat{r}_0\vec{e_j}, \vec{L} = L\vec{e_j}$, and $\vec{v}_j(t) = v_j(t)\vec{e_j}$ where $\vec{e_j}$ is the direction vector that is tangent to the pipeline segment $j$. Then $\vec{\hat{r}}_j(t) = \hat{r}(t)\vec{e_j}$, and $\vec{r}_j(t) = r(t)\vec{e_j}$.*

*Proof.* Integrating (4.25), we have

$$\begin{aligned} \vec{r}_j(t) &= \vec{r}_j(0) + \int_0^t \vec{v}_j(s)ds \\ &= r_0\vec{e_j} + \int_0^t v(s)\vec{e_j}ds \\ &= (r_0 + V(t))\vec{e_j} = r(t)\vec{e_j} \end{aligned} \tag{4.34}$$

Similarly integrating (4.26)

$$\begin{aligned} \vec{\hat{r}}_j(t) &= \vec{\hat{r}}_j(0) + \int_0^t \vec{v}_j(s)ds + \int_0^t \vec{L}\delta y(s)ds \\ &= \hat{r}_0\vec{e_j} + \vec{e_j}\int_0^t v(s)ds + \vec{e_j}\int_0^t L\delta y(s)ds \\ &= (\hat{r}_0 + V(t) + L\delta Y(t))\vec{e_j} = \hat{r}(t)\vec{e_j} \end{aligned} \tag{4.35}$$

□

As a result of Theorem 4.4, as long as the vehicle's velocity is aligned with $X_j$, the position of the vehicle started on $X_j$, remains on it by appropriately designing $\vec{\hat{r}}(0)$ and $\vec{L}$. Moreover, $\vec{\hat{r}}_j(t)$ will be aligned with $X_j$ at all times.

**Theorem 4.5.** *[122] Let the equilibruim points of equations* (4.30) *and* (4.31) *be denoted as* $\delta\mathbf{r}_\infty$, $\delta y_\infty$. *Under the assumptions of Theorem 4.4,* $v_j \neq 0$, *and* $L \neq 0$,

1. $\delta y_\infty = 0$,
2. $\delta\mathbf{r}_\infty = 0$ *is the only equilibrium point,*
3. *moreover, if* $\delta y(t) \to 0$ *as* $t \to \infty$, *then* $\delta\mathbf{r}(t) \to 0$ *as* $t \to \infty$.

*Proof.* Since $\vec{L} = L\vec{e_j}$ with $L \neq 0$, and $\vec{v_j}(t) = v_j(t)\vec{e_j}$, then using equation (4.30) and $\delta\dot{\mathbf{r}}_\infty = 0$ yields

$$\delta y_\infty = 0. \tag{4.36}$$

For the second result, the conditions for equilibrium points of equation (4.31) imply

$$\delta\dot{y}_\infty = 0, \tag{4.37}$$

and $\delta y(t) = \delta y_\infty = 0$ is a constant equilibrium point of (4.31). At a constant equilibrium point $\delta\mathbf{r}(t) = \delta\mathbf{r}_\infty$. From equation (4.31) we have

$$\delta\mathbf{r}_\infty^T\mathbf{v}_\infty = 0. \tag{4.38}$$

Since $\mathbf{v}_\infty$ and $\delta\mathbf{r}_\infty$ are both aligned with $X_j$ (Theorem 4.4), they cannot be orthogonal. Given that $\mathbf{v}_\infty \neq 0$, from this dot product we conclude that $\delta\mathbf{r}_\infty = 0$.
Finally, since $\delta y(t)$ is the difference of two squared norms, it is uniformly continuous. By invoking Barbalat's Lemma and given the uniform continuity of $\delta y(t)$, one must have $\delta\dot{y}(t) \to 0$ as $t \to \infty$. Then from equation (4.31) we conclude that $\delta\mathbf{r}(t) \to 0$ as $t \to \infty$ [122]. □

Based on these theorems, the nonlinear estimator proposed can be used to estimate the position of the quadrotor in each pipeline segment provided $\delta y \to 0$ as $t \to \infty$.
The proposed quadrotor navigation algorithm will be divided into three sections: initialization, flying forward, and changing direction.

### 4.3.4 Initialization of the Quadrotor

The first phase involves positioning the quadrotor directly above the first pipeline segment at an altitude distance $h_0$ above each range measurement emitter stationed at the waypoints to avoid colliding. (The navigation problem with the vehicle starting off the pipeline has been studied in [122].) Figure 4.2 shows a quadrotor in a pipeline inspection mission. Since $h_0$ is known to or measured by the quadrotor, it can find $x_j$ from the range using the Pythagorean theorem. Moreover, the initial estimation is in the form $\vec{\hat{r}}(0) = \hat{r}(0)\vec{e}_j$, and $L \neq 0$ at all time.

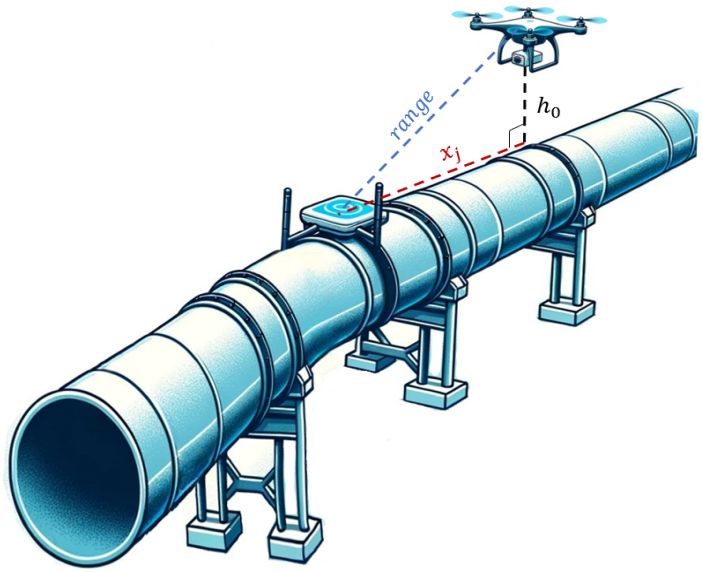


Figure 4.2: A quadrotor in a pipeline inspection mission. (This picture is generated by DALL-E-3, a modern text-to-image AI tool released by OpenAI [127].)

### 4.3.5 Flying Forward

The velocity (input) design with the feedback of position estimation is proposed for the quadrotor in each pipeline segment as

$$\vec{v}_j(t) = -\alpha\vec{\hat{r}}_j(t) + \vec{\beta}_j, \tag{4.39}$$

where the initial estimate is chosen as $\vec{\hat{r}}_j(0) = \hat{r}(0)\vec{e}_j \neq \frac{\vec{\beta}_j}{\alpha}$, and $\alpha \neq 0 \in \mathbb{R}^1$ and $\vec{\beta}_j = \beta_j \vec{e}_j \in \mathbb{R}^2$ are the design parameters.

To find the final position of the quadrotor, one can rewrite (4.39) as

$$\begin{aligned} \vec{v}_j(t) = \dot{\vec{r}}_j(t) &= -\alpha\big(\vec{r}_j(t) - \vec{\delta r}(t)\big) + \vec{\beta}_j \\ &= -\alpha \vec{r}_j(t) + \vec{\gamma}(t), \end{aligned} \tag{4.40}$$

where $\vec{\gamma}(t) = \alpha \vec{\delta r}(t) + \vec{\beta}_j$. Given the initial condition $\vec{r}_j(0)$,

$$\vec{r}_j(t) = \vec{r}_j(0)e^{-\alpha t} + \int_0^t e^{-\alpha(t-\tau)}\vec{\gamma}(\tau)d\tau. \tag{4.41}$$

For all the simulations in chapter 3, the position $\vec{r}_{j_\infty}$ converged to the steady-state value $\vec{\beta}_j/\alpha$. For the quadrotor to fly from $\vec{r}_j(0)$ to the next waypoint, $\vec{\beta}_j/\alpha$ is thus chosen as $O_{j+1}$ (the position of the next waypoint).

Moreover, from Theorem 4.4, one can write $\vec{\beta}_j = \beta_j \vec{e}_j$ and $\vec{\hat{r}}_j(t) = \hat{r}(t)\vec{e}_j$, and using equation (4.39) we have

$$\vec{v}_j(t) = -\alpha \hat{r}(t)\vec{e}_j + \beta_j \vec{e}_j = v_j(t)\vec{e}_j. \tag{4.42}$$

So this design also aligns the velocity vector with the pipeline segment. The values of $\alpha$ and $\beta_j$ must be chosen to make $\hat{r}(t) \neq \frac{\beta_j}{\alpha}$ so that the assumption $v_j(t) \neq 0$ is satisfied.

### 4.3.6 Changing direction

One of the key benefits of quadrotor UAVs is their ability to perform yaw motion while maintaining stable hovering. This is achieved through the manipulation of the torque produced by the clockwise and counter-clockwise rotors, which are typically arranged in pairs. The flight controller calculates the desired rotor speeds to achieve the desired yaw motion. The ability to perform yaw motion in a hover state allows quadrotors to change direction in hovering mode before switching to motion toward the next waypoint.

The quadrotor's model in each segment can be written in 1D as in equation (4.5). Each time the quadrotor reaches a waypoint, the model will switch to the exact same dynamics, only with different initial positions, velocities, and measurement values. This system can be viewed as a hybrid system, since it exhibits continuous dynamics and discrete-event switching. A common issue in designing switching logic for a system is avoiding "chattering," which refers to rapid, undesirable switching. The switching strategy utilized in the proposed navigation system is shown in Algorithm 1 with its flowchart shown in Figure 4.3. This method guarantees that the switch does not activate immediately in response to minor changes, thereby preventing potential chattering due to the uncertainties in estimation. Moreover, the system is designed to wait a certain dwell time before switching again to a new subsystem which is also important since the estimation is unreliable when the quadrotor is close to the departure waypoint.

**Algorithm 1** Waypoint Switch Algorithm

**Input:** waypoints, estimated_position, current_time
**Parameter:** *threshold* = 0.2 m, *dwell_time* = 1 s
**Output:** segment_number

Initialize persistent variables: current_segment, last_switch_time
**if** *current_segment* is empty **then**
  *current_segment* ← 1
**end if**
**if** *last_switch_time* is empty **then**
  *last_switch_time* ← 0
**end if**
**if** (*current_time* - *last_switch_time*) > *dwell_time* **then**
  **for** $i = 1$ **to** *size*(waypoints, 2) **do**
    *distance* ← norm(*estimated_position* - *waypoints*(:, $i$))
    **if** *distance* < *threshold* **and** *current_segment* ≠ $i$ **then**
      *current_segment* ← $i$
      *last_switch_time* ← *current_time*
      **break**
    **end if**
  **end for**
**end if**
*segment_number* ← *current_segment*

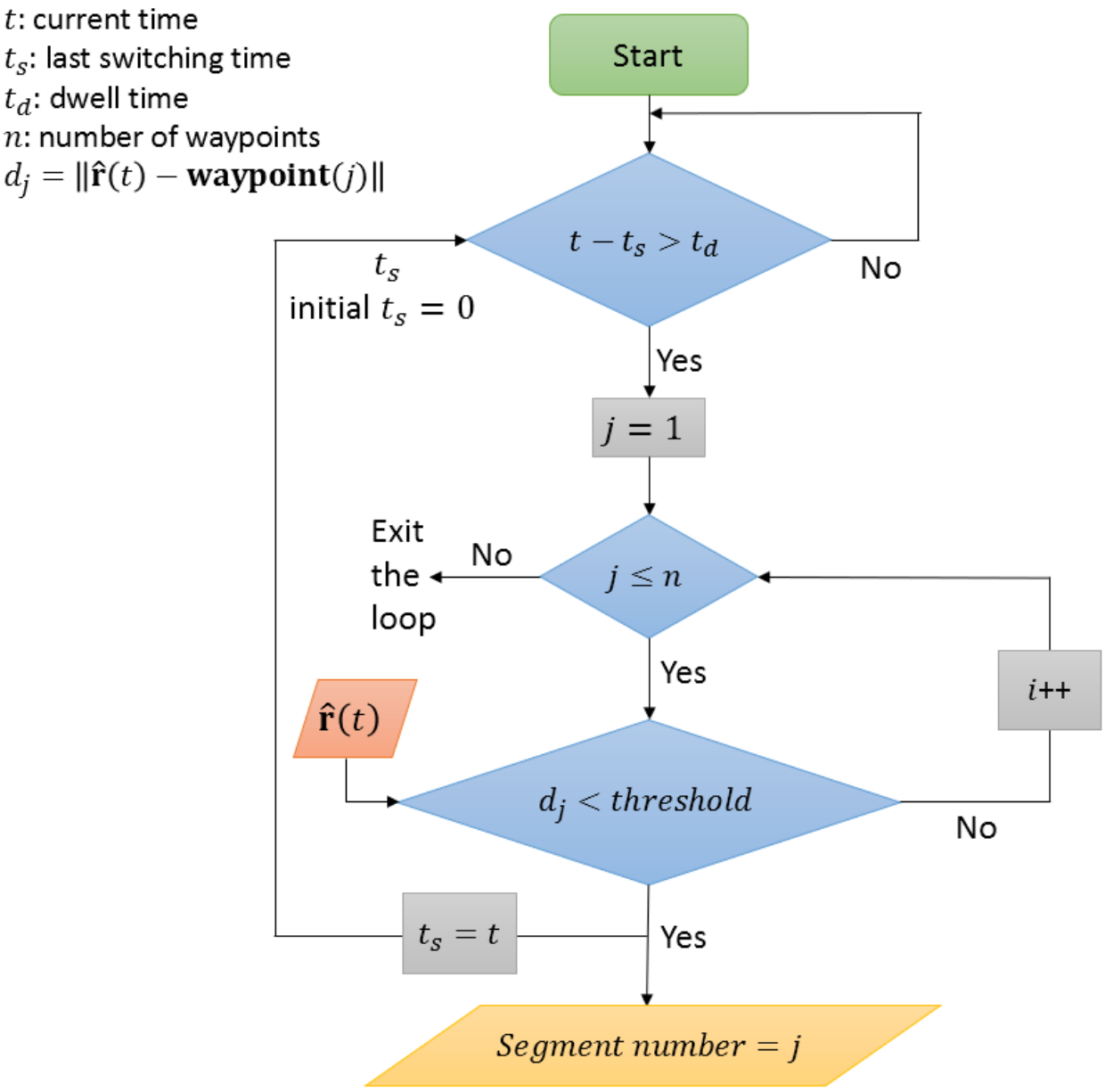


Figure 4.3: Flowchart of the switching algorithm

The block diagram in Figure 4.4 represents the estimation and control framework of our proposed navigation system for a quadrotor in the inspection of pipelines. This diagram includes several critical components. Primarily, the "Controller (Input Design)" block, which is formulated in accordance with equation (4.39). This block is responsible for designing the input controls for the quadrotor. It utilizes the 2D estimated position of the quadrotor along with the position of the upcoming waypoint which the quadrotor is navigating toward. Furthermore, the quadrotor model with noisy range measurements is defined by equation (4.1). The block "1D Nonlinear Estimator" operates based on the dynamics outlined in equation (4.12), and "1D to 2D Transformation" is based on equation (4.3). Lastly, the switching algorithm, an essential aspect of the navigation system, is described in the previous section.

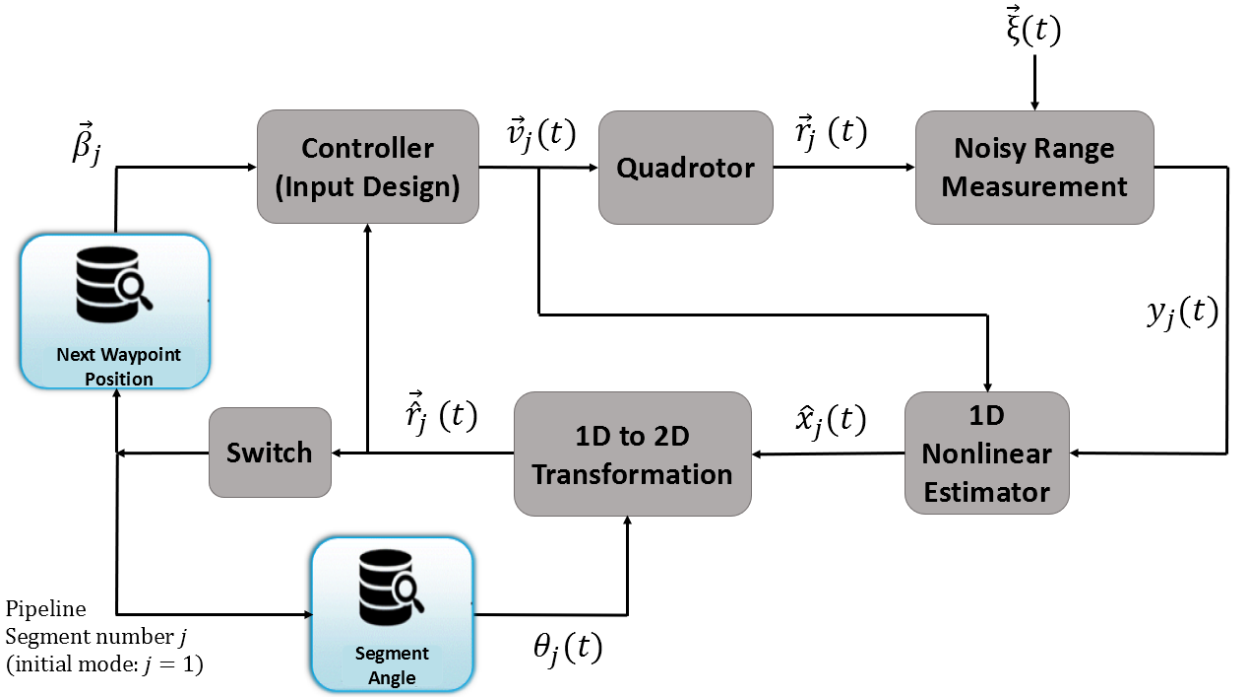


Figure 4.4: Block diagram of the estimation and control

## 4.4 Simulation Results

This section presents the simulation results of a practical case study that underscores the application of a nonlinear estimator in a real-world navigation setting. The focus of this case study is accurate position estimation in a quadrotor's navigation system, which is designed for pipeline inspection operations in a waypoint scenario. The quadrotor only measures the squared range perturbed by noise to show the practicality and reliability of this method in GPS-denied environments.

Similar to Figure 4.1, two pipeline geometries with five segments are considered and assumed to be known. In each illustrative scenario, the navigation algorithm is designed to enable the quadrotor to perform the inspection task. The quadrotor initiates its flight from an arbitrary point at $h_0 = 1$ meters above the pipeline. The objective is for the quadrotor to autonomously navigate and fly along the entire span of the pipeline's geometry, ensuring comprehensive and consistent coverage. Moreover, using the nonlinear estimator, the quadrotor is tasked with estimating its position in the $East - North$ $(E_0 - N_0)$ frame. This navigation system has access to the squared range measurements from the sources from which the quadrotor is flying away at each segment. These measurements are crucial, yet they are perturbed by Gaussian white noise with zero-mean and a variance of $0.1\,m$. The gain of the nonlinear observer is selected as $L = 1$ in all simulations.

The velocity (input) of the quadrotor is designed based on equation (4.39) at each pipeline segment. Upon arriving at a waypoint, this input undergoes modification through the adjustment of the vector parameter $\vec{\beta}_j$, aligning it with the position of the next waypoint.

All the system, input, and measurement models are designed in 2D, assuming the pipeline has a constant altitude, and the quadrotor flies at a constant altitude. The position estimation using the nonlinear estimator is necessary here to navigate through the pipeline and determine above which segment the quadrotor is flying.

### 4.4.1 First Pipeline Geometry with 5 Segments

In the first scenario, the navigation geometry of a pipeline with 6 waypoints (5 segments) is assumed to be known with the position of the waypoints as given in Table 4.1, and the clockwise angle between the pipeline segments and $E_0$ as shown in Table 4.2. The quadrotor's initial position is $(0, 0)$ and the initial estimation is $(0.98, 2.85)$. The real and estimated trajectories of the quadrotor in the top view (2D, East-North frame) are shown in Figure 4.5. The pipeline with a diameter of $1\,m$ is also depicted.

Table 4.1: Position of the Waypoints in Meters

| | Waypoint 1 | Waypoint 2 | Waypoint 3 | Waypoint 4 | Waypoint 5 | Waypoint 6 |
|---|---|---|---|---|---|---|
| Position | $\begin{pmatrix} 0 \\ 0 \end{pmatrix}$ | $\begin{pmatrix} 10 \\ 5 \end{pmatrix}$ | $\begin{pmatrix} 15 \\ 15 \end{pmatrix}$ | $\begin{pmatrix} 20 \\ 10 \end{pmatrix}$ | $\begin{pmatrix} 30 \\ 40 \end{pmatrix}$ | $\begin{pmatrix} 30 \\ 40 \end{pmatrix}$ |

Table 4.2: Angles in Degree

| | Segment 1 | Segment 2 | Segment 3 | Segment 4 | Segment 5 |
|---|---|---|---|---|---|
| Angle | $\theta_1 = 71.56°$ | $\theta_2 = 45°$ | $\theta_3 = -35.53°$ | $\theta_4 = -123.69°$ | $\theta_4 = -146.31°$ |

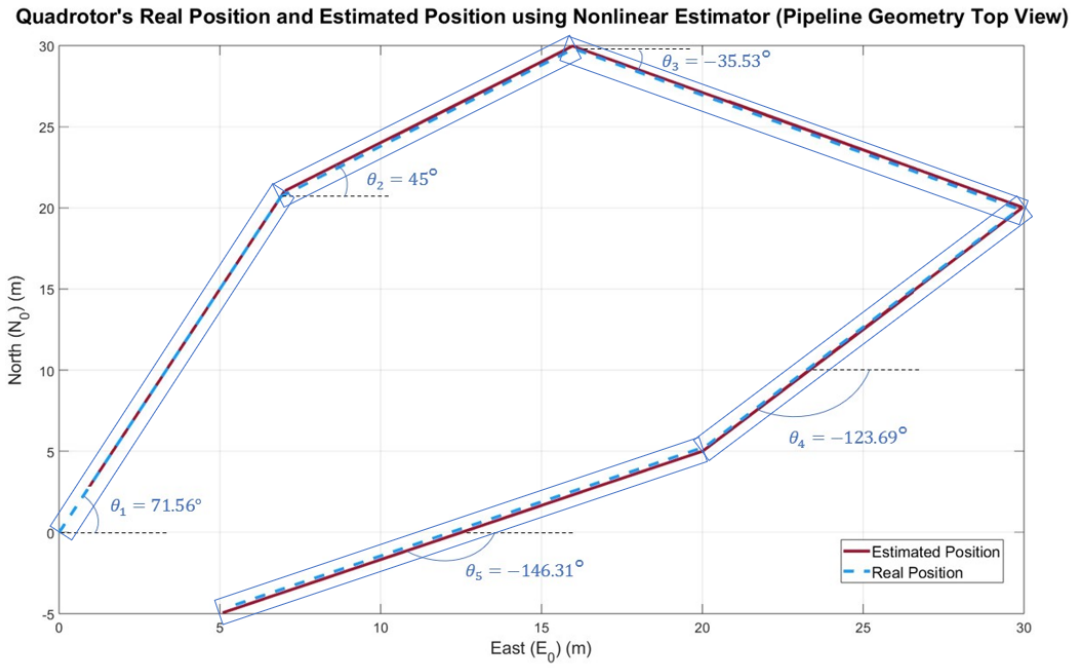


Figure 4.5: The real, and estimated position of the quadrotor in 2D (top view)

Figures 4.6 and 4.7 display the estimation error trajectories with different noise seeds along the $E_0$ axis and the $N_0$ axis respectively. The estimation error converges to a small neighborhood of zero after the switching transients subside. The variance is less than the pipeline diameter.

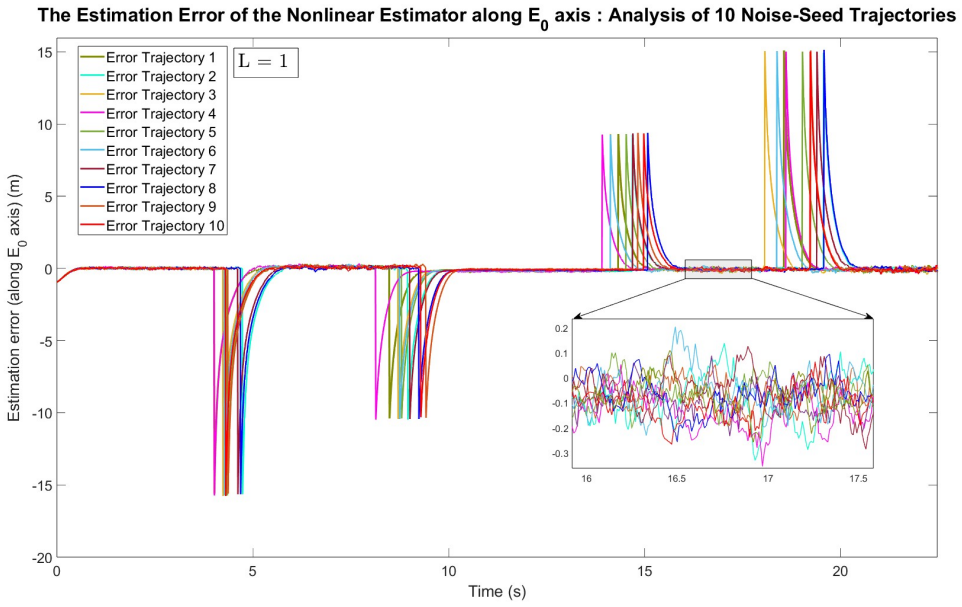


Figure 4.6: The estimation error's sample trajectories along $E_0$ axis

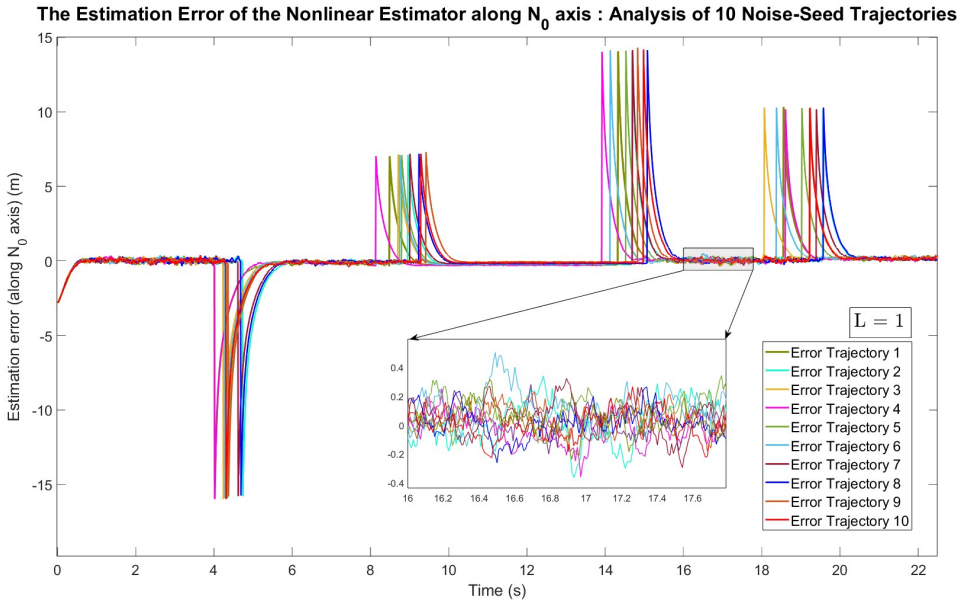


Figure 4.7: The estimation error's sample trajectories along $N_0$ axis

Figures 4.8 and 4.9 depict the designed input (velocity) trajectory of the quadrotor along $E_0$ and $N_0$ for flying on top of the pipeline (the real trajectory in Figure 4.5).

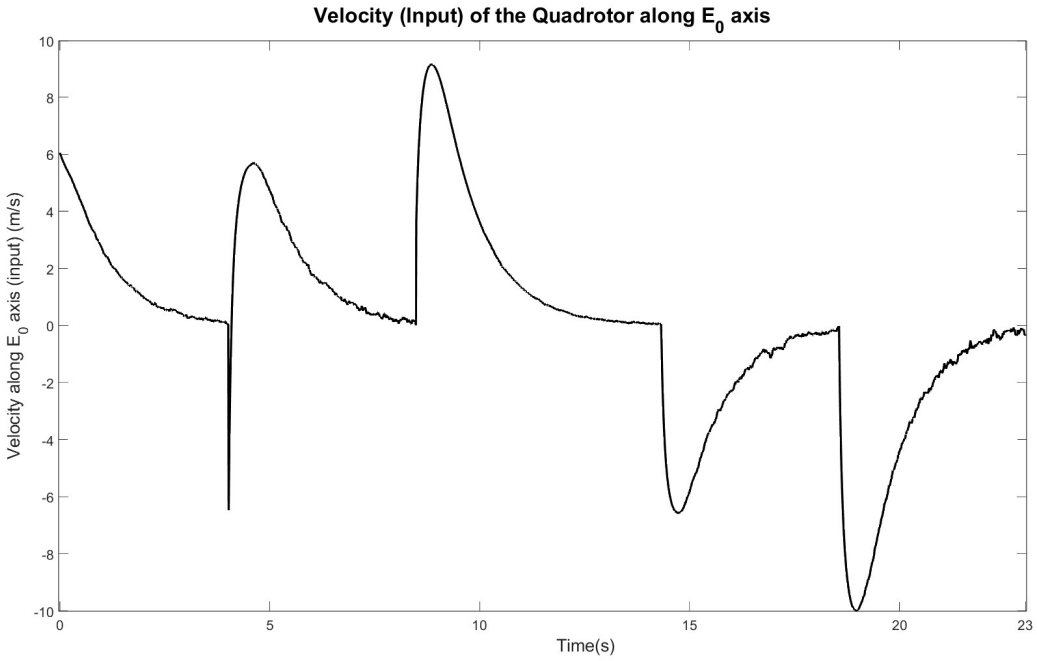


Figure 4.8: Velocity (input) of the quadrotor along $E_0$ axis

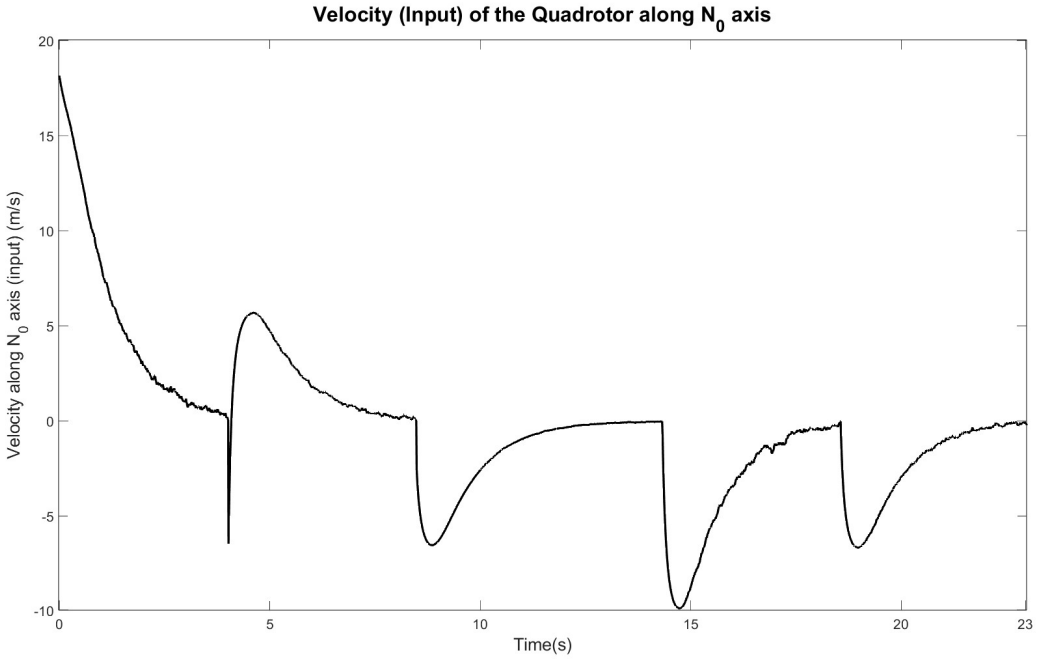


Figure 4.9: Velocity (input) of the quadrotor along $N_0$ axis

It is shown in Figures 4.10 and 4.11 that the estimation error of the nonlinear estimator will be stable and converge to a neighborhood of zero for different initial estimates.

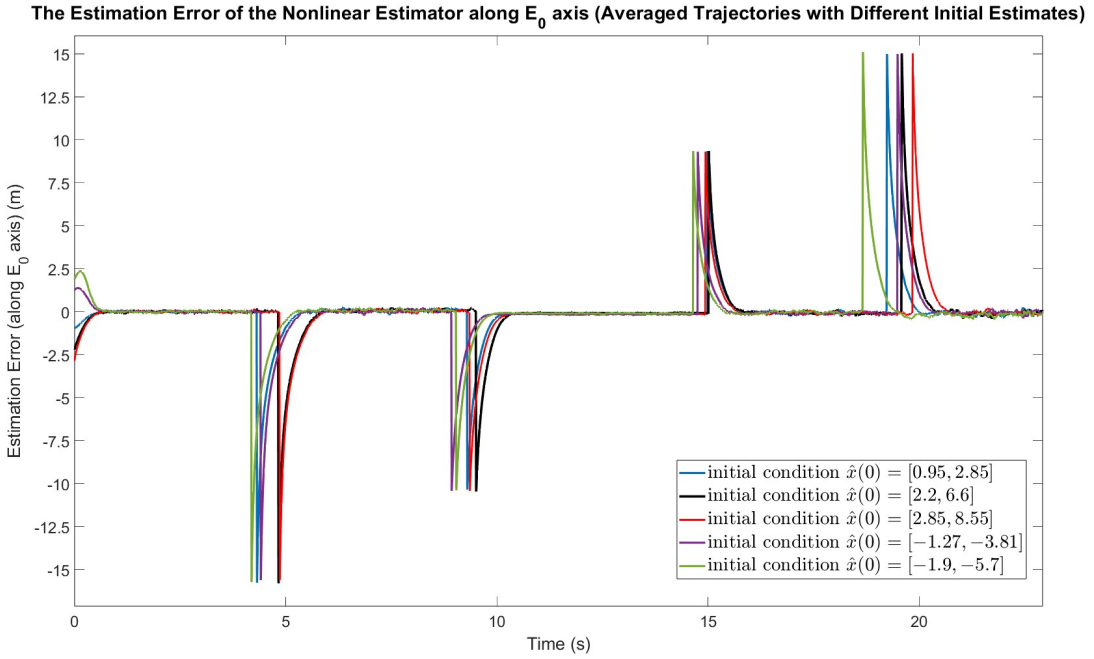


Figure 4.10: Estimation error trajectories along $E_0$ axis with different initial estimates.

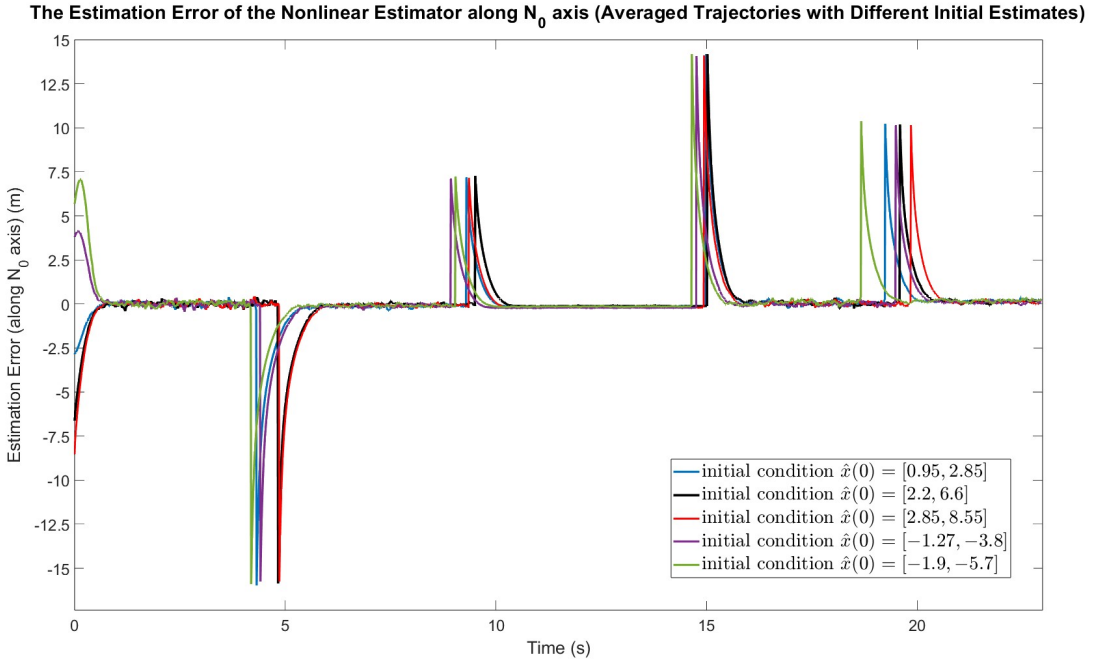


Figure 4.11: Estimation error trajectories along $N_0$ axis with different initial estimates.

### 4.4.2 Second Pipeline Geometry with 5 Segments

Another navigation geometry based on a real natural gas pipeline in Finland [128] is considered in this section. The waypoints' position is given in Table 4.3, and the clockwise angle between the pipeline segments and $E_0$ is shown in Table 4.4. The quadrotor's initial position is $(2, 57)$ and the initial estimation is $(2.8, 55.2)$. The real and estimated trajectories of the quadrotor in the top view and the pipeline with a diameter of $1\,m$ are shown in Figure 4.12.

Table 4.3: Position of the Waypoints in Meters

| | Waypoint 1 | Waypoint 2 | Waypoint 3 | Waypoint 4 | Waypoint 5 | Waypoint 6 |
|---|---|---|---|---|---|---|
| Position | $\begin{pmatrix} 0 \\ 65 \end{pmatrix}$ | $\begin{pmatrix} 10 \\ 30 \end{pmatrix}$ | $\begin{pmatrix} 30 \\ 45 \end{pmatrix}$ | $\begin{pmatrix} 40 \\ 5 \end{pmatrix}$ | $\begin{pmatrix} 60 \\ 5 \end{pmatrix}$ | $\begin{pmatrix} 80 \\ 25 \end{pmatrix}$ |

Table 4.4: Angles in Degree

| | Segment 1 | Segment 2 | Segment 3 | Segment 4 | Segment 5 |
|---|---|---|---|---|---|
| Angle | $\theta_1 = -74.05°$ | $\theta_2 = 36.87°$ | $\theta_3 = -75.96°$ | $\theta_4 = 0°$ | $\theta_5 = 45°$ |

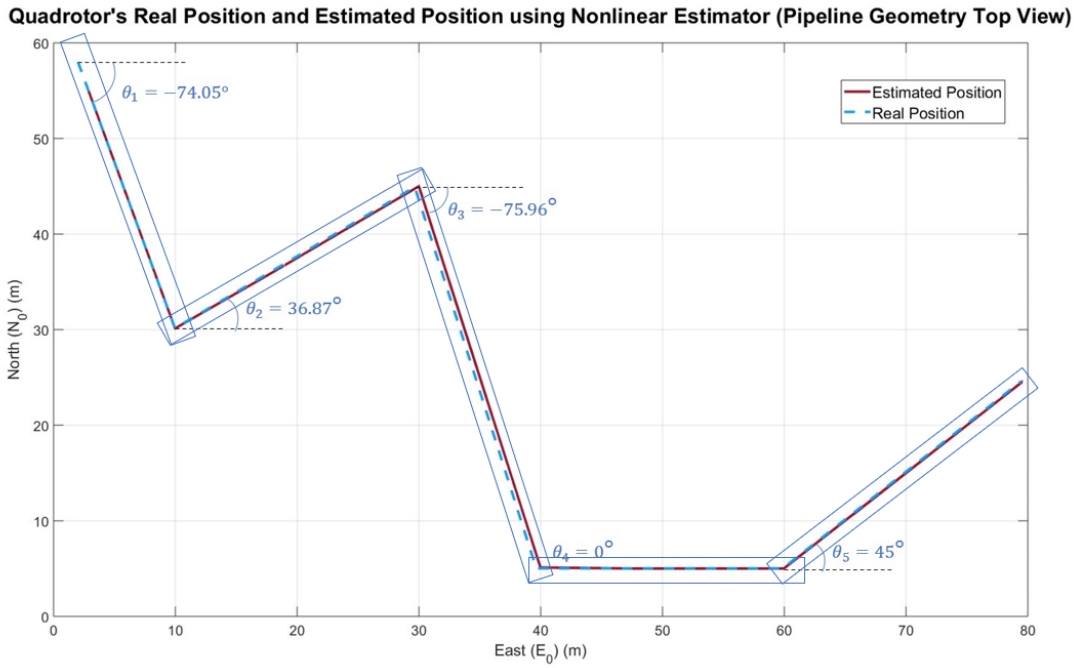


Figure 4.12: The real, and estimated quadrotor's position in 2D (top view)

Figures 4.13 and 4.14 display the estimation error trajectories with different noise seeds along the $E_0$ axis and the $N_0$ axis, respectively.

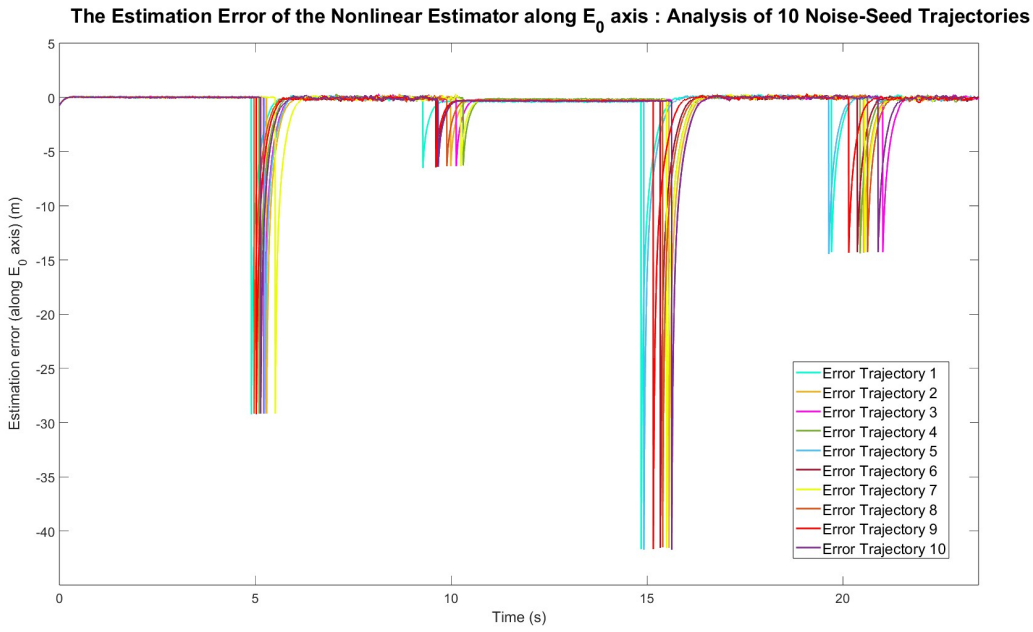


Figure 4.13: The estimation error's sample trajectories along $E_0$ axis

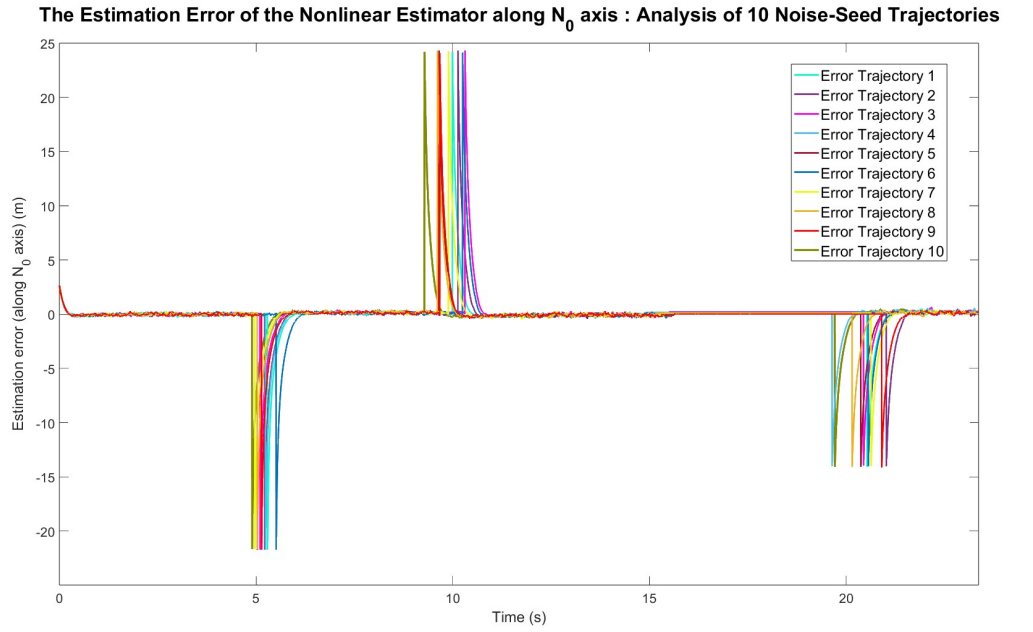


Figure 4.14: The estimation error's sample trajectories along $N_0$ axis

Figures 4.15 and 4.16 depict the designed input (velocity) trajectory of the quadrotor along $E_0$ and $N_0$ for flying on top of the pipeline (the real trajectory in Figure 4.5).

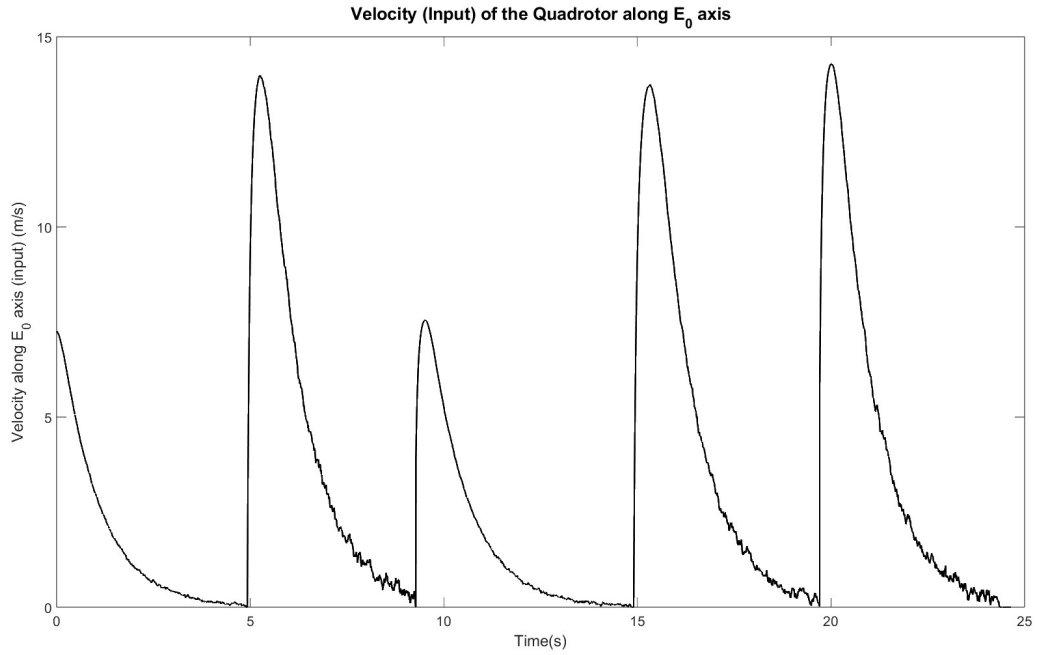


Figure 4.15: Velocity (input) of the quadrotor along $E_0$ axis

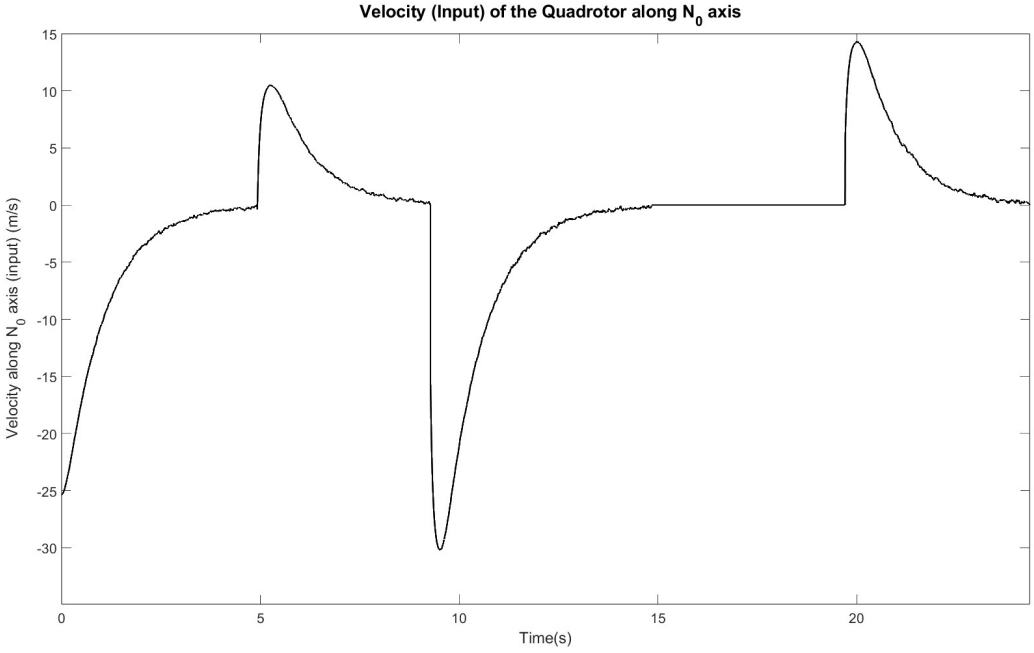


Figure 4.16: Velocity (input) of the quadrotor along $N_0$ axis

To compare our proposed nonlinear estimator to the established method in the literature, a Kalman filter is designed for the LTV augmented system. Figures 4.17 and 4.18 illustrate the averaged trajectories of the estimation error for both methods with the parameters ($L$ and noise covariances $Q$ and $R$ for Kalman filter) that yielded the best results.

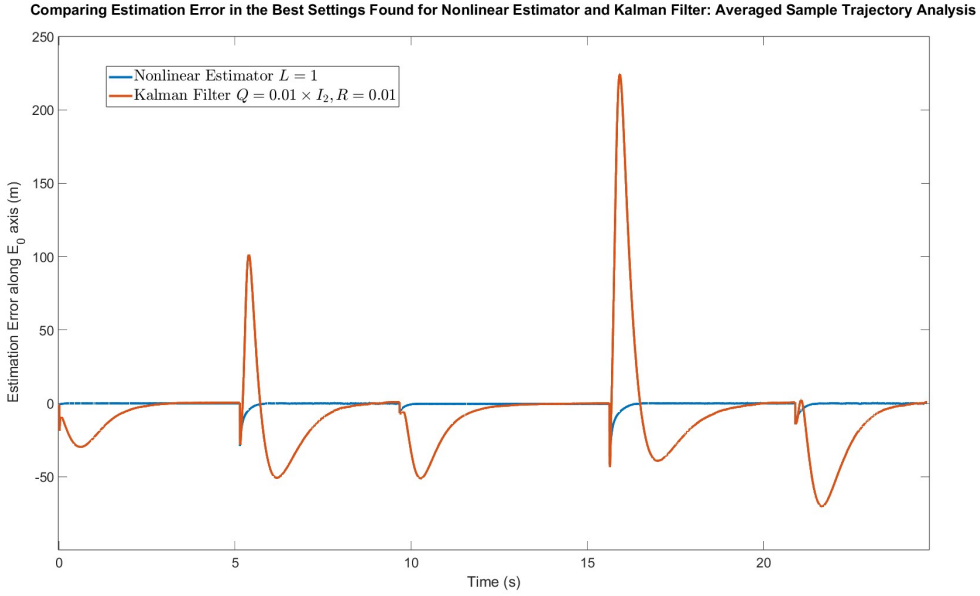


Figure 4.17: Averaged estimation error along $E_0$

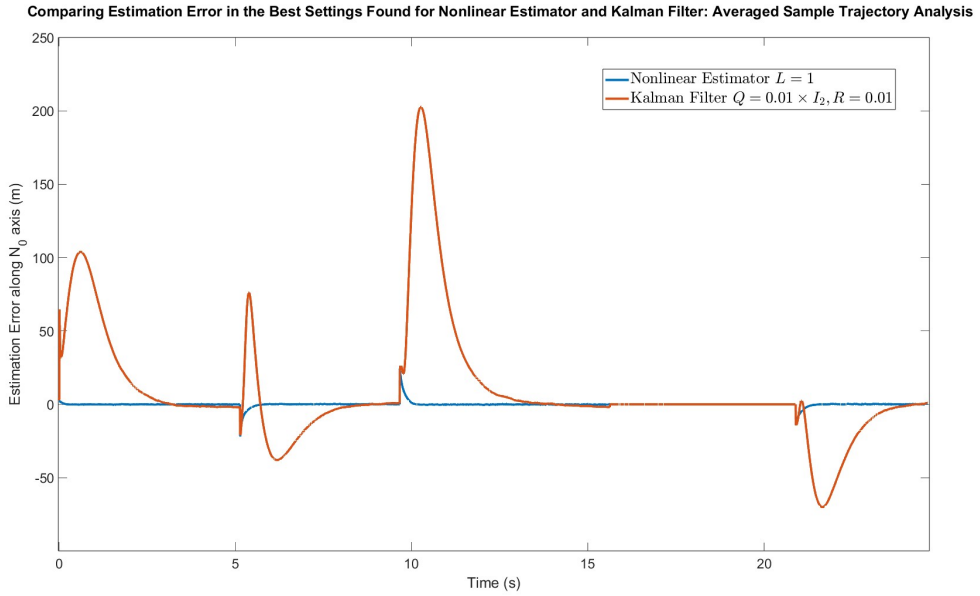


Figure 4.18: Averaged estimation error along $N_0$

The convergence time of the estimation error towards a neighborhood of zero is smaller using the nonlinear estimator when compared with the Kalman filter. The estimation error is lower for the proposed estimator than the one for the Kalman filter.

## 4.5 Conclusions

In this chapter, pipeline inspection by an autonomous UAV (quadrotor) with a waypoint-based self-navigating system is studied in a GPS-denied environment. A nonlinear estimator is proposed for the position estimation of the quadrotor using the square of noisy range measurements. The algorithm designs the velocity so that the quadrotor flies on top of the piecewise affine pipeline geometry using the estimated position.

The simulation results reveal that the estimation error is stable and the expected value converges to zero for different pipeline geometries and various initial estimates. Moreover, at the switching points (waypoints), the estimation error converges to a neighborhood around zero in all simulations, even with an inaccurate initial estimate. Finally, simulation results show that our proposed nonlinear estimator performs favorably when compared to a Kalman filter for the augmented state system.

# Chapter 5

# Conclusions and Future Work

This thesis presents a study on the development and application of a state estimation method for a class of systems with linear dynamics and noisy quadratic measurements. This study includes proposing a nonlinear estimator for applications on energy harvesters and a UAV navigation system for pipeline inspection. The performance of the nonlinear estimator is compared to the traditional Kalman filter.

Chapter 3 of this thesis introduces a nonlinear estimator for the body velocity in a kinetic energy harvester using the measurements of the generated electrical energy. The observability conditions for this system are derived based on the input, yielding that the input must be non-zero at all times for the system to be uniformly observable. Then, it has been shown that a nonlinear Verhulst logistic equation describes the estimation error dynamics. This observation unveiled a link between the state estimation using quadratic measurements and population dynamics. Moreover, the time evolution equation of the estimation error PDF is derived (the Fokker-Planck-Kolmogorov equation). It has been proved that the stationary distribution of the estimation error will converge to a zero-mean Gaussian with adjustable variance under certain assumptions (equation (3.19)).

The simulation results demonstrate the enhanced performance of the proposed nonlinear estimator in terms of convergence speed and steady-state error estimation mean (accuracy)

and variance (precision), compared to the Kalman filter using the weighting matrices tested in this thesis. The estimator not only achieved faster convergence for all inputs but also maintained convergence, unlike the Kalman filter. The mean of the estimation error for the nonlinear estimator converged to zero and its steady-state variance was less than the one for the Kalman filter in most of the simulations. Overall, the mean squared error (MSE) for the nonlinear estimator was lower than for the Kalman filter. Additionally, the nonlinear estimator was shown to be simpler to tune, representing a significant practical advantage.

In Chapter 4, the focus is shifted to the specific application of range-only vehicle navigation. The complexities introduced by non-Gaussian measurement noise are addressed by approximating this noise as zero-mean Gaussian under the condition that the vehicle is far enough from the source. The nonlinear estimator was adapted to this context. The Fokker-Planck-Kolmogorov equation was derived to find the time evolution of the estimation error PDF. It was proved that the stationary distribution of the estimation error converges to a zero-mean Gaussian with adjustable variance under certain assumptions. Thus the expected value of the estimation error was proven to converge to zero as time goes to infinity, and the stationary variance to be adjusted using the estimator gain.

The rest of Chapter 4 transitions from theoretical analysis to a practical application, showcasing the implementation of the nonlinear estimator in a simulated pipeline inspection conducted by an autonomous UAV (quadrotor). The nonlinear observer in the previous chapter is extended to a 2D case with piecewise affine motion. Moreover, it has been shown through extensive simulations that the nonlinear estimator performs well in practice for the system with measurement noise in 2D. Simulation results indicated a stable estimation error. Notably, regardless of the initial estimate, the estimation error converged to a neighborhood of zero, and the quadrotor maintained its flight path directly above the pipeline geometry.

Connecting these findings, theoretical analysis and practical applications demonstrate the nonlinear estimator's advantages over the Kalman filter. Its successful implementation in UAV navigation for pipeline inspection underscores its potential for facilitating complex au-

tonomous operations in various industries.

Potential future research directions include establishing the theoretical conditions for stability and convergence in 3D with different vehicle motions. Moreover, the performance of the nonlinear estimator can also be investigated in the presence of the process noise. The next step toward future work in the pipeline inspection application is to relax the assumptions such as "no wind and drag" and "initialization on top of the pipeline". Finally, one can investigate the use of two range signals from different sources to make the estimation more accurate even when the quadrotor is very close to the source.

# Bibliography


[1] S. Moura, "Energy systems and control - lecture notes." University of California, Berkeley, May 2018.

[2] R. Riemer and A. Shapiro, "Biomechanical energy harvesting from human motion: theory, state of the art, design guidelines, and future directions," *Journal of Neuro-Engineering and Rehabilitation*, vol. 8, no. 1, p. 22, 2011.

[3] J. A. Paradiso and T. Starner, "Energy scavenging for mobile and wireless electronics," *IEEE Pervasive Computing*, vol. 4, p. 18–27, January 2005.

[4] M. Hyland, H. Hunter, J. Liu, E. Veety, and D. Vashaee, "Wearable thermoelectric generators for human body heat harvesting," *Applied Energy*, vol. 182, pp. 518–524, 2016.

[5] X. Wu, G. Li, and D.-W. Lee, "A novel energy conversion method based on hydrogel material for self-powered sensor system applications," *Applied Energy*, vol. 173, pp. 103–110, 2016.

[6] D.-S. Kwon, H.-J. Ko, M.-O. Kim, Y. Oh, J. Sim, K. Lee, K.-H. Cho, and J. Kim, "Piezoelectric energy harvester converting strain energy into kinetic energy for extremely low frequency operation," *Applied Physics Letters*, vol. 104, p. 113904, March 2014.

[7] P. Pillatsch, E. Yeatman, and A. Holmes, "A piezoelectric frequency up-converting energy harvester with rotating proof mass for human body applications," *Sensors and Actuators A: Physical*, vol. 206, p. 178–185, February 2014.

[8] K. Ylli, D. Hoffmann, A. Willmann, P. Becker, B. Folkmer, and Y. Manoli, "Energy harvesting from human motion: exploiting swing and shock excitations," *Smart Materials and Structures*, vol. 24, p. 025029, January 2015.

[9] S. Niu, X. Wang, F. Yi, Y. S. Zhou, and Z. L. Wang, "A universal self-charging system driven by random biomechanical energy for sustainable operation of mobile electronics," *Nature Communications*, vol. 6, no. 1, 2015.

[10] S. Roundy and P. K. Wright, "A piezoelectric vibration based generator for wireless electronics," *Smart Materials and Structures*, vol. 13, p. 1131, August 2004.

[11] S. P. Beeby, R. N. Torah, M. J. Tudor, P. Glynne-Jones, T. O'Donnell, C. R. Saha, and S. Roy, "A micro electromagnetic generator for vibration energy harvesting," *Journal of Micromechanics and Microengineering*, vol. 17, p. 1257, June 2007.

[12] J. Hillenbrand, P. Pondrom, and G. Sessler, "Electret transducer for vibration-based energy harvesting," *Applied Physics Letters*, vol. 106, p. 183902, May 2015.

[13] V. Bhatnagar and P. Owende, "Energy harvesting for assistive and mobile applications," *Energy Science & Engineering*, vol. 3, no. 3, pp. 153–173, 2015.

[14] H. Fu, X. Mei, D. Yurchenko, S. Zhou, S. Theodossiades, K. Nakano, and E. Yeatman, "Rotational energy harvesting for self-powered sensing," *Joule*, vol. 5, pp. 1074–1118, May 2021.

[15] POWER Magazine, "Power from the People? A Long Way to Go." Available: `www.powermag.com/power-from-the-people-a-long-way-to-go/`, 2020. [Online].

[16] Jane Benson, NSRDEC Public Affairs, "Self-generated power could reduce Soldiers' load." Available: www.army.mil/article/177130/self-generated-power-could-reduce-soldiers-load, 2016. [Online].

[17] AMPY, "AMPY: Power your devices from your motion." Available: www.kickstarter.com/projects/1071086547/ampy-power-your-devices-from-your-motion/description, 2014. [Online].

[18] RayMing, "What is Energy Harvesting About?." Available: www.raypcb.com/energy-harvesting/, 2023. [Online].

[19] A. Alcocer, *Positioning and Navigation Systems for Robotic Underwater Vehicles*. PhD thesis, Universidade Tecnica De Lisboa Instituto Superior Tecnico, January 2010.

[20] N. H. Motlagh, T. Taleb, and O. Arouk, "Low-altitude unmanned aerial vehicles-based internet of things services: Comprehensive survey and future perspectives," *IEEE Internet of Things Journal*, vol. 3, pp. 899–922, 2016.

[21] S.-s. Choi and E.-k. Kim, "Building crack inspection using small uav," in *17th International Conference on Advanced Communication Technology (ICACT)*, pp. 235–238, July 2015.

[22] N. Gao, J. Zhao, D. Song, J. Chu, K. Cao, X. Zha, and X. Du, "High-precision and light-small oblique photogrammetry uav landscape restoration monitoring," in *2018 9th International Conference on Intelligent Control Information Processing*, pp. 301–304, IEEE, November 2018.

[23] D. Kang and Y.-J. Cha, "Autonomous uavs for structural health monitoring using deep learning and an ultrasonic beacon system with geo-tagging," *Computer-Aided Civil and Infrastructure Engineering*, vol. 33, no. 10, pp. 885–902, 2018.

[24] D. C. Tsouros, A. Triantafyllou, S. Bibi, and P. G. Sarigiannidis, "Data acquisition and analysis methods in uav- based applications for precision agriculture," *15th International Conference on Distributed Computing in Sensor Systems (DCOSS)*, pp. 377–384, May 2019.

[25] M. Silvagni, A. Tonoli, E. Zenerino, and M. Chiaberge, "Multipurpose uav for search and rescue operations in mountain avalanche events," *Geomatics, Natural Hazards and Risk*, vol. 8, no. 1, pp. 18–33, 2017.

[26] A. King, "Inertial navigation-past, present, and future," in *Workshop on Airborne Navigation Systems (Digest No. 1997/169)*, pp. 3/1–3/9, 1997.

[27] R. Johannessen, "The role of gps in flight calibration," in *IEE Colloquium on Current and Future Trends in Flight Calibration of Radio Navigational Aids*, pp. 9/1–9/6, 1991.

[28] P. Djederich, "Global navigation satellite systems," in *Proceedings of the IEE Airborne Navigation Systems Workshop (1998/275)*, pp. 1/1–1/2, Manchester, UK, 1998.

[29] G. Mao, S. Drake, and B. Anderson, "Design of an extended kalman filter for uav localization," *Conference Proceedings of 2007 Information, Decision and Control, IDC*, pp. 224–229, March 2007.

[30] Flyability, "Elios 2." Available: `www.flyability.com/elios-2`, 2023. [Online; accessed April 23, 2023].

[31] Robotics Business Review Staff, "Flyability Launches Next Generation of Indoor Inspection Drone." Available: `www.roboticsbusinessreview.com/unmanned/unmanned-aerial/flyability-launches-next-generation-of-indoor-inspection-drone/`, 2019. [Online; accessed April 29, 2019].

[32] Niiveth Mani, "6 Ways the Oil and Gas Industry is Using Indoor Drone Inspections to Cut Costs." Available: `https://feds.ae/`

6-ways-the-oil-and-gas-industry-is-using-indoor-drone-inspections-to-cut-costself_l1_ymxvzw/, 2021. [Online; accessed April 28, 2021].

[33] Enviro Trenchless, "Drone Pipe Inspections." Available: https://envirotrenchless.com/service/drone-pipe-inspections/, 2019. [Online; Accessed 2019].

[34] EIT RawMaterials, "Autonomous Flying Robots for Safer Underground Mining Inspection and 3D Mapping." Available: https://eitrawmaterials.eu/autonomous-flying-robots-for-safer-underground-mining-inspection-and-3d-mapping/, 2021. [Online; accessed July 22, 2021].

[35] Aqua Strategy, "Video Prelude for Sewer Drone Service." Available: www.aquastrategy.com/article/video-prelude-sewer-drone-service, 2017. [Online; accessed October 2017].

[36] R. Kalman, "A new approach to linear filtering and prediction problems," *ASME Journal of Basic Engineering*, vol. 82, pp. 35–45, 1960.

[37] P. Djuric, J. Kotecha, J. Zhang, Y. Huang, T. Ghirmai, M. Bugallo, and J. Miguez, "Particle filtering," *IEEE Signal Processing Magazine*, vol. 20, no. 5, pp. 19–38, 2003.

[38] Y. Bar-Shalom and E. Tse, "Tracking in a cluttered environment with probabilistic data association," *Automatica*, vol. 11, no. 5, pp. 451–460, 1975.

[39] S. J. Julier and J. K. Uhlmann, "New extension of the Kalman filter to nonlinear systems," in *Signal Processing, Sensor Fusion, and Target Recognition VI* (I. Kadar, ed.), vol. 3068, pp. 182 – 193, International Society for Optics and Photonics, SPIE, 1997.

[40] E. Wan and R. Van Der Merwe, "The unscented kalman filter for nonlinear estimation," in *Proceedings of the IEEE 2000 Adaptive Systems for Signal Processing, Communications, and Control Symposium (Cat. No.00EX373)*, pp. 153–158, 2000.

[41] T. Dixon, "An introduction to the global positioning system and some geological applications," *Reviews of Geophysics*, vol. 29, no. 2, p. 249 – 276, 1991.

[42] K. Vickery, "Acoustic positioning systems. a practical overview of current systems," in *Proceedings of the 1998 Workshop on Autonomous Underwater Vehicles (Cat. No. 98CH36290)*, pp. 5–17, IEEE, 1998.

[43] G. Dissanayake, P. Newman, S. Clark, H. F. Durrant-Whyte, and M. Csorba, "A solution to the simultaneous localization and map building (slam) problem," *IEEE Trans. Robotics Autom.*, vol. 17, pp. 229–241, 2001.

[44] H. Durrant-Whyte and T. Bailey, "Simultaneous localization and mapping: part i," *IEEE Robotics  Automation Magazine*, vol. 13, no. 2, pp. 99–110, 2006.

[45] T. Bailey and H. Durrant-Whyte, "Simultaneous localization and mapping (slam): part ii," *IEEE Robotics  Automation Magazine*, vol. 13, no. 3, pp. 108–117, 2006.

[46] D. Sobers, G. Chowdhary, and E. Johnson, "Indoor navigation for unmanned aerial vehicles," in *AIAA Guidance, Navigation, and Control Conference and Exhibit*, AIAA Guidance, Navigation, and Control Conference and Exhibit, 2009.

[47] Y. Cao, "Uav circumnavigating an unknown target under a gps-denied environment with range-only measurements," *Automatica*, vol. 55, pp. 150–158, 2015.

[48] J. P. Matos-Carvalho, R. Santos, S. Tomic, and M. Beko, "Gtrs-based algorithm for uav navigation in indoor environments employing range measurements and odometry," *IEEE Access*, vol. 9, pp. 89120–89132, 2021.

[49] W. You, F. Li, L. Liao, and M. Huang, "Data fusion of UWB and IMU based on unscented kalman filter for indoor localization of quadrotor UAV," *IEEE Access*, vol. 8, pp. 64971–64981, 2020.

[50] A. R. Vetrella, G. Fasano, and D. Accardo, "Cooperative navigation in gps-challenging environments exploiting position broadcast and vision-based tracking," in *International Conference on Unmanned Aircraft Systems (ICUAS)*, pp. 447–456, June 2016.

[51] M. Gnanasekera, J. Katupitiya, A. V. Savkin, and A. H. T. E. De Silva, "A range-based algorithm for autonomous navigation of an aerial drone to approach and follow a herd of cattle," *Sensors (Basel, Switzerland)*, vol. 21, no. 21, p. 7218, 2021.

[52] M. Gnanasekera, A. V. Savkin, and J. Katupitiya, "Range measurements based uav navigation for intercepting ground targets," in *6th International Conference on Control, Automation and Robotics (ICCAR)*, pp. 468–472, April 2020.

[53] V. Stepanyan, K. S. Krishnakumar, and C. A. Ippolito, "Coordinated turn trajectory generation and tracking control for multirotors operating in urban environment," in *AIAA Scitech 2019 Forum*, p. 0957, 2019.

[54] M. B. Larsen, "Synthetic long baseline navigation of underwater vehicles," in *OCEANS 2000 MTS/IEEE Conference and Exhibition. Conference Proceedings (Cat. No. 00CH37158)*, vol. 3, pp. 2043–2050, IEEE, September 2000.

[55] A. S. Gadre and D. J. Stilwell, "A complete solution to underwater navigation in the presence of unknown currents based on range measurements from a single location," in *2005 IEEE/RSJ International Conference on Intelligent Robots and Systems*, pp. 1420–1425, IEEE, August 2005.

[56] P.-M. Lee, B.-H. Jun, K. Kim, J. Lee, T. Aoki, and T. Hyakudome, "Simulation of an inertial acoustic navigation system with range aiding for an autonomous underwater vehicle," *IEEE Journal of Oceanic Engineering*, vol. 32, no. 2, pp. 327–345, 2007.

[57] T. D. Casey, B. W. Guimond, and J. Hu, "Underwater vehicle positioning based on time of arrival measurements from a single beacon," *OCEANS 2007*, pp. 1–8, 2007.

[58] S. H. Dandach, B. Fidan, S. Dasgupta, and B. D. Anderson, "A continuous time linear adaptive source localization algorithm, robust to persistent drift," *Systems & Control Letters*, vol. 58, no. 1, pp. 7–16, 2009.

[59] P. Batista, C. Silvestre, and P. Oliveira, "Single range navigation in the presence of constant unknown drifts," in *2009 European Control Conference (ECC)*, pp. 3983–3988, IEEE, August 2009.

[60] P. T. M. Batista, C. Silvestre, and P. J. R. Oliveira, "Single range aided navigation and source localization: Observability and filter design," *Systems & Control Letters*, vol. 60, no. 8, pp. 665–673, 2011.

[61] P. Batista, C. Silvestre, and P. Oliveira, "Globally exponentially stable filters for source localization and navigation aided by direction measurements," *Systems & Control Letters*, vol. 62, no. 11, pp. 1065–1072, 2013.

[62] P. T. M. Batista, C. Silvestre, and P. J. R. Oliveira, "Single beacon navigation: Observability analysis and filter design," *Proceedings of the 2010 American Control Conference*, pp. 6191–6196, 2010.

[63] T. Hamel and C. Samson, "Position estimation from direction or range measurements," *Automatica*, vol. 82, pp. 137–144, 2017.

[64] D. Theodosis, S. Berkane, and D. V. Dimarogonas, "State estimation for a class of linear systems with quadratic output," *24th International Symposium on Mathematical Theory of Networks and Systems MTNS 2020*, vol. 54, no. 9, pp. 261–266, 2021.

[65] S. Berkane, D. Theodosis, T. Hamel, and D. Dimarogonas, "State estimation for linear systems with quadratic outputs," *IEEE Control Systems Letters*, vol. PP, pp. 1–1, 01 2023.

[66] A. Jazwinski, *Stochastic processes and filtering theory*. No. 64 in Mathematics in science and engineering, New York, NY [u.a.]: Acad. Press, 1970.

[67] Luis Rodrigues, "A Review of Probability and Least Squares Estimation - lecture notes," December 2022.

[68] P. Billingsley, *Probability and Measure, Third Edition (Wiley Series in Probability and Statistics)*. Wiley Series in Probability and Statistics, Wiley-Interscience, 3 ed., 1995.

[69] Princeton University, "Random Variables - COS 341 Fall 2002, Lecture 21," 2002. [Online].

[70] J. Maddock, P. A. Bristow, H. Holin, X. Zhang, B. Lalande, J. Råde, G. Sewani, and T. van den Berg, "Normal distribution." Available: `http://surl.li/sycai`. [Online].

[71] D. C. S. Miller, *Probability and Random Processes: With Applications to Signal Processing and Communications*. Academic Press, 1st ed., 2004.

[72] A. Winkelbauer, "Moments and absolute moments of the normal distribution - arxiv," 2014. [Online].

[73] P. Mörters and Y. Peres, *Brownian Motion*. Cambridge Series in Statistical and Probabilistic Mathematics, Cambridge University Press, 2010.

[74] E. Lewis, "Brownian motion and ito's formula." REU Papers - University of Chicago, 2020.

[75] L. Rodrigues, "Brief review of brownian motion - lecture notes," November 2022.

[76] C. Wu and R. Buyya, *Cloud Data Centers and Cost Modeling*. Morgan Kaufmann, 2015.

[77] A. Mcknight, "Some basic properties of brownian motion." VIGRE REU Papers - University of Chicago, 2009.

[78] I. Karatzas, "A tutorial introduction to stochastic analysis and its applications - lecture notes." Columbia University, September 1988.

[79] B. Øksendal, "Space-time stochastic calculus and white noise," *arXiv preprint arXiv:2210.17276*, 2022.

[80] M. Hauser, "The derivative of brownian motion is white gaussian noise - lecture notes." `http://mbhauser.com/informal-notes/white-gaussian-noise.pdf`, 2023.

[81] K. Itô, "109. stochastic integral," *Proceedings of the Imperial Academy*, vol. 20, no. 8, pp. 519–524, 1944.

[82] J. Goodman, "Stochastic calculus: Stochastic integral, ito integral - lecture notes," 2022.

[83] S. Särkkä and A. Solin, *Applied Stochastic Differential Equations*. Institute of Mathematical Statistics Textbooks, Cambridge University Press, 2019.

[84] G. Gerhartz, "Langevin and fokker-planck equation." Seminar: Theoretical Statistical Physics, June 2023. Supervised by Prof. Dr. Georg Wolschin.

[85] R. Hermann and A. Krener, "Nonlinear controllability and observability," *IEEE Transactions on Automatic Control*, vol. 22, no. 5, pp. 728–740, 1977.

[86] P.-J. Bristeau, N. Petit, and L. Praly, "Design of a navigation filter by analysis of local observability," pp. 1298 – 1305, January 2011.

[87] W. J. Rugh, *Linear System Theory (2nd Ed.)*. USA: Prentice-Hall, Inc., 1996.

[88] L. M. Silverman and H. E. Meadows, "Controllability and observability in time-variable linear systems," *Siam Journal on Control*, vol. 5, pp. 64–73, 1967.

[89] L. Weiss, "The concepts of differential controllability and differential observability," *Journal of Mathematical Analysis and Applications*, vol. 10, no. 2, pp. 442–449, 1965.

[90] P. Batista, N. Petit, C. Silvestre, and P. Oliveira, "Relaxed conditions for uniform complete observability and controllability of ltv systems with bounded realizations," *IFAC-PapersOnLine*, vol. 50, no. 1, pp. 3598–3605, 2017. 20th IFAC World Congress.

[91] P. Morin, A. Eudes, and G. Scandaroli, "Uniform observability of linear time-varying systems and application to robotics problems," in *Geometric Science of Information* (F. Nielsen and F. Barbaresco, eds.), (Cham), pp. 336–344, Springer International Publishing, 2017.

[92] B. Ni and Q. Zhang, "Stability of the kalman filter for continuous time output error systems," *Systems  Control Letters*, vol. 94, pp. 172–180, 2016.

[93] G. Kern, "Uniform controllability of a class of linear time-varying systems," *IEEE Transactions on Automatic Control*, vol. 27, no. 1, pp. 208–210, 1982.

[94] The SciPy Community, "SciPy Official Website." Available: `https://scipy.org/`, 2024. [Online].

[95] G. H. Golub and C. F. V. Loan, *Matrix Computations*. Baltimore, MD: Johns Hopkins University Press, 4th ed., 2013.

[96] P. Virtanen, R. Gommers, T. E. Oliphant, *et al.*, "Scipy 1.0: fundamental algorithms for scientific computing in python," *Nature Methods*, vol. 17, pp. 261–272, 2020.

[97] G. Besançon, *An Overview on Observer Tools for Nonlinear Systems*, pp. 1–33. Berlin, Heidelberg: Springer Berlin Heidelberg, 2007.

[98] G. Besançon, G. Bornard, and H. Hammouri, "Observer synthesis for a class of nonlinear control systems," *European Journal of Control*, vol. 2, no. 3, pp. 176–192, 1996.

[99] G. Bornard, N. Couenne, and F. Celle, "Regularly persistent observers for bilinear systems," in *New Trends in Nonlinear Control Theory* (J. Descusse, M. Fliess, A. Isidori, and D. Leborgne, eds.), (Berlin, Heidelberg), pp. 130–140, Springer Berlin Heidelberg, 1989.

[100] J.-P. Gauthier and I. Kupka, *Deterministic Observation Theory and Applications*. Cambridge University Press, 2001.

[101] X. Mao, G. Marion, and E. Renshaw, "Environmental brownian noise suppresses explosions in population dynamics," *Stochastic Processes and their Applications*, vol. 97, no. 1, pp. 95–110, 2002.

[102] J. Calatayud, J.-C. Cortés, and F. A. Dorini, "On the random non-autonomous logistic equation with time-dependent coefficients," *Fluctuation and Noise Letters*, vol. 20, no. 04, p. 2150038, 2021.

[103] T. Kawano, "Anthropocene is the epoch in which we handle our future," *Bulletin du Centre Franco-Japonais d'Histoire des Sciences (Kitakyushu-Paris)*, vol. 13, pp. 1–18, August 2019.

[104] D. Jiang and N. Shi, "A note on nonautonomous logistic equation with random perturbation," *Journal of Mathematical Analysis and Applications*, vol. 303, p. 164, January 2005.

[105] J. S. Fulda, "The logistic equation and population decline," *Journal of Theoretical Biology*, vol. 91, no. 2, pp. 255–259, 1981.

[106] M. R. Q.A. and L. Rodrigues, "Nonlinear observer for quadrotor waypoint navigation using only range measurements," in *2023 9th International Conference on Control, Decision and Information Technologies (CoDIT)*, pp. 2439–2444, 2023.

[107] L. Rodrigues, "Navigation in 1d with range measurements - research seminar," September 2022.

[108] P. Panthongsy, D. Isarakorn, P. Janphuang, and K. Hamamoto, "Fabrication and evaluation of energy harvesting floor using piezoelectric frequency up-converting mechanism," *Sensors and Actuators A: Physical*, vol. 279, pp. 321–330, 2018.

[109] S. DeBruin, B. Campbell, and P. Dutta, "Monjolo: An energy-harvesting energy meter architecture," in *Proceedings of the 11th ACM Conference on Embedded Networked*

*Sensor Systems*, SenSys '13, (New York, NY, USA), Association for Computing Machinery, 2013.

[110] A. Cervera, Z. Rubinshtein, M. Gad, R. Riemer, and M. M. Peretz, "Biomechanical energy harvesting system with optimal cost-of-harvesting tracking algorithm," *IEEE Journal of Emerging and Selected Topics in Power Electronics*, vol. 4, no. 1, pp. 293–302, 2016.

[111] S. Roos-Hoefgeest, J. Cacace, V. Scognamiglio, I. Álvarez, R. C. González, F. Ruggiero, and V. Lippiello, "A vision-based approach for unmanned aerial vehicles to track industrial pipes for inspection tasks," in *2023 International Conference on Unmanned Aircraft Systems (ICUAS)*, pp. 1183–1190, June 2023.

[112] H. H. Helgesen, F. S. Leira, T. A. Johansen, and T. I. Fossen, "Tracking of marine surface objects from unmanned aerial vehicles with a pan/tilt unit using a thermal camera and optical flow," in *2016 International Conference on Unmanned Aircraft Systems (ICUAS)*, pp. 107–117, June 2016.

[113] M. Israel and A. Reinhard, "Detecting nests of lapwing birds with the aid of a small unmanned aerial vehicle with thermal camera," in *2017 International Conference on Unmanned Aircraft Systems (ICUAS)*, pp. 1199–1207, June 2017.

[114] A. Shukla, H. Xiaoqian, and H. Karki, "Autonomous tracking and navigation controller for an unmanned aerial vehicle based on visual data for inspection of oil and gas pipelines," in *16th International Conference on Control, Automation and Systems (ICCAS)*, pp. 194–200, June 2016.

[115] B. Patel, *Visual Localization for UAVs in Outdoor GPS-denied Environments*. PhD thesis, Aerospace Science and Engineering, November 2019.

[116] F. Vanegas, K. J. Gaston, J. Roberts, and F. Gonzalez, "A framework for uav navigation and exploration in gps-denied environments," in *2019 IEEE Aerospace Conference*, pp. 1–6, IEEE, March 2019.

[117] B. Yang and E. Yang, "A survey on radio frequency based precise localisation technology for uav in gps-denied environment," *Journal of Intelligent & Robotic Systems*, vol. 103, p. 38, 2021.

[118] Y. Yang, J. Khalife, J. J. Morales, and Z. M. Kassas, "Uav waypoint opportunistic navigation in gnss-denied environments," *IEEE Transactions on Aerospace and Electronic Systems*, vol. 58, no. 1, pp. 663–678, 2022.

[119] M. Gnanasekera, J. Katupitiya, A. V. Savkin, and A. E. De Silva, "A range-based algorithm for autonomous navigation of an aerial drone to approach and follow a herd of cattle," *Sensors*, vol. 21, no. 21, 2021.

[120] C. Evrendilek and H. Akcan, "On the complexity of trilateration with noisy range measurements," *IEEE Communications Letters*, vol. 15, no. 10, pp. 1097–1099, 2011.

[121] D. Moore, J. Leonard, D. Rus, and S. Teller, "Robust distributed network localization with noisy range measurements," in *Proceedings of the 2nd International Conference on Embedded Networked Sensor Systems*, SenSys '04, (New York, NY, USA), p. 50–61, Association for Computing Machinery, 2004.

[122] L. Rodrigues and M. R. Q. A., "Verhulst-based observer for uav waypoint navigation using quadratic measurements." *Transactions of the Institute of Measurement and Control* - [Under review], 2024.

[123] J. Abel and J. Smith, "Source range and depth estimation from multipath range difference measurements," *IEEE Transactions on Acoustics, Speech, and Signal Processing*, vol. 37, no. 8, pp. 1157–1165, 1989.

[124] Y. Chan and K. Ho, "A simple and efficient estimator for hyperbolic location," *IEEE Transactions on Signal Processing*, vol. 42, no. 8, pp. 1905–1915, 1994.

[125] K. Cheung, H. So, W.-K. Ma, and Y. Chan, "Least squares algorithms for time-of-arrival-based mobile location," *IEEE Transactions on Signal Processing*, vol. 52, no. 4, pp. 1121–1130, 2004.

[126] A. Polyanin and V. Zaitsev, *Handbook of Ordinary Differential Equations: Exact Solutions, Methods, and Problems*. January 2018.

[127] DALL·E 3. Prompt: Image generated by DALL·E 3 based on the prompt: "A pipeline inspection using a quadrotor placed on top of the pipeline. At the beginning of the pipeline, there is an emitter installed on top of the pipeline. The quadrotor should be at a higher distance to the top of the emitter to avoid colliding. Position the quadrotor directly above the pipeline at a notably minimal distance above each range measurement emitter stationed at the waypoints.".

[128] M. Kruglyakov, E. Marshalko, A. Kuvshinov, M. Smirnov, and A. Viljanen, "Multi-site transfer function approach for real-time modeling of the ground electric field induced by laterally-nonuniform ionospheric source," *Space Weather*, vol. 21, October 2023.